REPUBLIC OF TURKEY
ADANA ALPARSLAN TÜRKEŞ SCIENCE AND TECHNOLOGY UNIVERSITY

INSTITUTE OF GRADUATE STUDIES
DEPARTMENT OF MECHANICAL ENGINEERING

INVESTIGATION OF FLOW CHARACTERISTICS FOR DIFFERENT GROOVED SHAPE AND BARE CYLINDER AT DIFFERENT HEIGHTS IN SHALLOW WATER

Meltem ÇALIŞKAN
MASTER OF SCIENCE

ADANA 2021

REPUBLIC OF TURKEY

ADANA ALPARSLAN TÜRKEŞ SCIENCE AND TECHNOLOGY UNIVERSITY

INSTITUTE OF GRADUATE STUDIES

DEPARTMENT OF MECHANICAL ENGINEERING

INVESTIGATION OF FLOW CHARACTERISTICS FOR DIFFERENT GROOVED SHAPE AND BARE CYLINDER AT DIFFERENT HEIGHTS IN SHALLOW WATER

Meltem ÇALIŞKAN

MASTER OF SCIENCE

SUPERVISOR

Assoc. Prof. Dr. Naime Filiz ÖZDİL

ADANA 2021

I hereby declare that all information in this thesis has been obtained and presented in accordance with academic rules and ethical conduct. I also declare that, as required by these rules and conduct, I have fully cited and referenced all information that is not original to this work.

[Signature]
Meltem ÇALIŞKAN

ABSTRACT

INVESTIGATION OF FLOW CHARACTERISTICS FOR DIFFERENT GROOVED SHAPE AND BARE CYLINDER AT DIFFERENT HEIGHTS IN SHALLOW WATER

Meltem ÇALIŞKAN

Department of Mechanical Engineering

Supervisor: Assoc. Prof. Dr. Naime Filiz ÖZDİL

February 2020, 96 pages

In this project, the control of the unsteady flow structure formed behind a cylinder placed horizontally in shallow water is investigated experimentally with the help of grooves having different geometries opened on the cylinder. For this purpose, the effects of the geometric parameters of the grooves and the different heights where the horizontal cylinder is placed in the water on the flow structure behind the horizontal cylinder are examined in detail with the help of particle imaging velocimetry (PIV) technique. The experiments are carried out at a constant Re number at different heights (h_D) where the horizontal cylinder is placed in shallow water. With the help of PIV technique, instantaneous and average velocity vectors are measured in two dimensions at many points simultaneously in a planar flow area. With the help of the measured velocity vectors, instantaneous and average vortex and streamline values and turbulence (normal and Reynolds stresses) statistics in the flow area are obtained and the results obtained are analyzed with the help of TECPLOT program and detailed information about the flow is obtained. In CorelDRAW program, instantaneous velocity vectors and vortex contours are monitored and detailed information about flow structure is obtained. It is concluded that large negative counter at h: 37.5 mm is observed for bare cylinder, at h: 45 mm for square grooved cylinder and rectangular grooved cylinders. Also, no negative counter is observed at h: 0 mm due to the bottom effect. Two foci points and saddle point have been seen as they move away from the surface. When the wake regions consisting of two foci points are examined, the smallest vortex region is at h: 37.5mm rectangular grooved cylinder at a: 90^o and 95^o.

Keywords: Flow Control, Grooved Cylinder, Shallow Water, PIV.

ÖZET

SIĞ SUDA FARKLI YÜKSEKLİKLERDE YATAY KONUMLANDIRILMIŞ SİLİNDİR ARKASINDA OLUŞAN DAİMİ OLMAYAN AKIŞ YAPISININ, SİLİNDİR ÜZERİNE DEĞİŞİK GEOMETRİLERDE OYUKLAR AÇILARAK KONTROLÜ

Meltem ÇALIŞKAN

Makina Mühendisliği Anabilim Dalı

Danışman: Doç. Dr. Naime Filiz ÖZDİL

Şubat 2021, 96 sayfa

Bu projede, sığ su içerisine yatay olarak yerleştirilmiş olan bir silindir arkasında oluşan daimi olmayan akışın yapısının, silindirin üzerine açılan farklı geometrilere sahip oyukların yardımıyla kontrolü deneysel olarak araştırılmıştır. Bu kapsamda oyuklara ait geometrik parametreler ile yatay silindirin su içerisinde yerleştirildiği farklı yüksekliklerin, yatay silindirin arkasındaki akış yapısına etkileri parçacık görüntülemeli hız ölçüm tekniği ile detaylı olarak incelenmiştir. Deneyler, yatay silindirin sığ su içerisinde yerleştirildiği farklı yüksekliklerde (h) sabit Re sayısında gerçekleştirilmiştir. Geometrik parametreler ise; dikdörtgen kesitli oyuk için, silindir üzerine silindir boyunca açılan oyuğun genişliğinin (w) oyuğun yüksekliğine (d) oranı, üçgen kesitli oyuk için ise, silindir üzerine silindir boyunca açılan oyuğun açısıdır (β). Parçacık görüntülemeli hız ölçüm tekniği ile düzlemsel bir akış alanı içerisinde aynı anda birçok noktada anlık ve ortalama hız vektörleri iki veya üç boyutlu olarak ölçülmüştür. Ölçülen hız vektörleri yardımıyla akış alanındaki anlık ve ortalama girdap ve akım çizgisi değerleri ile türbülans (normal ve Reynolds gerilmeleri) istatistikleri elde edilmiş ve elde edilen sonuçlar TECPLOT programı yardımıyla analiz edilerek akış hakkında detaylı bilgilere ulaşılmıştır. CorelDRAW programında anlık hız ve girdap konturları, bilgisayar ortamında izlenerek akış yapısı hakkında detaylı bilgilere sahip olunmuştur. Sonuç olarak; oyuksuz silindir için h: 37.5 mm yüksekliğinde, kare oyuklu silindir ve dikdörtgen oyuklu silindirler için h: 45 mm yüksekliğinde en büyük negatif basınç bölgesi gözlenmiştir. Ayrıca, yüzey etkiden dolayı h: 0 mm'de negatif basınç bölgesi gözlenmemiştir. Yüzeyden uzaklaştıkça iki odak noktası ve eyer noktası görülmüştür. İki odak noktasından oluşan art izi bölgeleri incelendiğinde, en küçük girdap bölgesi 90^{o} ve 95^{o}'de h: 37.5 mm dikdörtgen oyuklu silindirde meydana geldiği görülmüştür.

Anahtar Kelimeler: Akış Kontrolü, Oyuklu Silindir, Sığ Su, PIV.

dedication

ACKNOWLEDGEMENTS

I would like to express my deepest appreciation to my invaluable Assoc. Prof. Dr. Naime Filiz ÖZDİL, who has always helped me with her inspiring and leading nature, and she has educated me with her expertise and experience in my graduate studies.

I would like to thank my dear teammate Atakan TANTEKİN, who always supported and helped me from the experimental stage to the final stage of my thesis.
I would like to thank Prof. Dr. Hüseyin AKILLI and Prof. Dr Beşir ŞAHIN, who helped me immensely in becoming an engineer and opened their laboratories to experimental working.

I would like to thank M. Oğuz TAŞÇI and Sergen TÜMSE for guiding and conveying their experiences in laboratory studies.

I would also like to thank Mine EFEOĞLU and Abdurrahman Furkan GÜLBAŞ, who made me happy with their presence during my master's degree.

This thesis was financially supported by TUBİTAK with project number of 118M794.

TABLE OF CONTENTS

LIST OF FIGURES

LIST OF TABLES

NOMENCLATURE

PIV	: Particle Image Velocimetry
CD	: Drag Coefficient
h	: Height
D	: Cylinder diameter
a	: Angle
<V>	: Time-averaged velocity vectors
<ψ>	: Corresponding streamline topology
u'u'	: Streamwise Reynolds normal stress
v'v'	: Spanwise Reynolds normal stress
Fr	: Froude number
Re	: Reynolds number
w	: Width of grooved
d	: Depth of grooved
St	: Strouhal number

1. INTRODUCTION

In the environment, many objects are seen in the flow affected by the fluid. This flow creates non-permanent loads both on the body and behind the body. These loads and vibrations cause fatigue in the body. Besides, these vortices affect the environmental factors, especially in shallow water applications, resulting in erosion in streams and rivers, and transport of particles and pollution at the bottom. In order to prevent the problems caused by the vortex structure formed behind an object placed in the flow, it is necessary to control the non-permanent flow structure and to reduce the turbulence intensity in the region behind the body. In general, control methods in the flow around an object are divided into two classes. These are active and passive control methods. Active control effected from the outside while passive control didn't need the external energy supply to change the flow structure.

1.1. Flow Control

There are various engineering applications that require the control of irregularities caused by flow both on the body and its back. For example, by controlling the distribution of the air flow on the wings of the aircraft, the magnitude of the forces acting on the aircraft such as lift and drag are changed. Thus, the take-off, safe flight and landing of the aircraft are provided. The flow around the cylinder is nowadays encountered in areas such as construction, aviation, machinery and chemistry. In engineering applications such as noise and vibration control and control of weather events, situations similar to the flow on the cylinder are observed. In the past, many researchers preferred to examine the flow structure around the cylinder as a blunt body due to the commonality of cylinder-like structures in engineering applications. Examples of these applications are heat exchanger tubes, bridge piers, offshore oil platforms, power plant chimneys, energy transmission lines, cylindrical structures.

1.2. Shallow water and PIV

Flows where the width of the flow is greater than its depth is called as shallow water flow such as flow around the ship. Flow floor and flow free surface have significant effects on flow structure in shallow water flows compared to deep water flows. Many flows in nature, especially flows in rivers and streams, flows in coastal areas of seas and lakes, flow around bridge piers, are examples of large shallow water flows. The small distance between the bottom and the surface in shallow waters makes the flow much more complex (3-

dimensional) than the flow in deep waters (high chimneys, oil platforms installed in deep water, high buildings, etc.).

Due to the complex nature of the flow around mass objects, it is very difficult to evaluate with qualitative (paint) images and does not give numerical results. However, the use of the PIV method provides the opportunity to measure with quantitative images that give numerical results. It also makes possible to provide researchers with useful parameters for both practical and design. In the experimental study, with the help of two-dimensional velocity fields determined by particle imaging velocity measurement method (PIV), the vortex structure formed in the intermediate region of the cylinder pair and in the near wake, streamlines and turbulence statistics and flow structure are determined depending on time. With the PIV measurement technique that has been used in fluid mechanics very detailed information about the structure of non-steady flow has begun to be obtained.

1.3. Experimental Procedure

This project is designed to ensure that the non-continuous flow formed behind a cylinder, which has cavities in different geometries such as square, rectangular and triangular, places in shallow water at various heights from 0 mm to 60 mm (h = 0 mm, 15 mm, 22.5 mm, 30 mm, 37.5 mm, 45 mm, 52.5 mm and 60 mm). It is an experimental study aiming passive control. The study consists of 3 parts. In the first step, bare cylinder, cylinder having square grooved ((w / d = 1 (width of the grooved (w), height of the grooved (d)), cylinder having rectangular grooved (w / d = 2) and cylinder having equilateral triangular grooved (= 60^o) have been performed in various level of shallow water. In the second step, the cavities have been rotated at certain angles ($\alpha = 0^o$, 80^o, 85^o, 90^o and 95^o) to examine the effect of these cavities on the flow separation. In this study, Froude Number is calculated as 0.27. The calculated Froude number is below from critical Froude number (Fr<1) which means the results is valid for subcritical regimes. In last step, average velocity and eddy turbulence statistics are calculated using particle velocity measurement technique. Although there are many studies on deep water flow control in the literature, studies conducted in shallow water are considered insufficient and as a basis for future studies.

The drag coefficient is a dimensionless quantity that used to calculate the friction or resistance of a body in a flow. The reduction in the drag coefficient at high aspect ratios is primarily due to the boundary layer staying attached to the surface longer and the resulting pressure recovery. For this reason, examine of the drag coefficient helps more to understand the flow.

2. LITERATURE REVIEW

In litaratüre, there are many studies about flow caharacteristic around cylinder using active and passive control techniques. The following examples of flow control can be seen in literature.

Yagmur et al. (2017) examined a triangular cylinder with the different Reynolds numbers and results were compared by using Particle Image Velocimetry and Large Eddy Simulation methods. The data obtained as a result of this experiment were as follows: as the Reynolds numbers were increased, the CD decreased. However, the Power Spectral Density (PSD) and the vortex shedding frequency increased. For the same Reynolds numbers, the experimental and numerical results were consistent.

Sooraj et al. (2019) studied an investigation about three vertical arranged cylinders for the proportion of the distance between the cylinders (s) and the diameter of the cylinders (d). The interface of the inner shear layers formed between the cylinders was greater compared to the connection between the shear layers formed around a roll for lower void rates. This meant that according to the experiment, flow characteristics and CD were affected by different Reynolds number and gap ratio.

Özdil and Akıllı (2019) showed single and dual cylinders positioned parallel to the channel bottom. The cylinder located different levels during the experiments to examine the effect of the distance on flow characteristics. The dimension of the wake area rises as the space between tandem cylinders deepens.

Ozdil and Akilli (2015) demonstrated flow characteristics around the horizontal cylinder. This cylinder was positioned as a different immersion ratio. As this ratio was increased from 0.25 to 1, the jet-like flow velocity was increased. After ratio1, values had changed.

Oruç et al. (2016) investigated bare and drop-shaped mesh cylinders using the PIV method with passive control. At this experiment, Reynolds numbers were determined different parameters. It was substantially vortexs on a large scale in the downstream direction of the bare cylinder. To make flow control, they shaped cylinders as drop mesh. They managed

large-scale vortical flow structure vorticity layers, Reynolds shear stress and turbulent kinetic energy. As a result of this study, the flow structure was controlled successfully.

Oruç (2012) studied both bare cylinders and streamline shaped cylinders. It was observed that flow was controlled with a shaped cylinder in comparison with the bare cylinder at their experiment results. Flow more controlled at shaped cylinders when it was compared cylinder shape and L/D ratio effect on the flow characteristic.

Canpolat and Sahin (2017) investigated square grooved cylinder was positioned different groove angle in the water by using PIV method. According to this experiment, it was observed that the critical angle was 80^{o}. Since flow separation started and occured vorticity, Karman vortex etc. at this angle.

The flow characteristic of hole circular cylinders was investigated by Durhasan et al. (2018). Moreover, the PIV method was used at this experiment. Cylinder diameter and Reynolds number were 100 mm and 10.000, respectively. In the experiment, it was aimed to control vortex, by changing the hole in different range. As a result of these phenomena as the hole was increased, the wake region decreased due to elongated and fragmented shear layers and reduced magnitudes of vortices.

Zhou et al. (2015) aimed to show flow characteristics with smooth, grooved and dimpled cylinders using a piezo-electric load cell and PIV. The experiments were carried out on the open channel, towing tang. According to the result of the experiment, the flow was more controlled at grooved and dimpled than the smooth cylinder.

Yayla and Teksin (2018) the flow structures behind the flexible separating plate attached to a circular cylinder and the post-flow wake were examined qualitatively and quantitatively in three different Reynolds numbers in deep water. It was concluded that the flexible separation plate was found to have a significant effect on vortex pouring and the fluctuations were significantly attenuated using control material.

Liu et al. (2011) used cacti shaped and smooth surfaces cylinder by using PIV method in order to understand the wake characteristic of the cylinders. It had been observed that small

vortices, superimposed on the slicing layers behind the grooved cylinder, were developed and transported downstream in the same phase. As a result, a drastic reduction in vortex force on the roller surface was observed.

Canpolat (2015) studied on the flow structure flowing over different rectangular groove shaped cylinder positioned at different angles using the PIV method. It was concluded that the position of the groove on the surface of the cylinder had an effect on the function of the wake flow structure. The frequency of Karman vortex shedding depended greatly on the groove size. Finally, shear layer instability with external frequencies was induced on the grooved side.

Rinoshika and Rinoshika (2019) studied a front inclined hole on flow structures around a surface-mounted short cylinder. Compared with standart cylinder with inclined hole, the separation region along the free end surface was observed to decline and the rear separation ron increases. In the recirculation region, Vortex and Reynolds shear stresses were also suppressed.

Pinar et al. (2015) studied perforated cylinder with different hole sizes using the PIV method to learn more about the flow characteristics. The cutting layer was extended, fluctuations were considerably decreased and Karman vortex was impeded successfully using porosity cylinders.

Najafi et al. (2016) studied different angles of divergence about close to the cylinder the time-average flow configuration using PIV and dye experiment. A bipolar pattern with close vigilance was observed as the flow pattern and deviation angle changed.

Gozmen et al. (2013) examined bare and different size separating platform to investigate the vortex discharge of a circular cylinder in shallow water by PIV method. Reynolds stress was shown to be significantly reduced in the bare cylinder.

Firat et al. (2015) examined the flow structure of the cylinder and the square prism placed behind it at different distances and different angle as numeric. The efficacy of the control rod

in minimizing the time-averaged drag coefficient of the total system was decreased with increasing angle.

Karasu (2020) researched flow regulation over a diamond-shaped cylinder utilizing PIV slits experimentally. The results suggest that the use of slits could be an efficient passive control strategy for diamond-shaped cylinders.

Kahraman et al. (2012) studied horizontal cylinder with different cylinder diameter, Reynolds number and Froude number using PIV method. As cylinder diameter was increased, vorticity intensity, Reynolds stress correlations, and the primary recirculating bubble length increased.

Gao et al. (2018) examined the flow activity of the clockwise and counter-clockwise rotating cylinder. Clockwise and counterclockwise rotation created major wake effects and altered the wake flow mechanisms and vortex shedding patterns. The time-averaged streamline models tended to be non-symmetrical about the longitudinal flow axis.

Durhasan (2020) studied square grooved cylinder with slots to demonstrate the effect of the slot ratio on the properties of the wake flow and turbulence statistics. He used PIV technique. Proper orthogonal decomposition (POD) analyses suggested that the self-disposing jet significantly altered the function of vortex shedding contact. According to the results of the study, the drag coefficient, derived from PIV results, was reduced by up to 42% compared to the solid cylinder model.

Özkan et al. (2017) examined porosity cylinders to determine the capability of connected porosity plates in the nominally two-dimensional vortex removal of locked cylinders. The findings showed that the use of a porosity plate effectively suppressed the vortex shedding downstream of a spherical cylinder.

Durhasan et al. (2016) conducted an experimental study to examine the flow characteristic of perforated hollow cylinder around bare cylinder with the parameters of arc angle from 120^{o} to 180^{o} with 30^{o} intervals and porosities from 0.3 to 0.8 with 0.1 intervals. According to the this paper that the use of perforated cylinders eliminated downstream vortex around the cylinder.

Akıllı et al. (2005) proposed a study about flow structure around a vertical circular cylinder controlled by a splitter plate with the help of PIV technique in shallow water. The length of the splitter plate was kept constant and it was equal to diameter of the cylinder as D = 50 mm. In order to show the effect of plate thickness, (T), T/D ratios were selected as 0.016, 0.04 and 0.08. Moreover, as another parameter, the gaps between the cylinder and splitter plate were chosen from 0 to 100 mm with 12.5 mm increments. According to the cylinder diameter, Reynolds number was selected as 5000. They concluded that the splitter plate had a major effect on the attenuation of the vortex shedding for gap ratio between 0 and 1.75D. Furthermore, the normalized Reynolds stress had the highest value in G/D = 1.75.

Akıllı and Rockwell (2002) performed a study about vortex formation around a cylinder in shallow water conditions using PIV method. The free-stream velocity and Reynolds number were selected as 194 mm/s and 10052, respectively. They remarked that the degree of large-scale vorticity was decreased with progressive elevations above the bed.

Akıllı et al. (2008) represented an investigation about passive control of vortex shedding behind a circular cylinder with splitter plates by PIV technique. The Reynolds number was selected as 6300. Furthermore, the length of the splitter plate was changed from (L/D) 0.2 to 2.4. They concluded that the splitter plate had a major effect on the flow characteristics around the circular cylinder.

Song et al. (2019) investigated the drag reduction on flow around fully triangular grooved cylinder and semi triangular grooved cylinder by taking into account combined effects of depth, width and location at cylinder. The results revealed that as the fully separation point was disturbed by the grooved surface, the reverse pressure zone decreased. Semi triangular grooved cylinder had more significant effects on drag reduction than fully triangular grooved cylinder.

Fırat et al. (2017) studied wake regions behind fixed, hollow and rigid circular cylinders with the help of PIV technique. The experiment was done with various parameters as three-hole diameters, six hole-to-hole lengths and ten angles. According to the study, the results indicated that the efficacy of double rows of vortex suppressing holes decreased with a rising incidence angle.

Fırat et al. (2019) studied flow characteristics on a circular cylinder with holes using dye visualization, PIV and force measurement techniques. The holes were connected front and rare stagnation lines of the cylinder. Two different Reynolds numbers were selected for water channel and wind tunnel measurements as 6900 and 20000, respectively. They concluded that the vortex formation length was depended on the angular position and the presence of the holes. Moreover, the drag coefficient of the cylinder was increased by the presence of the transverse-oriented slit.

Özkan et al. (2012) studied the flow properties of the inner circular cylinder surrounded by the outer permeable cylinder using the PIV method. To evaluate the effect of the outer cylinder diameter and porosity on the flow dynamics of the inner cylinder, various outer cylinder diameters and porosities were used. The results revealed that the association of the inner cylinder shear layers was effectively avoided by the inclusion of the outer cylinder.

Özkan et al. (2017) researched flow structure on a circular cylinder with an attached permeable plate of different porosity ratios using PIV technique and dye experiment. As the parameter, porosity had been chosen as β:0.4, 0.5, 0.6, 0.7 and 0.8 to analyze the effect of proposity on flow characteristics. As a result of the analysis, the length of the vortex formation was increased, turbulent statics were reduced and the rate of vortex shedding decreased when the plate was added to the normal cylinder surface from the lower separation point. On the other hand, due to the increased cross-section area, the drag force acting on the cylinder was observed to be increased.

Sanli and Akıllı (2018) researched the flow behaviors around the pervious cylinders by using PIV technique in deep water. The results indicated that while the porosity on the cylinder ascend, turbulent kinetic energy and Reynolds shear stress dwindled. And also that for all diameter values of pervious cylinders, flow structures downstream of the permeable cylinder had identical patterns with each other.

Narayanan et al. (2018) studied on elastic filament attached to a circular cylinder under uniform flow. Their study was carried out for different wall proximities and gap ratios with numerically. As a result of their study, with lower gap ratios of 0.5 and 0.6, flapping

amplitude modulations were found. Moreover, the frequency of flaps was in conjunction with the shedding frequency in their study.

Wang et al. (2015) performed a study to examined the movement of two tandem cylinders close and parallel to the Plane Wall using PIV method. The Reynolds number was selected as 6300. The other parameters were spacing ratio and gap to cylinder diameter ratio. The cylinder centre-to-centre gap ratio was changing from 1.5 to 6, and the gap-height-to-cylinder-diameter ratio from 0.15 to 2. They observed that vortex shedding suppressed gap-height-to- cylinder-diameter less than 0.3.

Yang et al. (2018) investigated an experimental study about the pressure distribution and the hydrodynamic forces on a cylinder placed near a plane boundary at various Reynolds numbers and G/D ratios (G was the gap between cylinder and ground of the channel). According to this study, the drag coefficient decreased at smaller G/D ratios.

Bayraktar et al. (2014) examined a numerical study about flow characteristics of circular, diamond and square cross-sectional cylinders to reveal the wall proximity effects. The study was carried out in a 2D domain with the finite volume discretization method for Re=20000 and unsteady Reynolds averaged Navier-Stokes equations with Spalart-Allmaras turbulence model was used. According to the results, for the same G/D ratio, the highest St was observed in circular cylinder although shedding frequencies increased as the G/D ratio increased for all types of cylinders.

Shi et al. (2010) investigated an experimental study for wall proximity on flow characteristics on a 2D square cylinder with PIV and TR-PIV methods. Reynolds number was selected as 2250 and G/D ratios were selected as 0.1, 0.2, 0.4 and 0.8. Furthermore, the proper orthogonal decomposition (POD) technique was used to decompose the TR-PIV results. According to the results, the slight spatial asymmetry of the two time-mean recirculation zones were observed for the G/D=0.8 and 0.4 with vortex shedding. Moreover, with the reduction of G/D from 0.2 to 0.1, vortex shedding was suppressed and a large separation bubble was attached on the wall.

He et al. (2017) performed an experimental study about flow characteristics over a circular cylinder in the vicinity of a flat plate by PIV method. The cylinder was located above the flat plate with its axis parallel to the wall and normal to the flow direction. The Reynolds number was selected as 1072 and the G/D ratios were varied from 0 to 3. The results showed that when the $G/D \leq 2$, the cylinder wake observed as asymmetric and a boundary layer separation was induced on the flat plate downstream of the cylinder. Furthermore, with the decreasing G/D until the critical gap ratio as 0.25, the wake vortex shedding frequency increased.

Oner et al. (2008) examined the velocity zone in a steady, 2D, turbulent flow around a horizontal circular cylinder close a plane boundary with PIV technique. G/D ratios were selected as 0, 0.1, 0.2, 0.3, 0.6, 1 and 2. Reynolds numbers were selected as 840, 4150 and 9500. The results indicated that the changes in the flow structure became very slow for $G/D \geq 0.3$ and the wall proximity effect on the flow around the cylinder became significant for $G/D \geq 1$.

Akoz (2012) examined the velocity zone of 2D turbulent flow around a partially buried circular cylinder on a smooth plane boundary with PIV technique. The experiments were conducted for Re = 1000, 3000, 5000 and 7000. The another important parameter is B/D ratios. Where B was the burial ratio, selected as 0.25 and 0.5. The results presented that the separation points on the cylinder surface and the length of the separation region upstream and downstream of the cylinder were powerfully related the B/D proportion and Re number. The location of boundary separation on the cylinder moved further upstream for higher Re numbers and it shifted in downstream direction with the increment of B/D ratio.

Kiran et al. (2018) studied the flow characteristic around the bare cylinder with separator plate using pressure, hot wire and particle image velocimetry methods. The separator plate had been found to reduce drag by 13 percent over the bare cylinder configuration. In the presence of the separator plate, the flow direction and the transverse velocity changes in the cylinder direction decreased by 22 and 27 percent, respectively. Phase-averaged PIV measurements demonstrate that the eddies in the separator plate case were weaker than the bare cylinder.

Dai et al. (2018) studied the elimination of vortex for circular cylinders with a high Reynolds number by divider plates. Calculations had been made using OpenFOAM. Comparisons were

made with laboratory results and a standardized procedure was used to perform a systematic analysis to assess the efficacy of vortex suppression. To assist in the study,

two-point interaction of forces around the cylinder period were attained to establish the conditions for the differentiation of cross-sectional oscillations. The findings showed that the separator plates provided a realistic mechanism for vortex elimination with a high Reynolds number and the degree of elimination could be maximized with an optimum geometric arrangement.

Yang et al. (2020) numerically analyzed the movement of a horizontal circular cylinder placed on a vertical side wall. The objective of this study was to investigate the flow properties around the junction region between the cylinder and the two plane boundaries. Gap- diameter ratio, Reynolds number and length-diameter ratio had been chosen as $G/D = \infty$, 10, 0.5 and 0.2, Re_D= 1250, 2500 and 5000 and L/D=20 and 40, respectively. The three-dimensional flow structures formed in the junction region between the vertical wall and the cylinder were found to be highly affected by the space ratio. The final effect of the vertical wall was restricted 0.7D in the direction of the spinwise, 0.5D upstream and 3D downstream of the cylinder.

The drag force, transverse force, vertical force and flow field were investigated in the range of 0.033 to 1 with AR-range experimentily by Yang et al (2020). The scanning of the flow zone showed that two recirculation regions were formed below and behind the square cylinder. According to the report, the free-end effect was found to reduce the interaction of perforated eddies on both sides of the square cylinder. As the free surface of the case with AR = 0330 deformed severely and air was drawn into the free surface to create an air cavity, the air cavity was expanded, broken into smaller bubbles and escaped to the free surface. In situations of AR below 0.167, the modified laws of force coefficients varied from those of AR below 0.167 in this study.

Shi et al. (2020) suggested an enhanced turbulence model from the original k-model shear-bearing stress and its supremacy was estimated by modeling unstable flows through a D-shaped cylinder and a space that corresponded to two Reynolds number. Results in flow morphology and medium velocity profiles were correlated with experiments and other

turbulence models. It was evident that in blowdown body awakening flows and shear strata and separation flows of the cavity, the estimation of the updated turbulence model is greatly improved. Any special configurations of vortex could be caught in open spacious spaces where secondary vortexs coming from the shear layer and the split vortex near the trailing edge could induce high flow stability. This improved model for turbidity, with a better hydrodynamic / aerodynamic efficiency and stable eddy flows, was assumed to be useable for more complex turbocharged flow, with guidance for building or improving rotating machines.

Chen and Jirka (1995) experimentally investigated the flow structure around the cylinder by placing a cylinder with a diameter larger than the depth of water in their study. In their work, they visually examined the structure of the scar area by adding dye to the flow from a point just behind the cylinder. As a result of their experimental studies, they determined that shallow water flow exhibits different physical behaviors compared to deep water flow. It also stated that the flow in the track region exhibited three different behaviors in the flow around the cylinder in shallow water. These behaviors; stable trail zone, unstable trail zone and regular Karman street. They defined these flow models with the so-called critical stability parameter $S = C_fD / h_w$. Here C_f is the base friction coefficient, D is the cylinder diameter and hw is the water depth. In cases where the stability parameter was less than 0.2, the normal Karman street consisted of an unstable track zone between 0.2 and 0.5, and a stable track zone when it was greater than 0.5.

Zdravkovich (1980) studied the flow leaving a flat plate induced by a horizontal cylinder. G is described as the space between the underside of the cylinder and the bottom surface, and d is the cylinder diameter. Vortex street didn't occur for G / d = 0 situation. However, for the G / d = 0.2 situation, a vortex street was noticed in the turbulent boundary layer. Also, vortex street had developed in the laminar boundary layer for the G / d = 0.3 configuration.

Sheridan et al. (1997) examined the flow characteristics for a cylinder placed very near to the free surface. They came to the conclusion that there were three dissimilar situations; the first one was attached to the free surface, another was connected to the cylinder, the last one was the middle state between them.

Lei et al. (1999) conducted on the flow formed around a horizontal cylinder placed in different places within the boundary layer. Their purpose was to study the vortex street behavior by changing the boundary layer thickness, velocity gradient, pressure distribution, hydrodynamic forces, and the roller's proximity to the bed. They showed that the void ratio and the boundary layer influanced the friction and lift coefficients.

Leung et al. (1997) experimentally studied the transition properties of flow on an asymmetric grooved circular cylinder. They found that during the test range, high flow regimes occurred on the grooved side of the cylinder while flow was in the lower critical regime on the smooth side of the cylinder.

Quintavalla et al. (2013) analyzed drag reduction on grooved cylinders in the critic Reynolds number regime. Their results from experiments; showed that by using grooves, even at very shallow related groove depths, cross flows could have significant drag reductions for circular cylinders. It had been shown that increasing the entire groove area with increasing either the shape, width and depth of the launder had a important effect on reducing the critic Reynolds number.

Yamagishi and Oki (2004) investigated the effect of corrugated structure on flow structure around a cylinder. They analyzed the flow structure around the cylinder applying the RNG k - turbulence model and analyzed the surface flow model using the oil film method. As a result, they concluded that the friction coefficient of a circular cylinder with triangular grooves was reduced by about a ratio compared to a circular cylinder with arc groove.

Wang et al. (2014) examined the flow structure around the cactus-analog corrugated cylinder for ReD = 5.4×10^4. They found that in the grooved roller system, the vortex shedding process was more consistent but poorer than the smooth cylinder.

Zhang and Ko (1995) numerically analyzed incompressible flow through a straight and grooved circular cylinder. Studies had shown that grooves could influence flow properties in space as well as flow properties at the cylinder surface. In this study, using spectral analysis, frequency shifts were observed in the transition waves due to the grooves. This was an indication of drag reduction for flow around the corrugated cylinder in the critical regime.

Lim and Lee (2003) examined the flow structure behind the U-grooved cylinder using particle imaging velocity measurement technique. They found that U-grooves reduced the coefficient of friction acting on the roller compared to smooth rollers.

El-Makdah and Oweis (2013) studied the flow around a cylinder with a cactus-like groove. The cactus model was observed to exhibit improved vortex behavior on the circular pattern and the vortex tied closer to the cylinder surface.

Liu et al. (2011) experimentally investigated the spatio-temporal vortex properties of the grooved cylinder in order to reveal the vortex properties of the adult Saguaro cactus. Vortex measurements behind the smooth cylinder were made for ease of comparison. When looking at the results, it was seen that the spatial distribution of the highest frequency revealed that the grooved cylinder vortex rupture was delayed and the high-frequency shear layer eddies dominated the dead flow zone.

Zhou et al. (2015) experimentally investigated the flow around a smooth cylinder and a cylinder with longitudinal grooves for Reynolds numbers from $7.4x10^3$ to $1.8x10^4$. This paper aimed to advance understand the effects of the grooved surface on the drag coefficient and flow properties of the cylinder in general. The force measurement consequences presented that the grooved surface reduced the friction coefficient by a ratio compared to that of the smooth roll at the equal Reynolds number. The PIV measurement consequences presented that the sliding layer emerging from the grooved roll was lesser in value and smaller in size compared to a smooth roll. As another result of this experiment, it was observed that the vortex rupture in the cylinder depleted due to the grooved surface.

Alonzo-Garcia et al. (2015) presented a CFD study on the effect of V and U grooves on four diamond-shaped cylinders in non-critical flow conditions. The K-ε turbulence model was applied to wall corrections close to fully structured hexagonal grids. The results demonstrated that the numerical pattern was capabilty to produce the striking flow pattern and driving forces were generated in the lateral cylinders of the smooth cylinder array. As a result of the flow alignment created by the grooves, a jet flow was created between the lateral cylinders, which can cause the vibration effect caused by the vortex, especially in the rear cylinder. The magnitudes of the shear stresses at the bottoms and peaks for the V-grooved rollers were lower than those of the U-grooved rollers, but the separation points could be delayed due to the presence of U grooves.

3. MATERIALS AND METHODS

3.1. Water Channel

This study has been performed at Çukurova University Department of Mechanical Engineering, a closed water duct installed in the fluid mechanics laboratory. The water canal consists of two pieces of storage and an acrylic section between these two warehouses with dimensions 8000x1000x750mm (length x width x height). There is a 2:1 constriction section to allow the transition of the test section with the water tank at the entrance (Fig. 3.1 (a) and (b)).

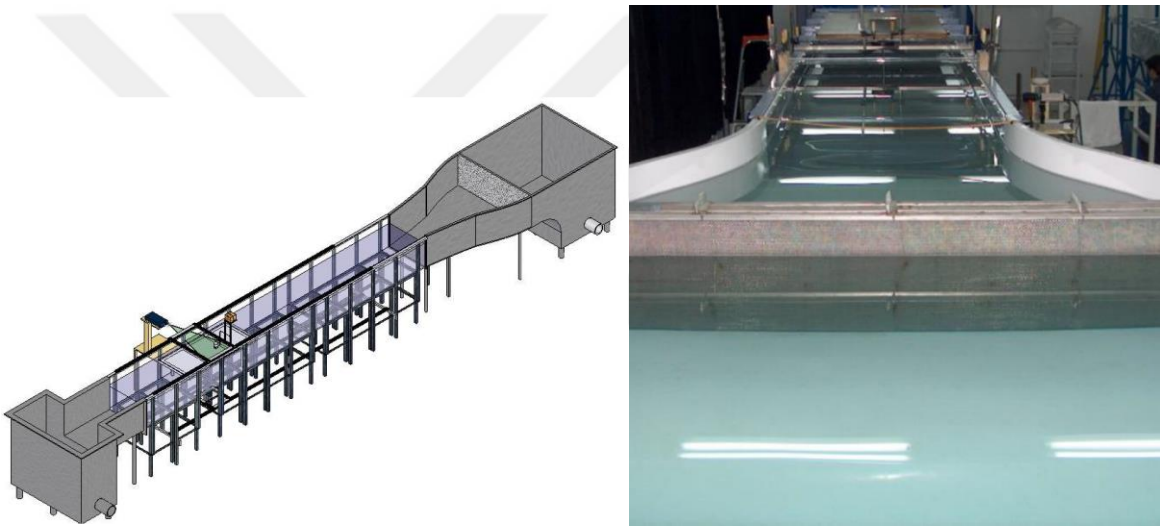

(a) **(b)**

Figure. 3.1. (a) The schematic respresentation of water channel; (b) The footage of water channel

The speed of the water in the channel has been adjusted by a pump operating at different speeds with the help of a speed control unit. Shallow water experiments are carried out on a platform placed in the water channel. The reason why the platform is chosen instead of the base of the channel for the experiments is that thanks to the platform, the hollow cylinders of different geometries and different angles used in the experiments are placed into the water without much disturbing the flow. The cylinders are placed in the metal block placed on this platform in order to provide stability of cylinders during the flow. Thus, both the perpendicularity of the cylinders to the flow is provided and the movement during the flow is prevented. The length of this platform used is 2300 mm, its width is 980 mm and the height of

the base of the platform from the bottom of the water channel is 220 mm with the acrylic layer on top.

Four types of cylinders have used in the experiment, as bare cylinder, triangular grooved shape cylinder, w / d = 1 square grooved shape cylinder and w / d = 2 rectangular grooved shape cylinder. During the experiments, cylinders have been rotated at $\alpha=0^o$ 80^o 85^o 90^o and 95^o at the clockwise direction in order to observe effect of grooved angle on flow structure. The flow direction of the water is zero. In this way, the effect of bare and groved cylinders have been investigated on flow characteristics. The cylinders to be controlled in the flow structure used in the experiments are made of acrylic material and have a diameter of D = 30 mm. The reason for choosing this cylinder diameter is to keep the blocking rate at reasonable levels, since the width of the water channel is 1000 mm. (Fig. 3.2)

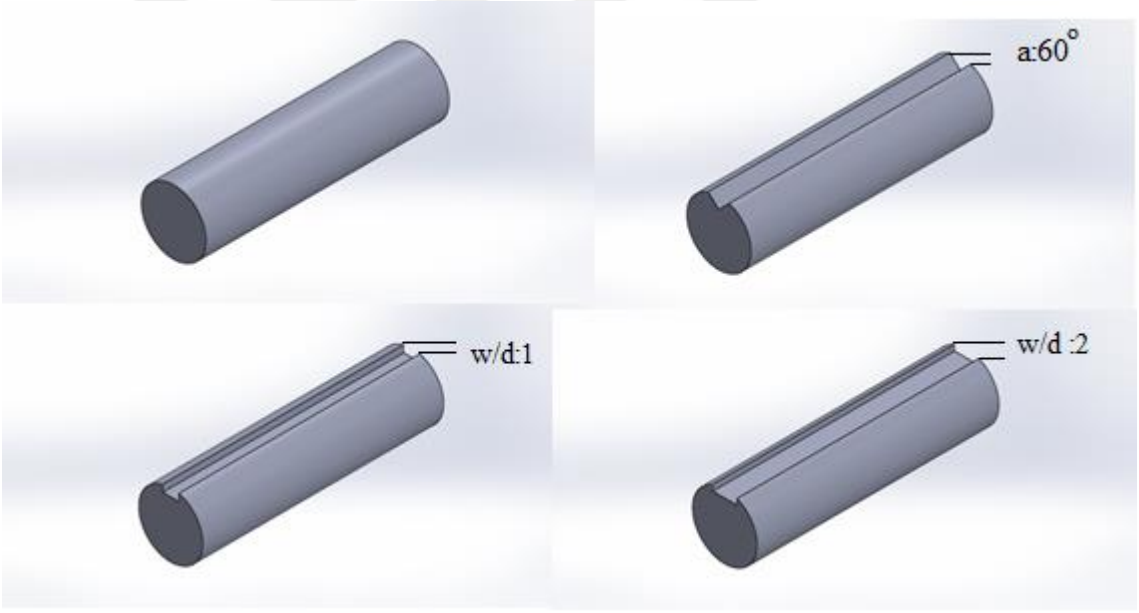

Figure. 3.2**.** Models used in experiments

Within the scope of the project, the flow structure is observed with dye experiments to have general information about the flow characteristics as a first study. The main reason for starting the studies with dye experiments is to determine the qualitative effects of the geometric parameters whose effects on the flow characteristics are investigated. The results of the dye experiment can be examined and compared with the results obtained from PIV experiments.

3.2. Dye Experiment

Rhodamine 6G and Rhodamine B have been preferred as light sensitive dyes (Fluorescent Dye) in dye experiments. This fluorescent dye is made into solution by mixing with water. The dye solution is transparent in daylight. However, when the dye is illuminated by laser in a dark environment, it becomes visible and becomes green. The dye solution prepared in a container has been left to flow from the front of the cylinder at a certain height with the help of a pipe that is thin enough not to disturb the flow structure. Illumination has been done with a 532 nm wavelength laser light. The stream that becomes visible has been recorded with a high speed resolution camera (SONY HD-SR1). The films that have been shot have been transformed into images with 24 images per second using the Play Memories program and the structure of the flow physics has been examined in detail. Then, by analyzing the video images, pictures representing the flow structure are obtained for each experimental situation. Each experiment has been videotaped for approximately three minutes.

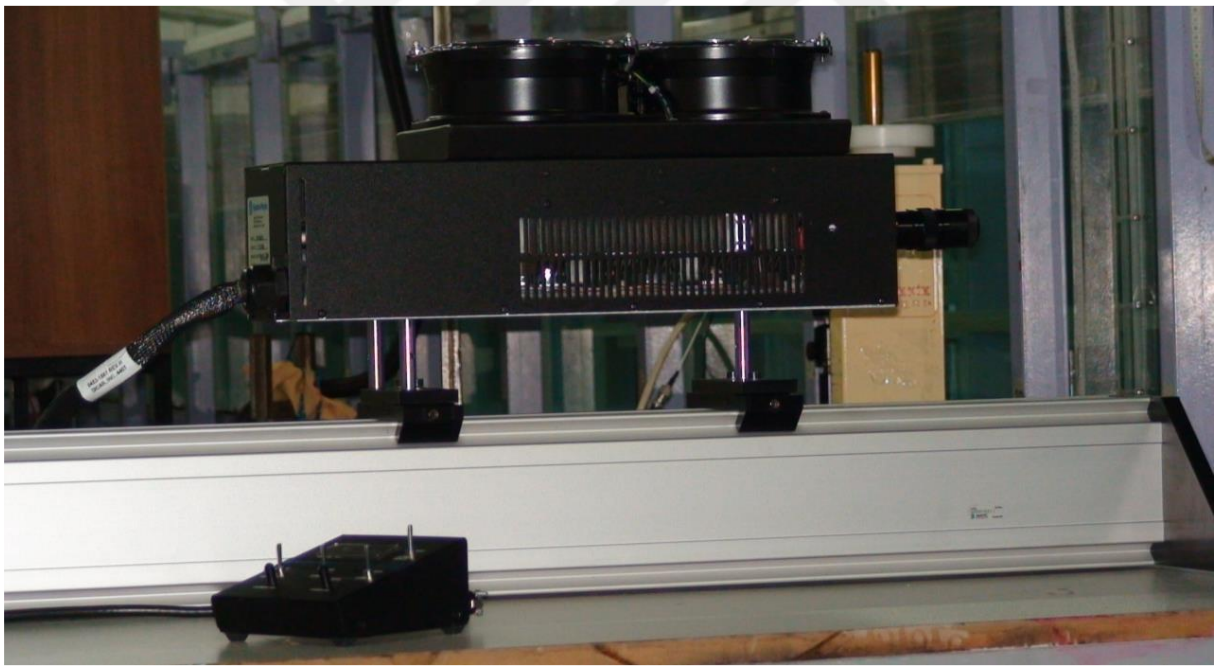

Figure. 3.3. Continuous laser used in dye experiment

3.3. PIV Experiment

One of the most important problems in fluid mechanics is to have information about the flow characteristics of that region by measuring at more than one point at the same time in the region under study. Many velocity measurement techniques provide information about flow by making time-dependent measurements at a single point. Especially in two-dimensional or

three-dimensional flows with a complex structure, the data obtained by measuring at only one point is not sufficient to interpret the structure of the flow. For two- and three-dimensional flows, it is possible to obtain the instantaneous velocity field in a planar region simultaneously by using the particle image velocitymetry technique. With the particle image velocitymetry technique, a certain planar surface can be illuminated and velocity vectors can be measured at many points simultaneously. Thanks to this technique, very detailed information about the non-steady flow structure is obtained. For example, it is necessary to measure instantaneous velocities at a certain frequency range at thousands of points simultaneously in order to determine the flow structure within a certain flow area in the separated flow region or the dead flow region. Namely, due to this measurement technique, analysis of the non-continuous complex flow structure is possible. In particle image velocitymetry technique applications, water is generally used as a fluid and the experiments are often carried out in a closed loop water channel. The particle image velocitymetry technique provides instantaneous or average information about the flow structure by measuring the velocities of small metal-coated solid particles at the micron level moving in the flow at the same speed as the fluid. In order to measure two-dimensional velocity with this technique, shiny silver-coated metal particles with a diameter of 10-20 micrometers with a density close to the density of water are sprinkled into the water. Although the density of the particles is relatively higher than the density of water (around 1100 kg / m3), they move at the same speed as water, since their sizes are in the micron range. General properties of the particles to be used; the laser light reflects well, does not cause corrosion on the channel equipment and model in the environment where the flow occurs, is not toxic, is clean to preserve the transparency of the fluid, and the intensity of the laser light does not reflect too much on the particles. The laser beam produced by the double-pulsed 120 mJ laser unit (Nd: YAG Laser) is turned into a laser beam of 1–2 mm thickness and different widths with the support of optical instruments. The laser unit can send a maximum of 15 laser beam pairs per second. The computer sends a signal to the laser source at regular intervals (30 signals / second). In each signal, two pictures are taken by a digital camera with milt intervals of milliseconds and transferred to the computer. The time (t) between two photos is entirely dependent on the velocity of the flow and the level of turbulence. Since the laser source is a pulsed type, the laser and the camera must work simultaneously. The device that adjusts the timing between the laser source and the digital camera (with a resolution of 1600 x 1200 pixels) is called a synchronizer and is controlled by a computer. These photos, which are

transferred to the computer, are usually divided into small sub-regions of 32x32 pixel size (these sizes can be increased or decreased if necessary) and using Fast Fourier transform, the displacements of the particles in each sub-region between the two images are found. As a result of the process of these pictures transferred to the computer, instantaneous velocity vectors are calculated. Since the time interval between both images and the average distance taken by the particles in each sub-region are known, the velocity of the flow in the considered sub-regions is calculated. In this study, 1000 instantaneous velocity vectors are measured in each experiment. Depending on the flow structure, at most 3% of the velocity vectors are composed of velocity vectors that do not conform to the flow structure called outlier. These velocity vectors are determined by the Cleanvec program, which is openly shared in the literature, and these vectors are extracted from the flow field. Instead of outlier vectors, new vectors obtained by least squares method are calculated by using vectors in neighboring networks. In addition, by applying Gaussian correction technique to vectors in the flow field, velocity vector at any network point is made more compatible with neighboring vectors. As a result of the researches, the particle image velocitymetry technique does not distribute the solid particles uniformly, the particles overlap when the image is taken, the particles move out of the laser plane at the time of image capture or the particles outside the plane enter the laser plane, the size of the area where the velocity vectors are calculated, electronic and optical total caused by noise It is stated that the uncertainty value is less than 2%. As can be understood from here, the accuracy of the results obtained from this technique gives more accurate results than other velocity measurement techniques.

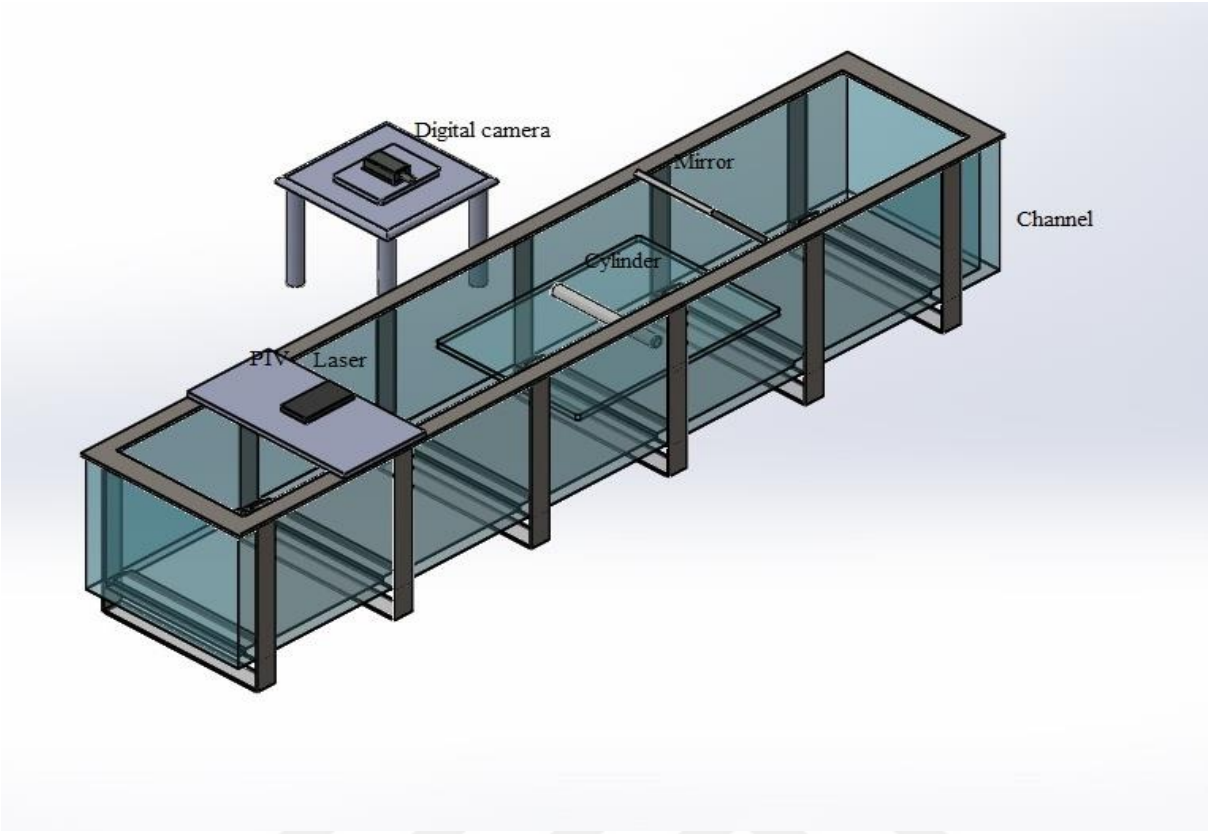

Figure. 3.4**.** Experimental setup used in particle imaging velocity technique experiments

4. RESULTS AND DISCUSSIONS

4.1. Dye Results

In this section, the results obtained from the dye experiment are represented. Fig. 4.1-4.27 show the dye test results for cylinders at all heights and angles. It is seen that the dye test results of bare and triangular shape grooved cylinders for h: 0 mm in Fig. 4.1. Vortex is observed for bare and at a: 95^o for triangular grooved cylinders. Furthermore, for a: 95^o triangular grooved cylinder, the vortex is smaller than the bare cylinder. Also, the vortex region is seen at the top of the wake region at a: 0^o, 80^o, 85^o and 90^o for triangular grooved cylinders. In Fig. 4.2, the dye experiment results of the bare and triangular shape grooved cylinders for the h: 7.5 mm are compared. It has been observed that the effect of the vortex formation of the h: 0 mm is greater than bare cylinder of h: 7.5 mm. When the groove positions of the h: 7.5 mm triangular shape grooved cylinders are compared, it is found that the vortex formation for a: 80^o is less than the other groove angles.

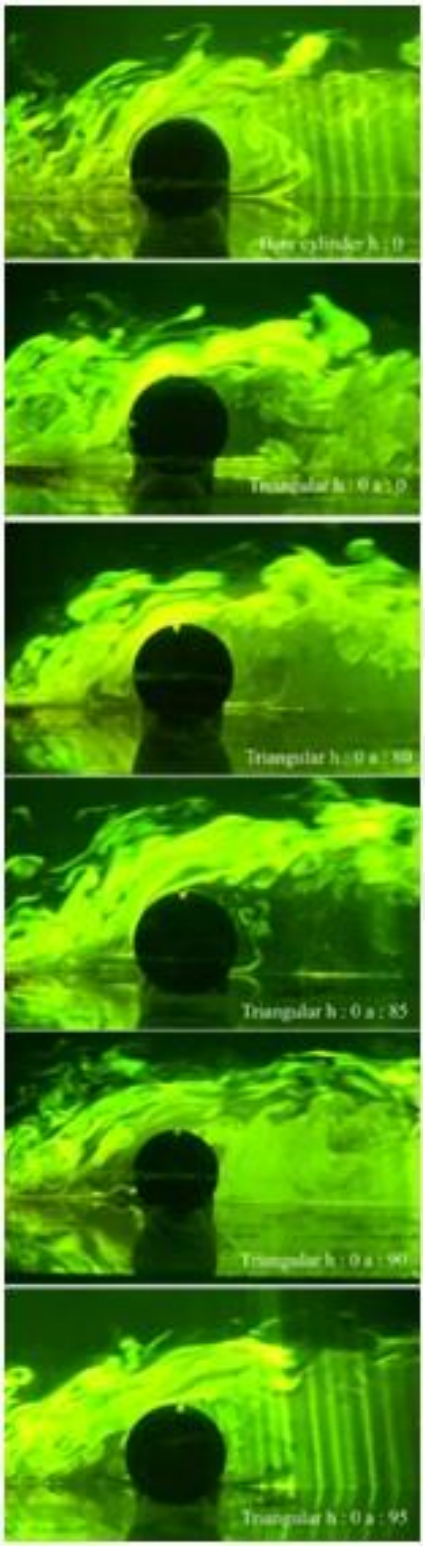

Figure. 4.1. Schematic displaying of flow structure in the downstream of the triangular grooved cylinders for h: 0 mm situations.

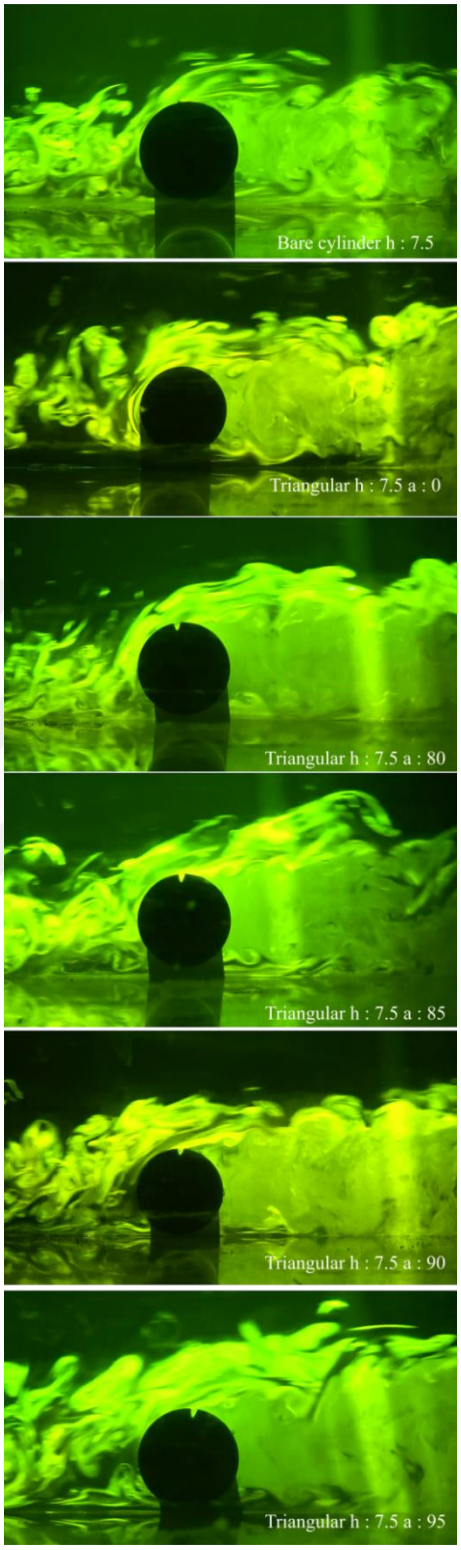

Figure. 4.2. Schematic displaying of flow structure in the downstream of the triangular grooved cylinders for h: 7.5 mm situations.

In Fig. 4.3, the dye test results of bare and triangular cylinders for h: 15 mm is showed. The smallest wake region zone is observed at h:15 mm for the bare cylinder. Besides, at a: 80^o and 90^o, the vortex formation occurs oscillation up and down, while for the other angles at h: 15 mm, it is formed in a single alignment compared to bare cylinder. Also, vortex formations occur oscillation up and down in h: 15 mm at a: 95^o. In Fig. 4.4, the dye test results of bare and triangular cylinders for h: 22.5 mm is showed. For h: 22.5 mm, it has been observed that surface effect has decreased compared to h: 0mm. 7.5mm and 15 mm. Also, a sudden rupture of the vortex is seen at a: 90^o. Also, a rapture is observed in the vortex region at a: 85^o, although not up to a: 90^o due to symmetrical angle position at a :90^o.

In Fig. 4.5, the dye test results of bare and triangular cylinders for h: 30 mm are shown. The Kármán vortex streets (KVS), as described in the literature, are most clearly seen at h: 30 mm compared to other heights due to sudden vortex rupture like the study of Ozgoren et al. (2011). For the bare and at a: 95^o for triangular grooved cylinders clearly show that the vortex formation forms up and down directions in the wake region, respectively. Even if the same situation is seen at a: 0^o, 80^o, 85^o and 90^o, not as much as bare and a: 95^o. In Fig. 4.6, the dye test results of bare and triangular cylinders for h: 37.5 mm is shown. The cylinder begins to approach the water surface at h: 37.5 mm. The vortexs formed in the wake region hit the surface and change direction. Therefore, surface effects are observed on the vortex formation and direction. It is seen clearly that oscillation accrued at the bare cylinder, a: 0^o, a: 7.5^o, a: 90^o and a: 95^o. Also, in this oscillation, the closest direction change to the cylinder is at a: 95^o.

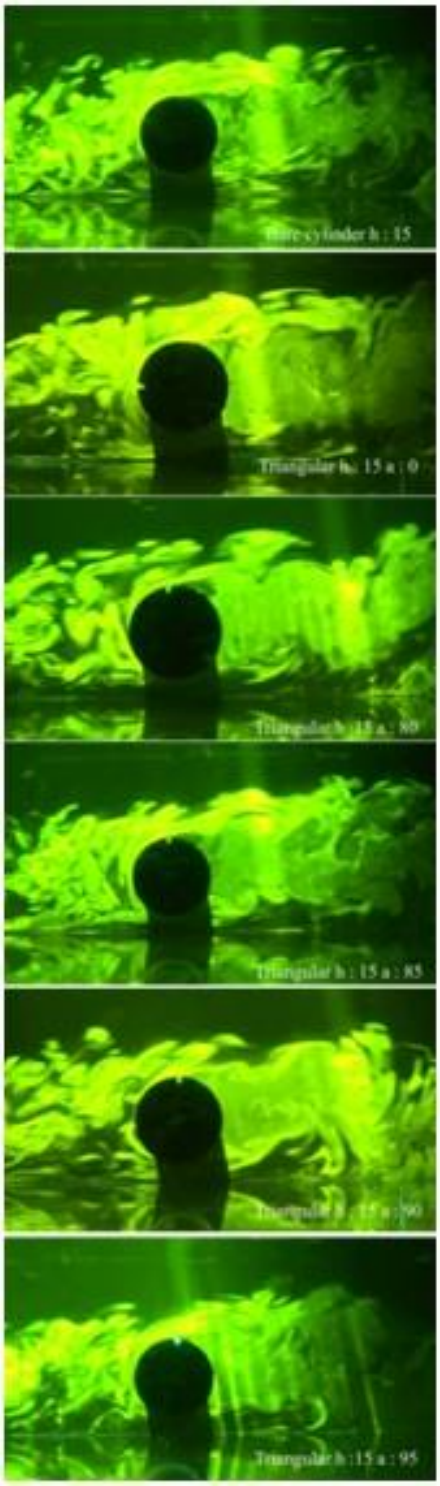

Figure. 4.3. Schematic displaying of flow structure in the downstream of the triangular grooved cylinders for h: 15 mm situations.

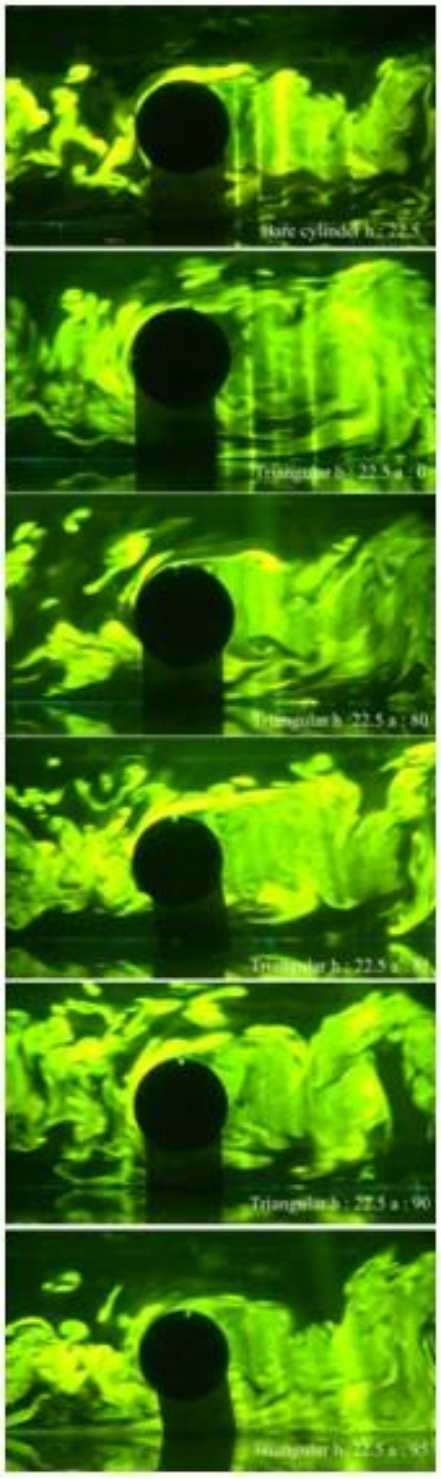

Figure. 4.4. Schematic displaying of flow structure in the downstream of the triangular grooved cylinders for h: 22.5 mm situations.

In Fig. 4.7, the dye test results of bare and triangular cylinders for h: 45 mm is shown. Due to surface effect, the formation of the vortex in the upper part of the cylinder is higher than the lower part in h: 45 mm bare cylinders. Also, it is observed that in cylinders with a: 90 and a: 95, flow separation occurs later, as the groove is further forward. For this reason, it is observed that vortices formed larger. In Fig. 4.8, the dye test results of bare and triangular cylinders for h: 52.5 mm is shown. Due to the surface effect of h: 52.5 mm, vortex formation is not observed in the upper part of the bare cylinder and a: 95^{o}. Also, it is observed that the vortex is not fully formed in the lower part of the bare cylinder compared to the same height triangular grooved cylinders. Besides, the most prominent vortex formation on the upper side of the cylinder is observed at a: 0^{o}. In Fig. 4.9, the dye test results of bare and triangular cylinders for h: 60 mm is shown. At this height, it is seen that the surface effect greatly prevents the formation of the vortex at the top of the cylinder. This means that the vortex exists only below part of the cylinders, due to the proximity of the cylinders to the flow surface. Because of the grooves' proximity to the flow surface, it is found that the grooves have no significant effect on the flow.

In Fig. 4.10, the dye experiment results of bare and square grooved cylinders for h: 0 mm are compared. Looking at these results, the formation of Karman vortex is observed at a: 0^{o} for square grooved cylinders. On the other hand, the formation of vortex at other angles is not evident. In Fig. 4.11, the dye experiment results of bare and square grooved cylinders for h: 7.5 mm are compared. As can be seen from the figure, it is determined that the vortex formation for a: 80 is less than the other groove angles when the groove positions of the square grooved cylinders positoned in h: 7.5 mm are compared.

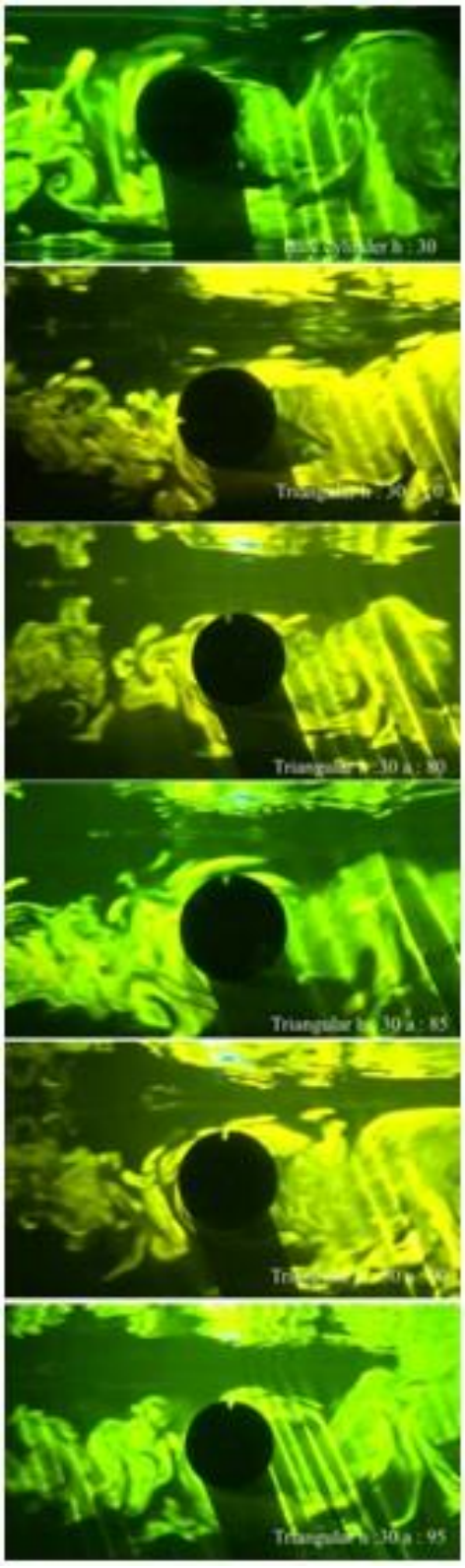

Figure. 4.5. Schematic displaying of flow structure in the downstream of the triangular grooved cylinders for h: 30 mm situations.

Figure. 4.6. Schematic displaying of flow structure in the downstream of the triangular grooved cylinders for h: 37.5 mm situations.

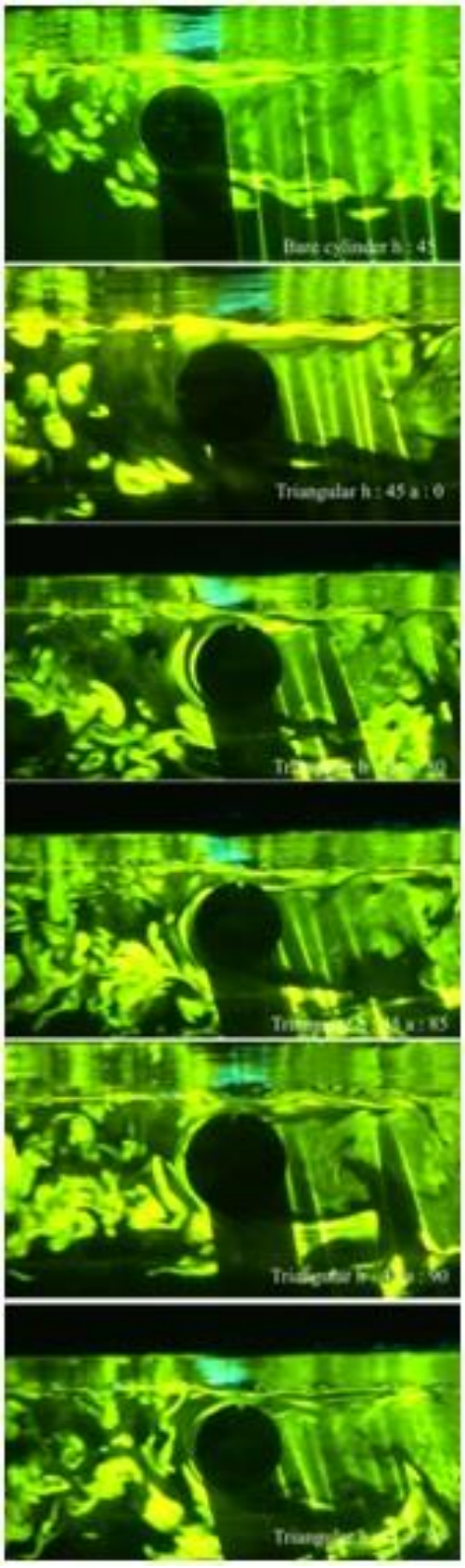

Figure. 4.7. Schematic displaying of flow structure in the downstream of the triangular grooved cylinders for h: 45 mm situations.

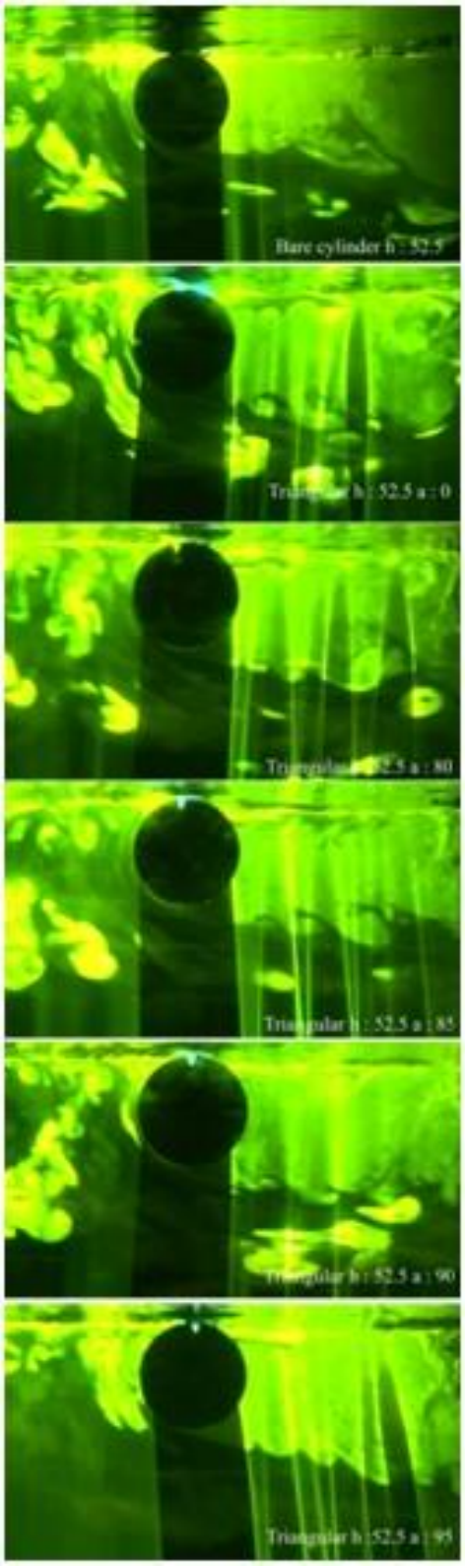

Figure. 4.8. Schematic displaying of flow structure in the downstream of the triangular grooved cylinders for h: 52.5 mm situations.

Figure. 4.9. Schematic displaying of flow structure in the downstream of the triangular grooved cylinders for h: 60 mm situatins.

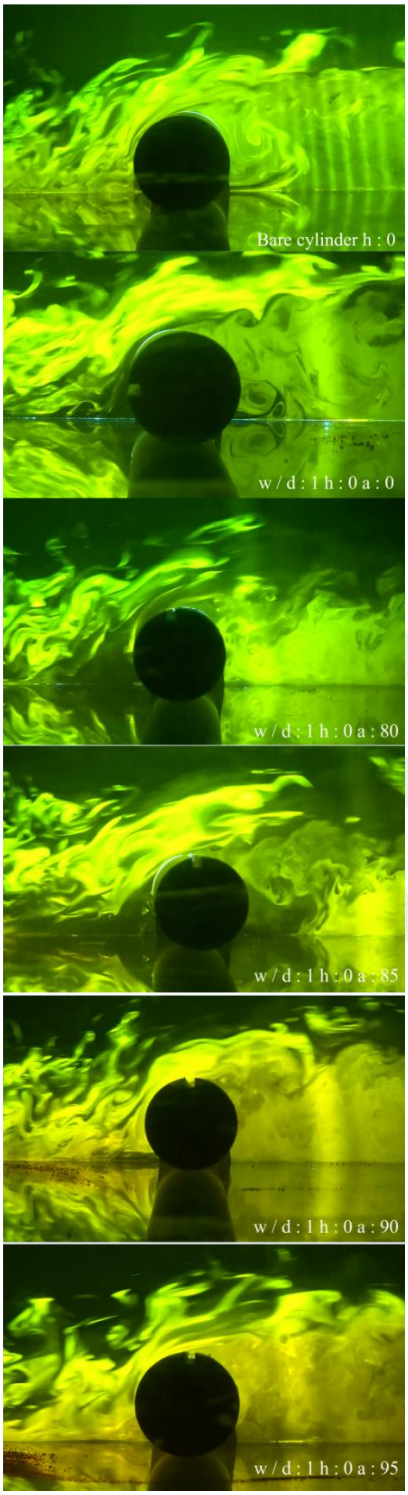

Figure. 4.10. Schematic displaying of flow structure in the downstream of the square grooved cylinder for h: 7.5 mm situations

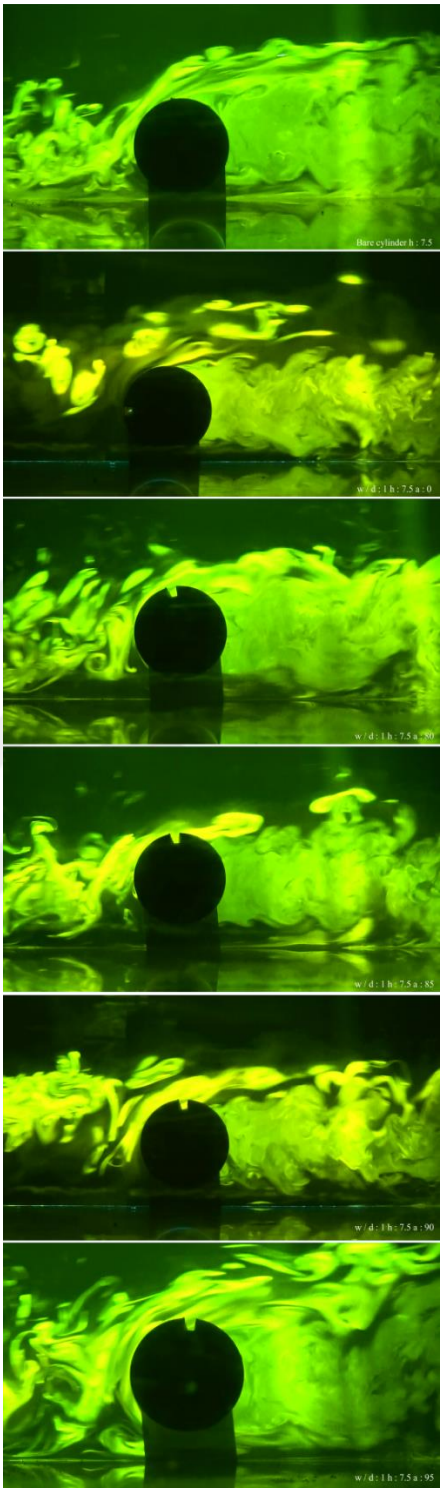

Figure. 4.11. Schematic displaying of flow structure in the downstream of the square grooved cylinder for h: 7.5 mm situations

.

In Fig. 4.12, the dye experiment results of bare and square grooved cylinders for h: 15 mm are compared. When comparing the h: 15 mm square grooved cylinders with respect to the groove angles, it is observed that it is similar to the h: 15 mm for a: 0^o and a: 95^o, with minimal wake region formation. In Fig. 4.13, the dye experiment results of bare and square grooved cylinder for h: 22.5 mm are compared. It is observed that the vortex effect is felt more at a: 90^o when compared to the square shape grooved cylinders of h: 22.5 mm.

In Fig. 4.14, the dye experiment results of bare and square grooved cylinders for mm h: 30 are compared. It has been observed that making a square recess in the cylinder for mm h: 30 significantly reduces the formation of vortex at all angles. Vortex formation is minimal, especially at an angle a: 80 where flow separation occurred earlier. In Fig. 4.15, the dye experiment results of bare and square shape cylinders for h: 37.5 mm are compared. When the square-grooved cylinders with a of h: 37.5 mm are compared according to the groove angles, it is observed that the flow structure behind the cylinder does not change much according to the angles.

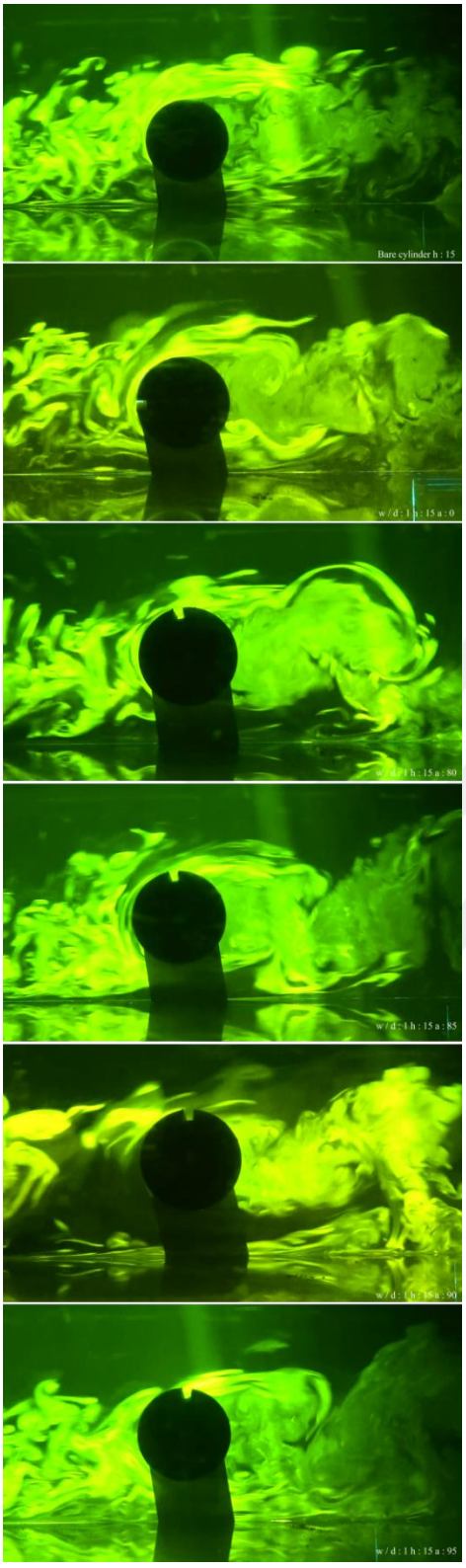

Figure. 4.12. Schematic displaying of flow structure in the downstream of the square grooved cylinder for h: 15 mm situations

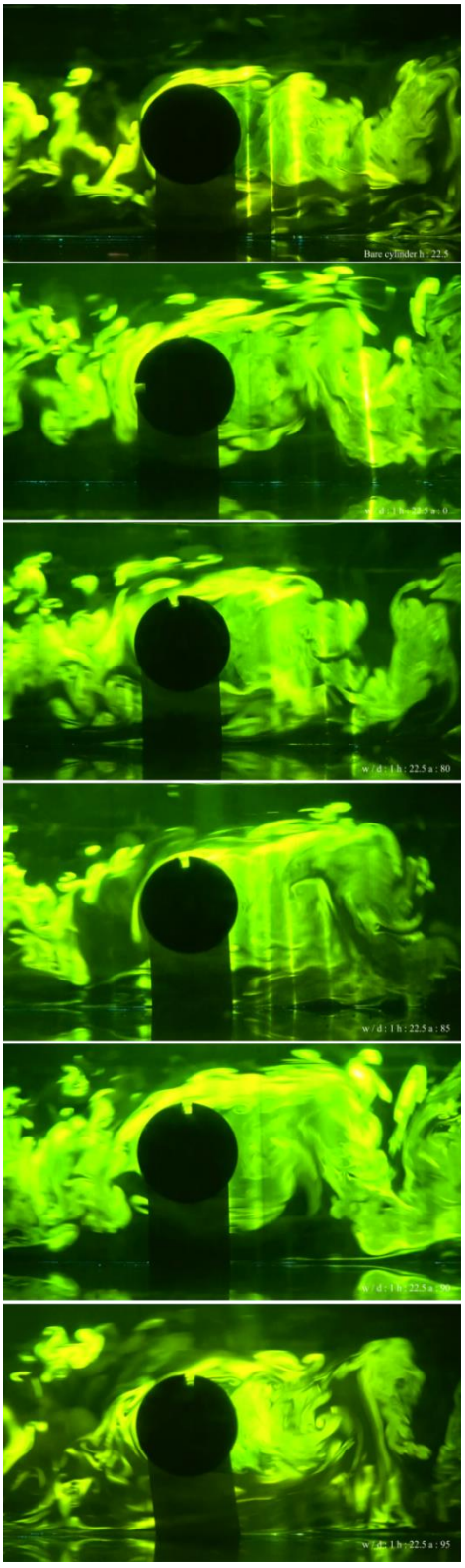

Figure. 4.13. Schematic displaying of flow structure in the downstream of the square grooved cylinder for h: 22.5 mm situations.

In Fig. 4.16, the dye experiment results of bare and square grooved cylinders for h: 45 mm are compared. Considering the square grooved cylinders with a of h: 45 mm, the vortex formation is more pronounced in the cylinder with a groove in the a: 0 angle compared to the cylinders at other angles. In Fig. 4.17 and 4.18, the dye experiment results of cylinders without hollow and square shape cylinder for h: 52.5 and h: 60 mm are compared. As with the triangular shape grooved cylinders, it has been observed that the groove has no noticeable effect on the flow due to their proximity to the flow surface.

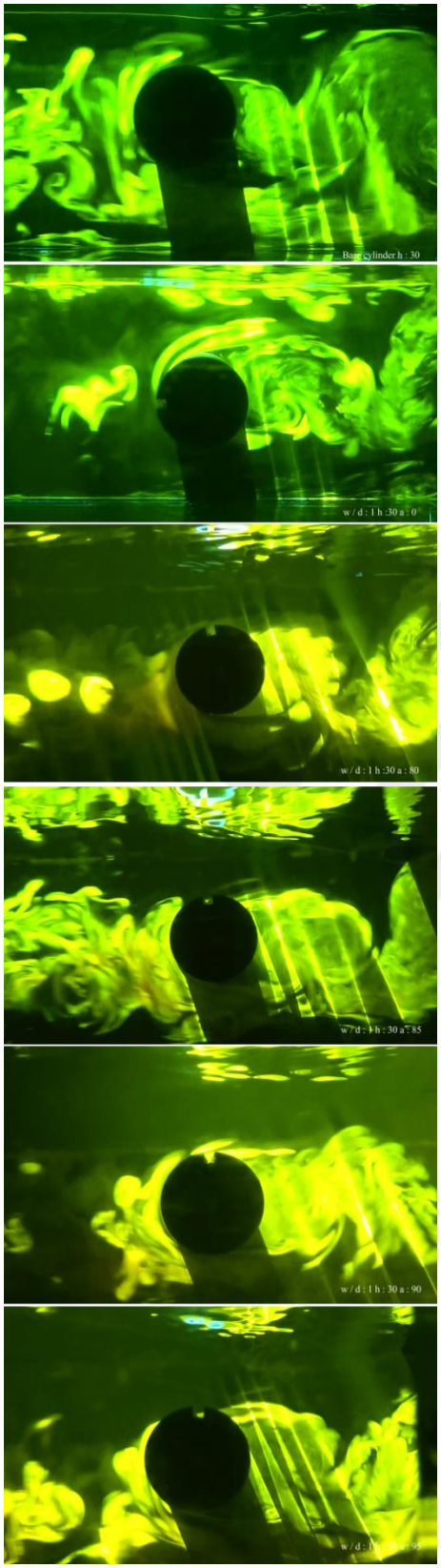

Figure. 4.14. Schematic displaying of flow structure in the downstream of the square grooved cylinder for h: 30 mm situations.

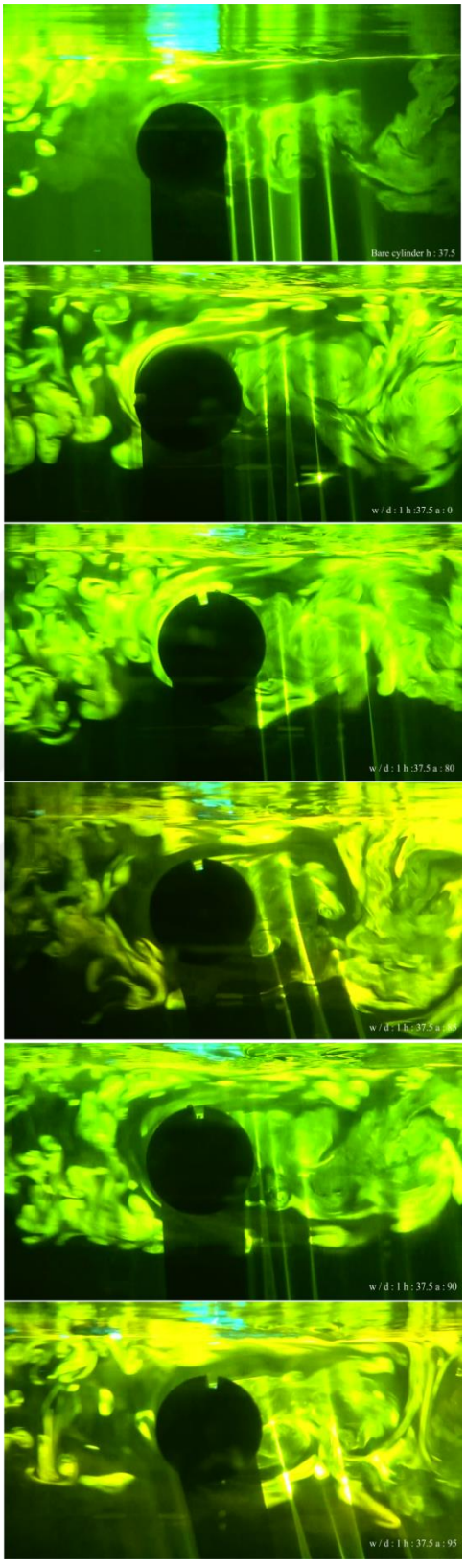

Figure. 4.15. Schematic displaying of flow structure in the downstream of the square grooved cylinder for h: 37.5 mm situations.

In Fig.4.19, the dye experiment results of bare and rectangular grooved cylinder for h: 0 mm are compared. Looking at these results, the formation of Karman vortex is observed at a: 0^o for rectangular shape grooved cylinder. On the other hand, the formation of vortex at other angles is not evident. In Fig.4.20, the dye experiment results of bare and rectangular grooved cylinders for h: 7.5 mm are compared. As can be seen from the Fig. 4.20, when the grooved angle positions of the h: 7.5 mm rectangular grooved cylinders are compared, it is determined that the vortex formation for a: 80^o is less than the other groove angles.

In Fig.4.21, the dye experiment result of bare and rectangular grooved cylinders for h: 15 mm are compared. Comparing the h: 15 rectangular grooved cylinders with respect to the groove angles, it is observed that the vortex formation is minimal at the angle a: 95. In Fig.4.22, the dye experiment result of bare and rectangular grooved cylinders for h: 22.5 mm are compared. When compared to the rectangular grooved cylinders of h: 22.5 mm, it is observed that the vortex effect is felt more at the angle of a: 90.

Figure. 4.16. Schematic displaying of flow structure in the downstream of the square grooved cylinder for h: 45 mm situations

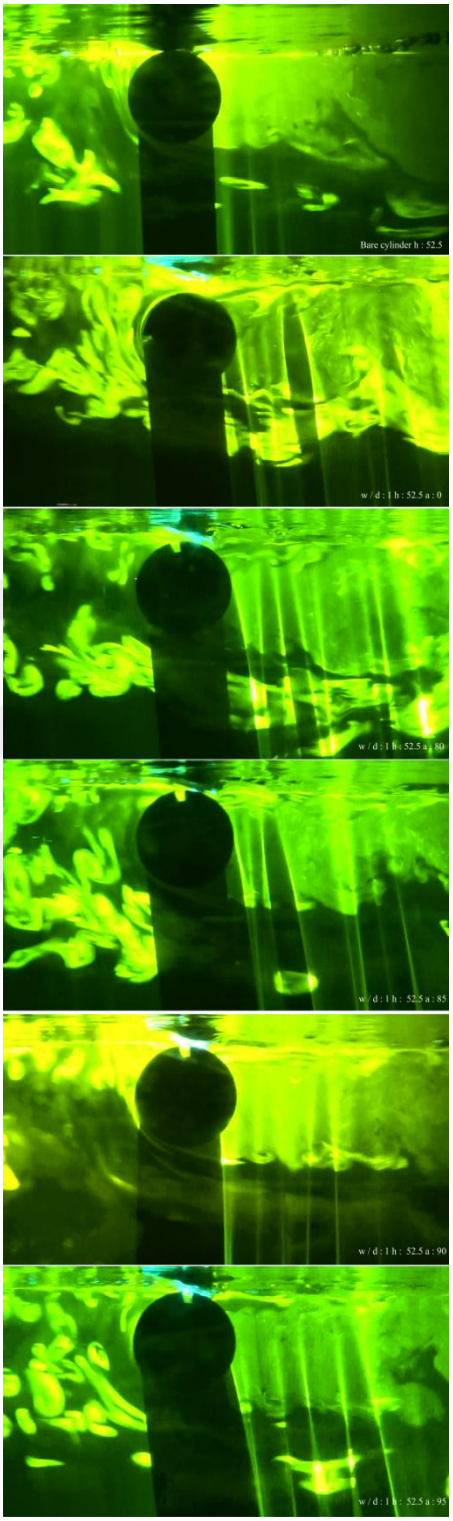

Figure. 4.17. Schematic displaying of flow structure in the downstream of the square grooved cylinder for h: 52,5 mm situations.

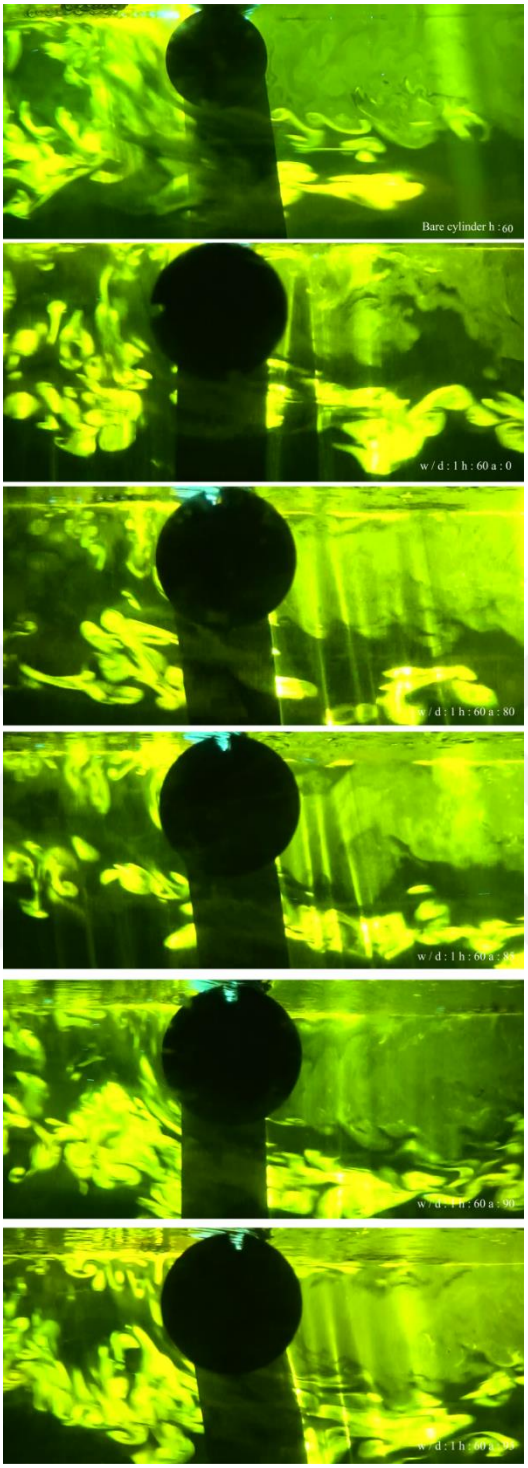

Figure. 4.18. Schematic displaying of flow structure in the downstream of the square grooved cylinder for h: 60 mm situations.

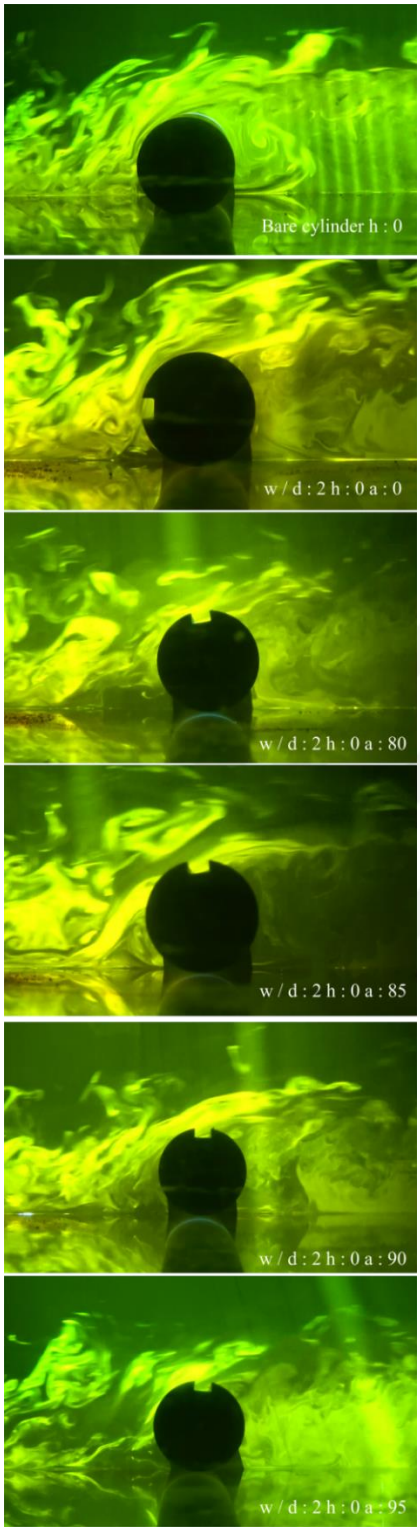

Figure. 4.19. Schematic displaying of flow structure in the downstream of the rectangular grooved cylinder for h: 0 mm situations.

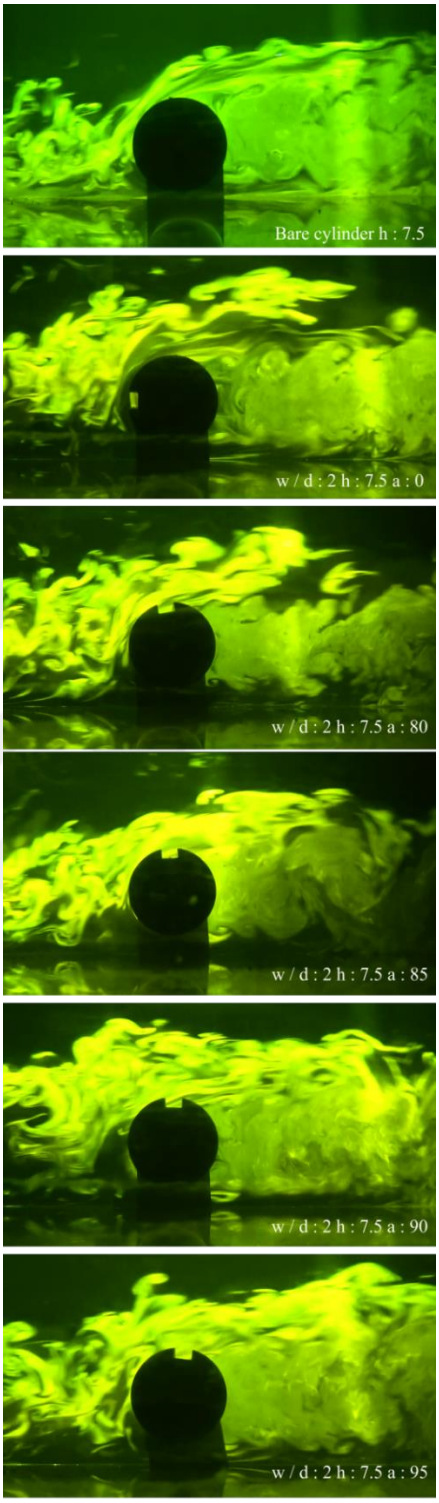

Figure. 4.20. Schematic displaying of flow structure in the downstream of the rectangular grooved cylinder for h: 7.5 mm situations.

In Fig.4.23, the dye experiment results of bare and rectangular grooved cylinders for h: 30 mm are compared. It has been observed that opening a rectangular recess in the cylinder for h: 30 mm significantly reduces the formation of vortex at all angles. In Fig.4.24, the dye experiment results of bare and rectangular grooved cylinders for h: 37.5 mm are compared. When the h: 37.5 high rectangular hollow cylinders are compared according to the groove angles, it has been observed that the flow structure behind the cylinder does not change much according to the angles.

In Fig.4.25, the dye experiment results of bare and w / d: 2 rectangular grooved cylinders for h: 45 mm are compared. When the cylinders with h: 45 mm are evaluated, it is seen that the formation of vortices is less at all angles compared to the angles at other heights. In Fig. 4.26 and 4.27, the dye experiment results of bare cylinder and rectangular grooved cylinder for h: 52.5 and h: 60 mm are compared. It has been observed that the groove has not a significant effect on the flow due to their proximity to the flow surface, and vortex formation is observed only in the lower part of the cylinder.

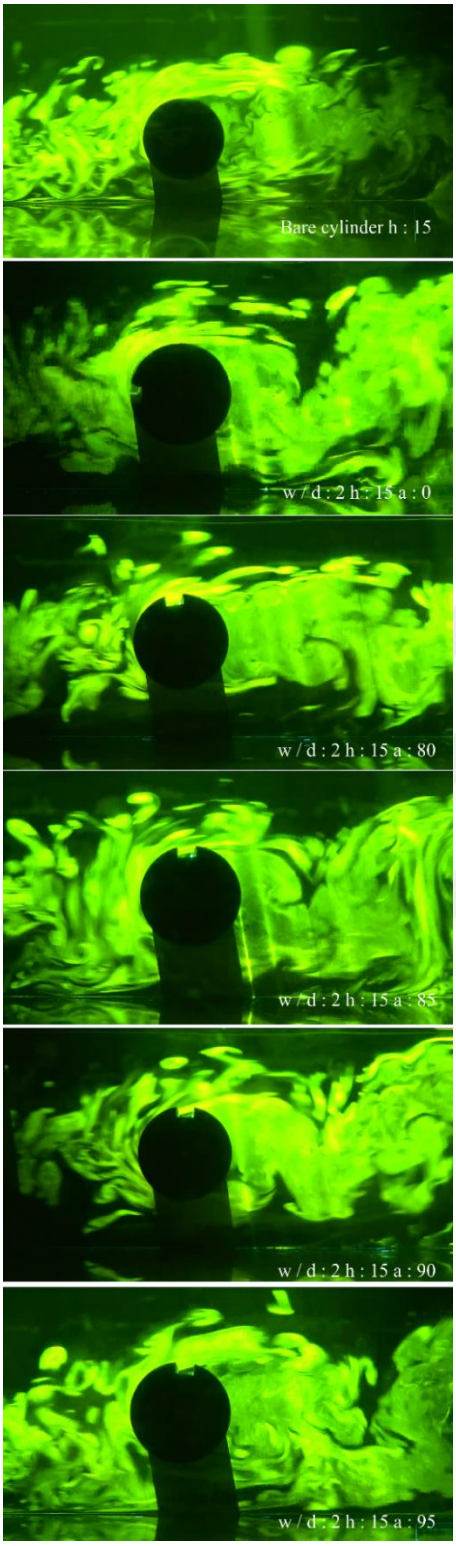

Figure. 4.21. Schematic displaying of flow structure in the downstream of the rectangular grooved cylinder for h: 15 mm situations.

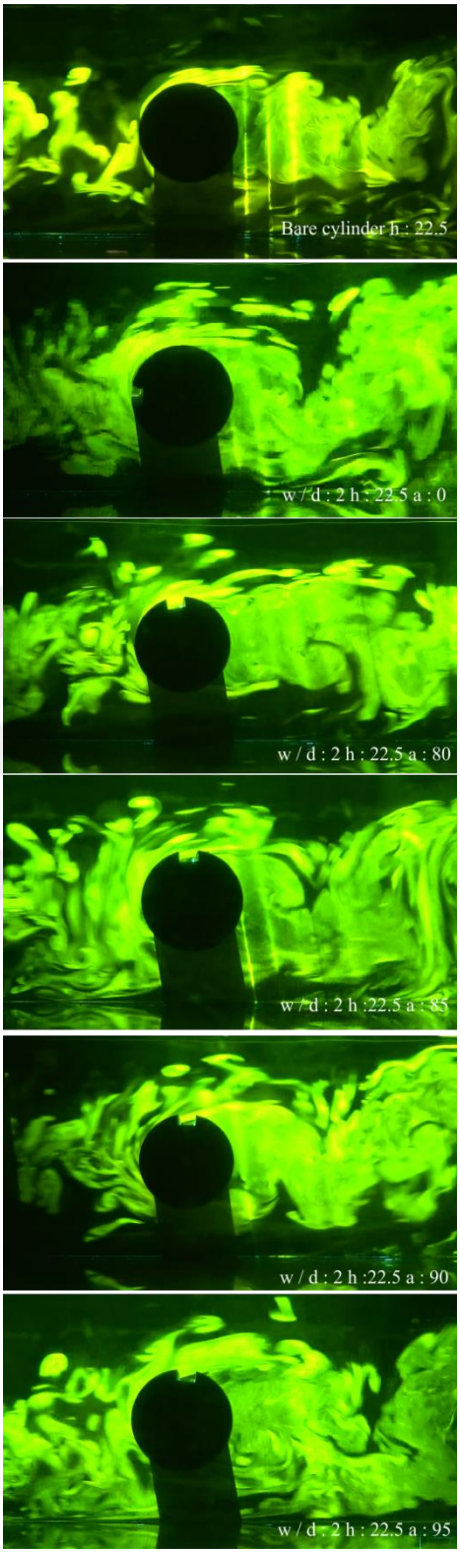

Figure. 4.22. Schematic displaying of flow structure in the downstream of the rectangular grooved cylinder for h: 22.5 mm situations.

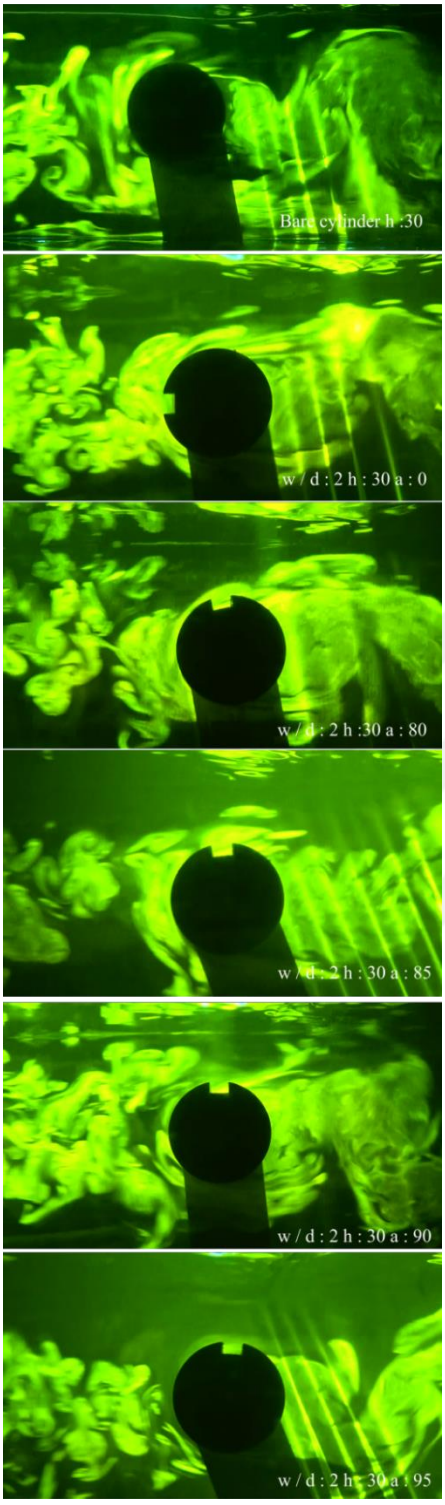

Figure. 4.23. Schematic displaying of flow structure in the downstream of the rectangular grooved cylinder for h: 30 mm situations.

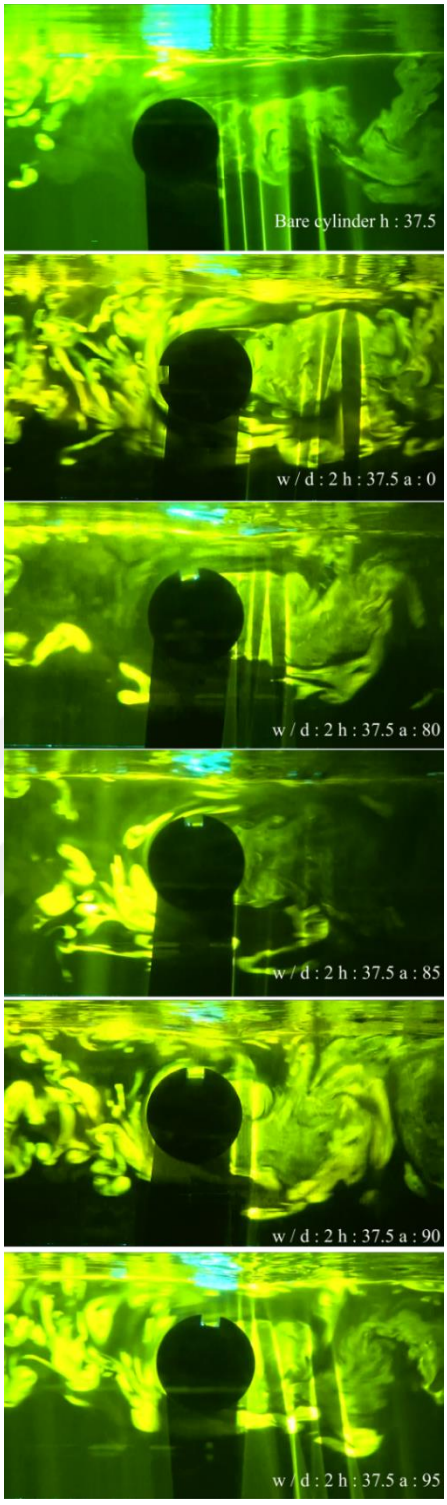

Figure. 4.24. Schematic displaying of flow structure in the downstream of the rectangular grooved cylinder for h: 37.5 mm situations.

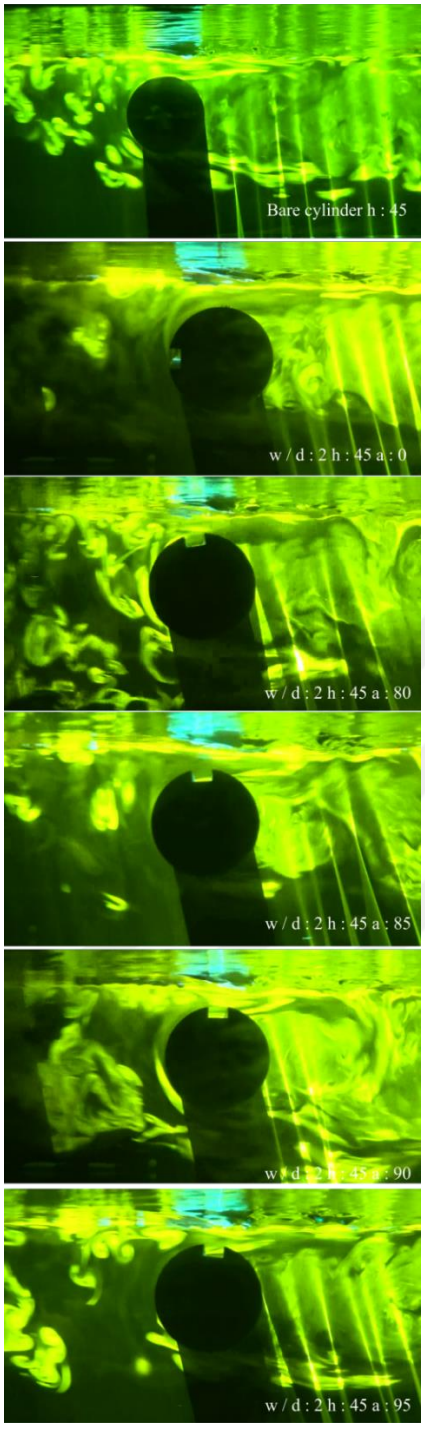

Figure. 4.25. Schematic displaying of flow structure in the downstream of the rectangular grooved cylinder for h: 45 mm situations.

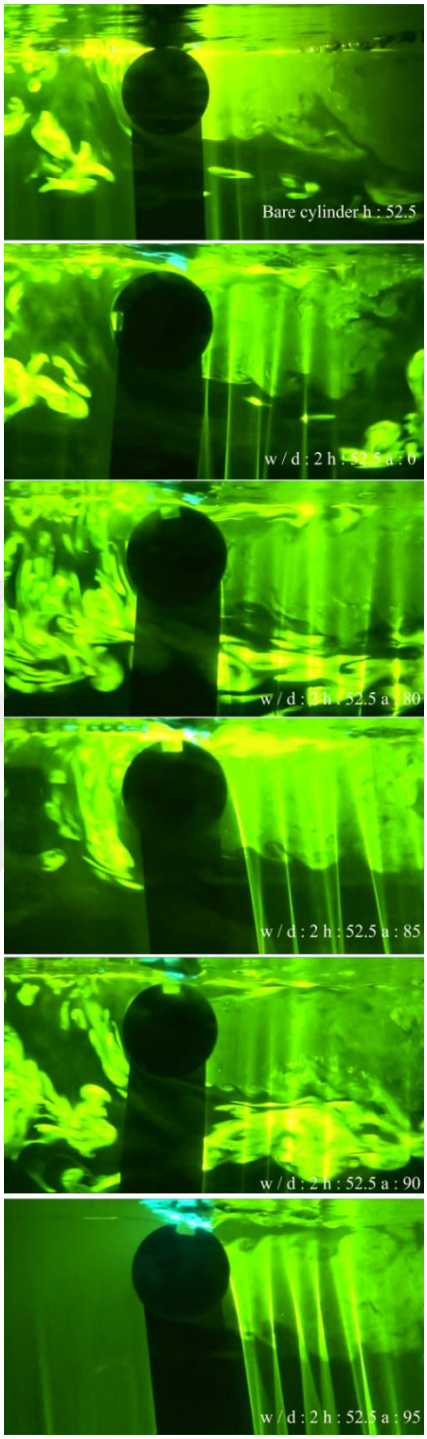

Figure. 4.26. Schematic displaying of flow structure in the downstream of the rectangular grooved cylinder for h: 52.5 mm situations.

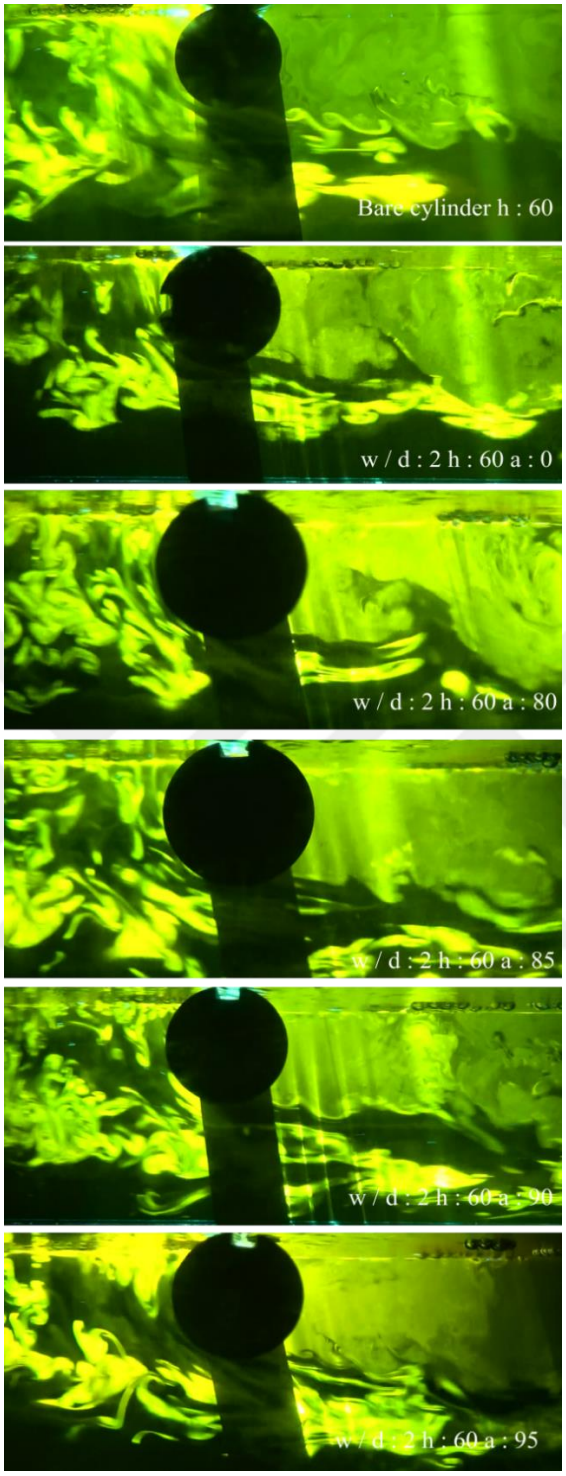

Figure. 4.27**.** Schematic displaying of flow structure in the downstream of the rectangular grooved cylinder for h: 60 mm situations.

4.2. PIV Results

In this section, the results obtained from the PIV experiment are presented. Flow characteristics with the inclusion of Reynolds stress (uv/U^2), time-averaged velocity vectors (<V>) and the corresponding streamline topology (<ψ>) are shown in Fig 4.28. Reynolds stress (uv/U^2) is shown in Fig. 4.28. in the first column while velocity vectors (<V>) is shown in the second column, for the visual low-velocity vector accrue downstream of the cylinders. As can be seen in the first column, however, both negative and positive counter occurs all height at the cylinder, there is only a positive counter appears at h: 0 mm due to the influence of the surface effect. When comparing all cylinders at first column, the maximum negative width and length counter form at h: 37.5 mm. On the other hand, except for h: 52.5 mm and h: 60 mm, more high-velocity vector is observed just around the cylinders. Furthermore, at the bottom of the experimental area at h: 22.5 mm, it's observed that there are more intensive velocity vectors among other test sections. Foci (F) and saddle point (S) (junction of the streamlines) are illustrated in the third column in Fig. 4.28 as time average streamline topology (<ψ>). At this figure., symmetry is obvious at both sides around the cylinder downstream which consistent with the study of Canpolat (2015). Also, two foci points are observed at h: 15 mm, 22.5 mm, 30 mm, 37.5 mm, 45 mm, and 52.5 mm due to the shear layer at the upper side of the cylinder. Although the second foci point is not seen at h: 60 mm, it can be predicted to occur later. On the other hand, swirl could be taking place at h: 0 mm. According to the visual, the biggest wake region is observed at h: 52.5 mm. Furthermore, comparing h: 45mm and h: 52.5 mm, the wake region enlarges in the longitudinal direction at h: 52.5 mm. For this reason, the saddle point occurs later. On the other hand, this region enlarges in the transverse direction at h: 45 mm. Compare with foci points of h: 45 mm; foci points enlarge in the transverse direction at h: 52.5 mm. Moreover, it is observed that the wake region shrinks in the transverse direction at h: 15mm, 22.5 mm, 30 mm and 37.5 mm. Among these heights, the largest wake region is seen at 22.5 mm. Also, at h: 0 mm and 60 mm, wake regions accrue later from other height due to shear layers.

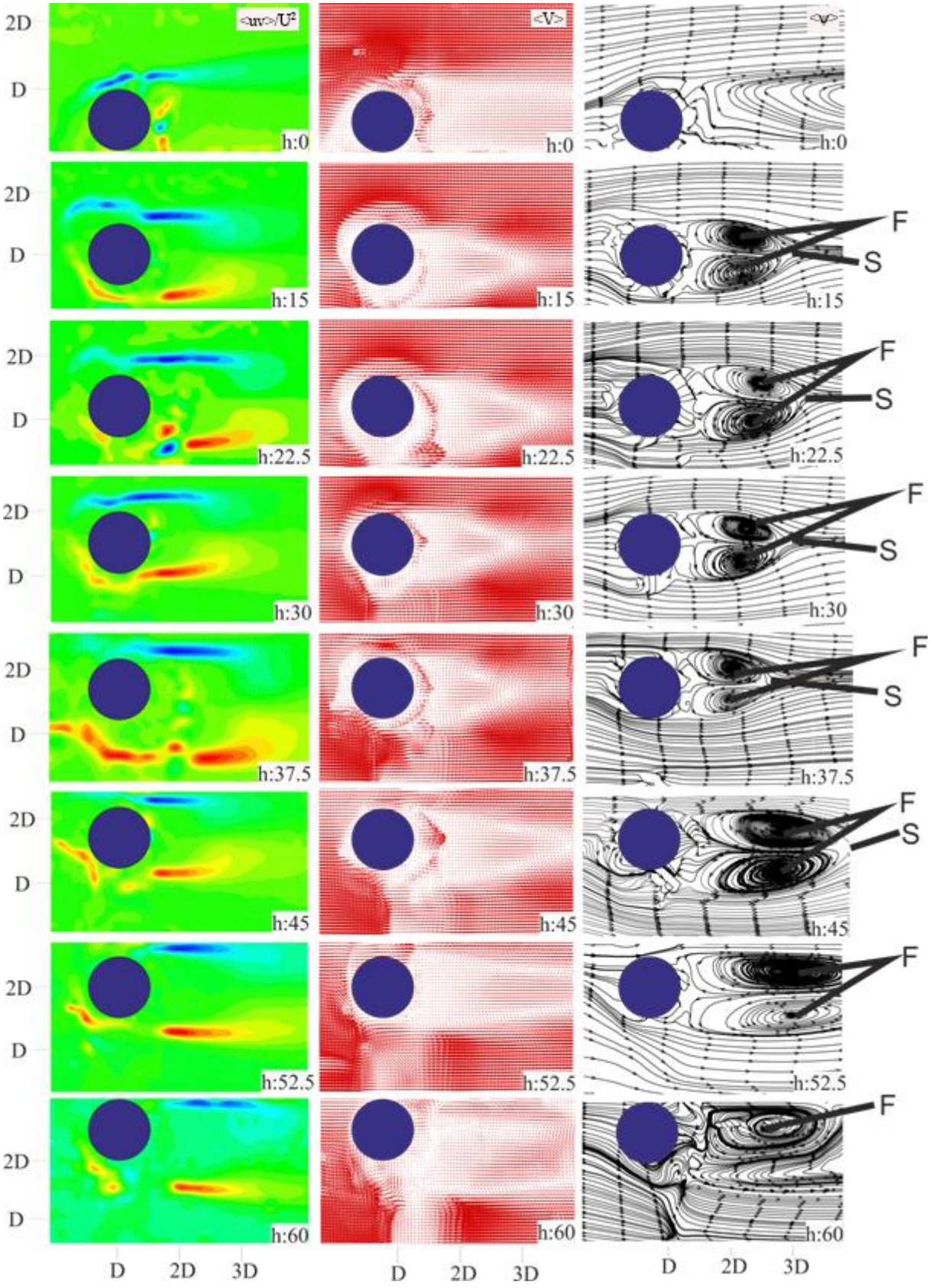

Figure. 4.28. Schematic displaying of flow structure in the downstream of the bare cylinder

Fig. 4.29 illustrates the flow structure in the downstream of the triangular grooved and bare cylinders at h: 0 mm. Also, triangular grooved cylinders rotate clockwise direction with the a: 0^o, 80^o, 85^o, 90^o, and 95^o, respectively. At first column in Fig. 4.29, the biggest negative counter is observed at the situation of the a: 90^o. Only a positive counter accrued near the cylinders is seen at the bare cylinder and a: 0^o. While the negative counter is observed 3h/2 from the cylinder at a: 80^o, 90^o and h/2 from the cylinder at a: 85^o and 95^o. Furthermore, since separation taking place where groove at the cylinder, as the angle is chanced, separation accrue far behind of the flow. The density of the velocity vectors appears to be fast at the point where the flow break occurs on the upper surface of the cylinder at the second column. Moreover, it is observed that the velocity vector behind the cylinders like the second column in Fig. 4.28. According to the third column in Fig. 4.29, swirl takes place at a: 0^o like a bare cylinder. Moreover, it is observed wake region accrues after a: 0^o. There are two foci points and saddle point in four angles. a: 80^o and 90^o compared to a: 85^o and 95^o, it can be seen that the vortex starting point is far behind from a: 85^o and 95^o.

Fig. 4.30 illustrates bare and triangular grooved cylinder experiments positioned in h: 15 mm with different angles. As can be seen in the first column in this figure, Reynolds stress accrues different configurations from h: 0 mm. It can be predicted that the reason for this phenomenon is the bottom effect. At the a: 0^o and 95^o, the positive counter exhibits constant flow while at the: 80^o, 85^o and 90^o, fragile accrue at the positive column. Furthermore, the negative and positive columns at all bare cylinders accrue near the cylinders. On the other hand, at bare cylinders, these counters are carried away from the cylinder. Also, it has been observed that the velocity vectors take place just behind the cylinder, while the bare cylinder is further back. It can be undoubtedly seen that there is saddle and foci point at last column all visual. Comparing the results of the experiment as shown in the image, the wake region is the closest to the cylinder where the: 0^o.

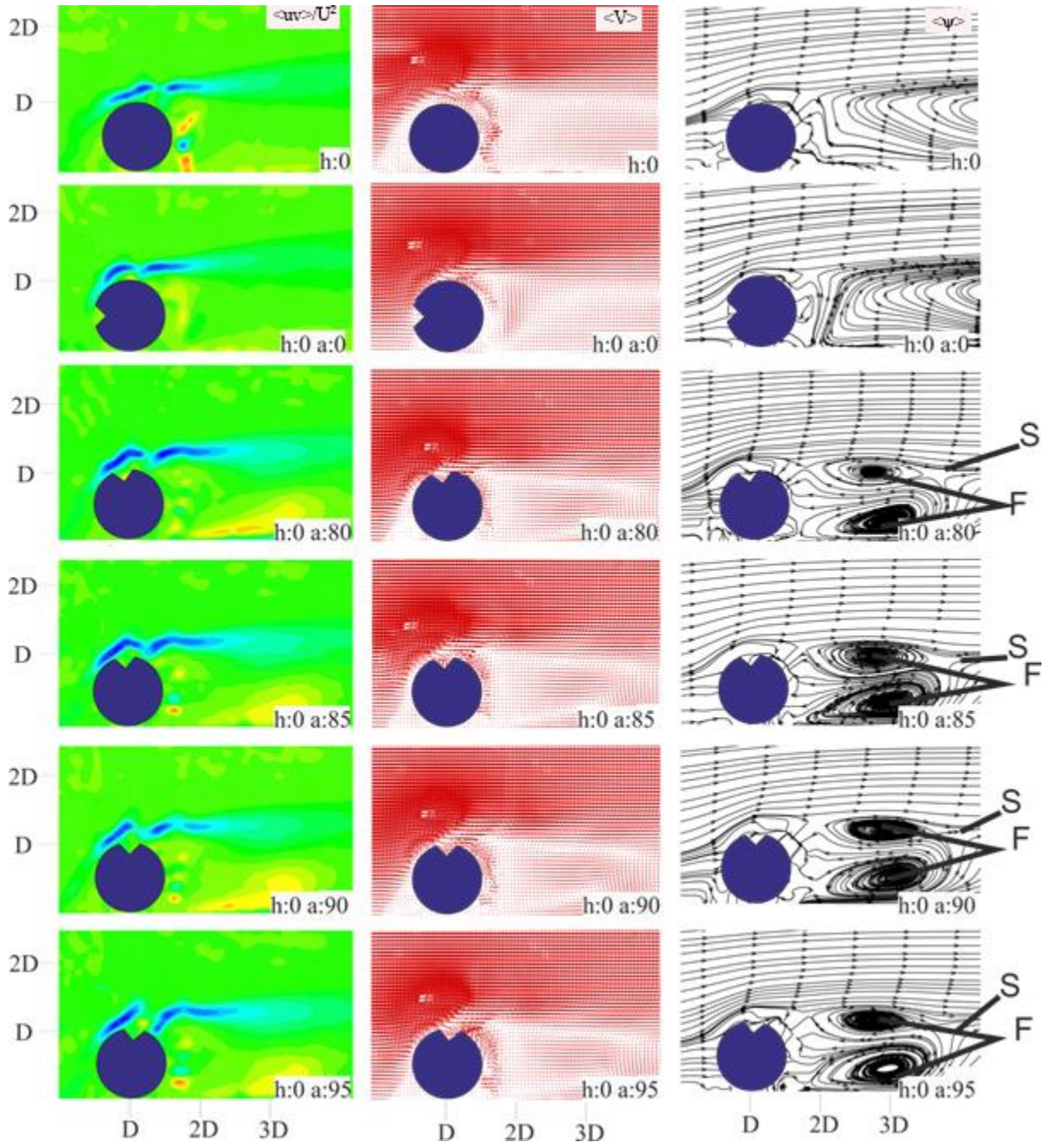

Figure. 4.29. Schematic displaying of flow structure in the downstream of the triangular grooved cylinders for h: 0 mm situations.

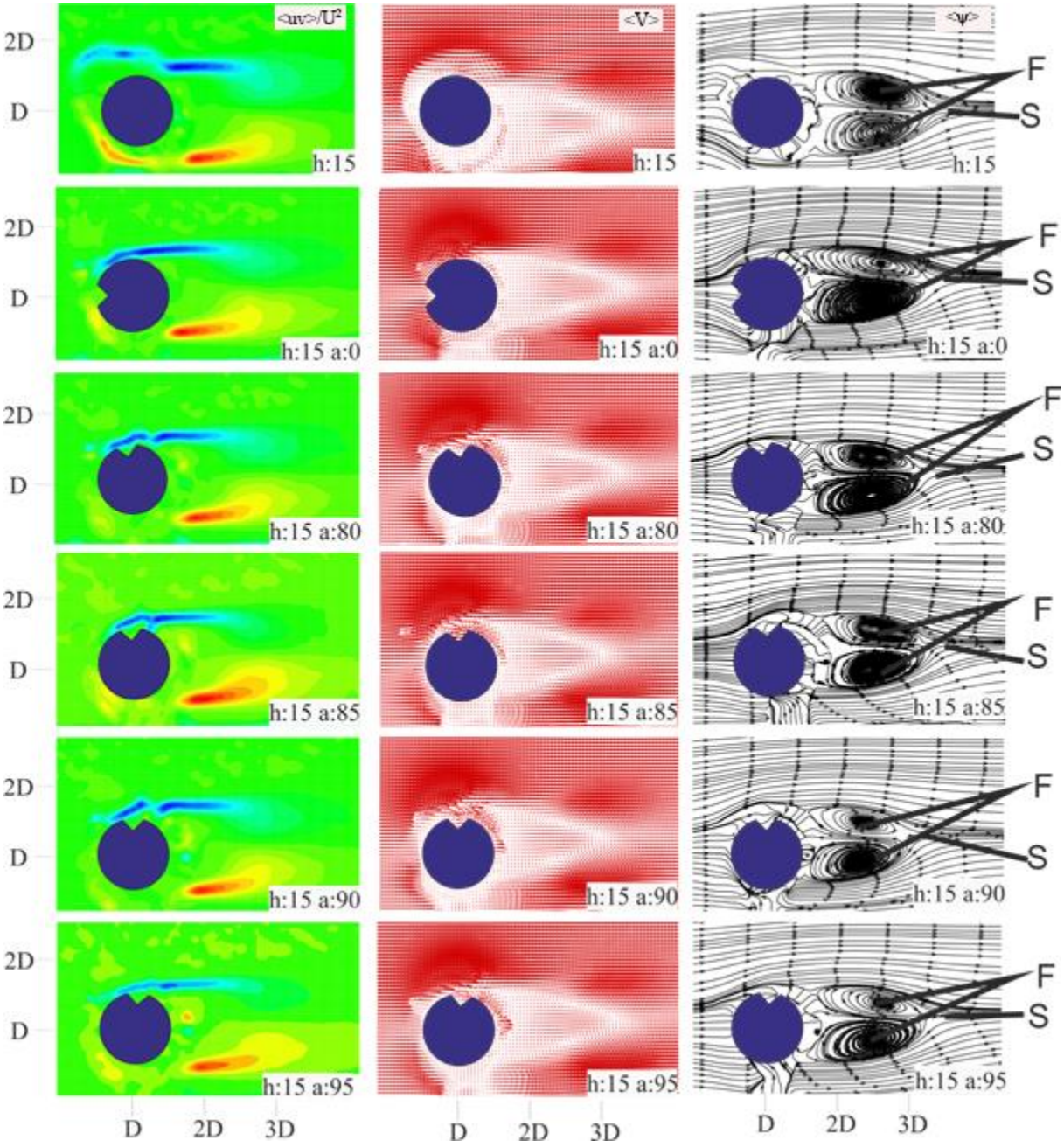

Figure. 4.30. Schematic displaying of flow structure in the downstream of the triangular grooved cylinders for h: 15 mm situations.

It is seen that at the first column negative counters occur almost the same size in all cylinders in Fig. 4.31 showing comparison between bare cylinder and triangular cyling positioned in h: 22.5 mm. It is observed there are velocity vectors around cylinders like other height but not seen at a: 0^o in h: 22.5 mm. Furthermore, F and S are observed for all angles and bare cylinder.

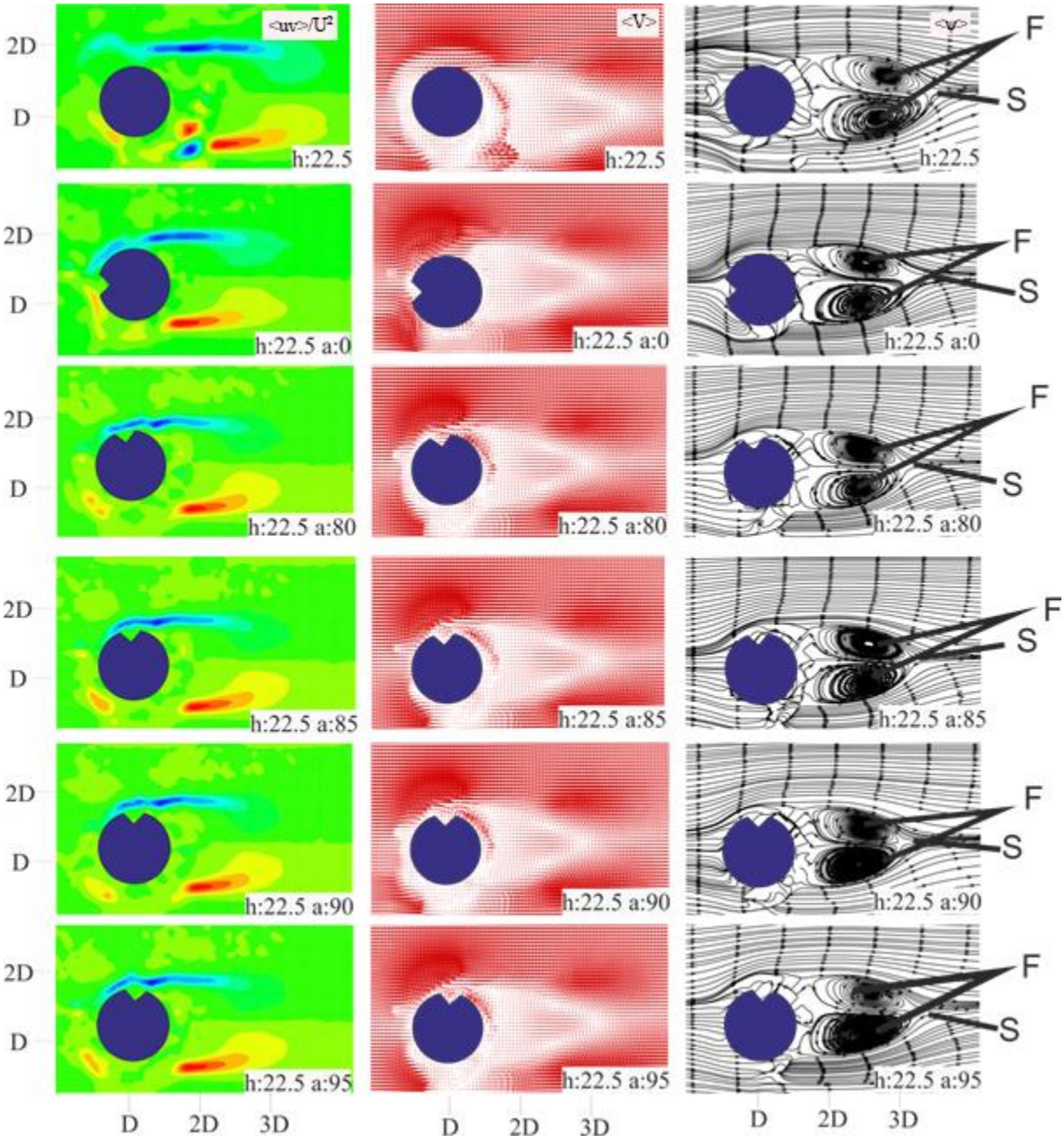

Figure. 4.31. Schematic displaying of flow structure in the downstream of the triangular grooved cylinders for h: 22.5 mm situations.

In this experiment at h: 30 mm means that the center of the cylinder corresponds to the center of the water height. Compare bare and grooved cylinders at first column, although the positive counter at bare cylinder accrues further in the cylinder, it is formed closer to the cylinder in the grooved. Velocity vectors (V), shown the second column, illustrate the low-velocity region which represents the wake region just downstream of the cylinders. This means that velocity vectors are slow in the rear flow zone of the cylinder. Wake regions accrue symmetric in the last column. Moreover, it is not seen as a big difference between the wake regions for all angles.

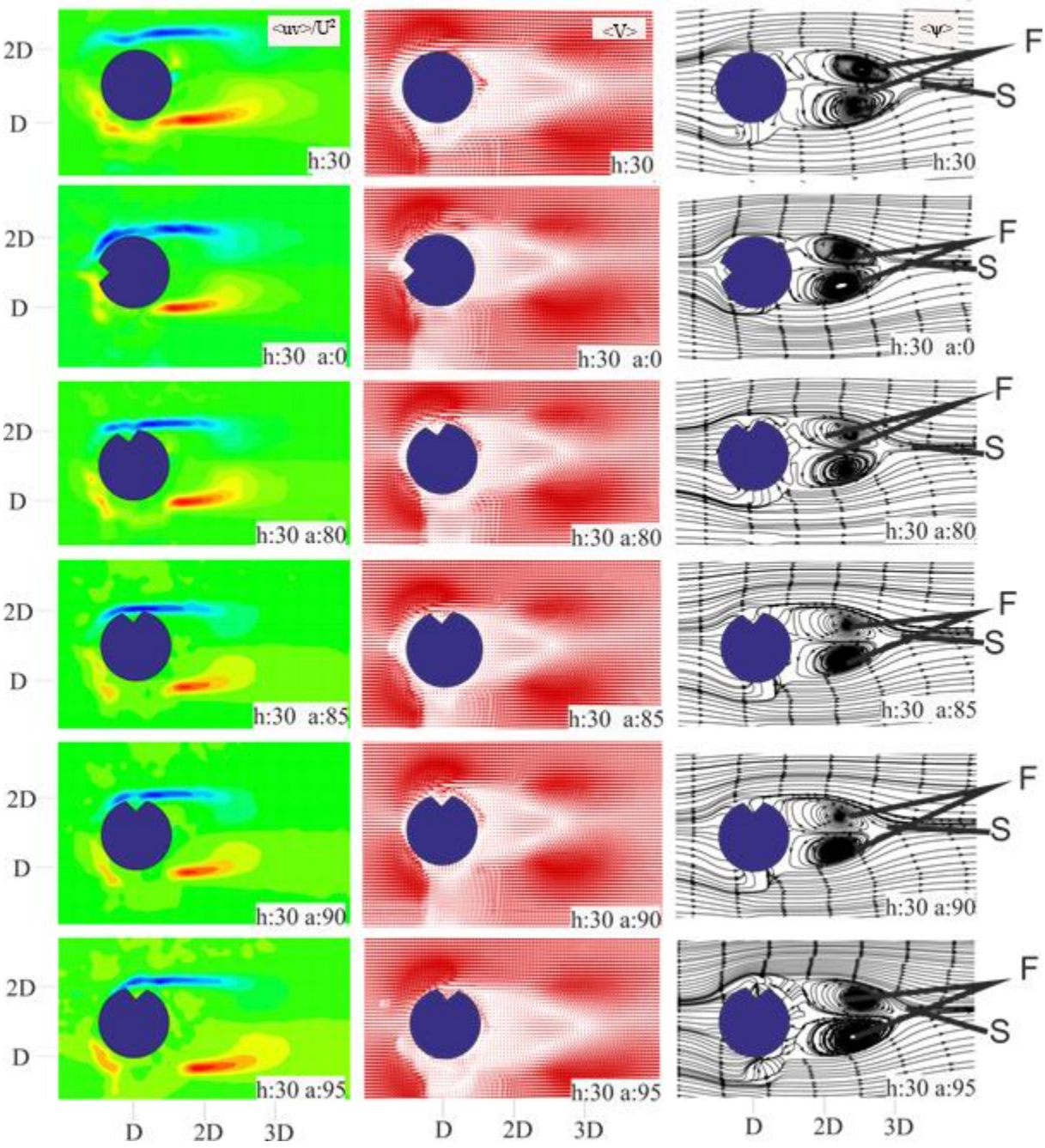

Figure. 4.32. Schematic displaying of flow structure in the downstream of the triangular grooved cylinders for h: 30 mm situations.

In Fig.4.33, a positive counter in a bare cylinder takes up more space than grooved cylinders. Also, compared to other height, negative contours have the largest and longest area at first column in this figure. Velocity vectors, presenting in the second column, show a low-velocity region which represents the wake region which represents the wake region downstream of the cylinders like other heights. Besides, some velocity vectors accrue backward of the cylinders, expected in angle of zero. Foci point can be seen in the last column in this visual.

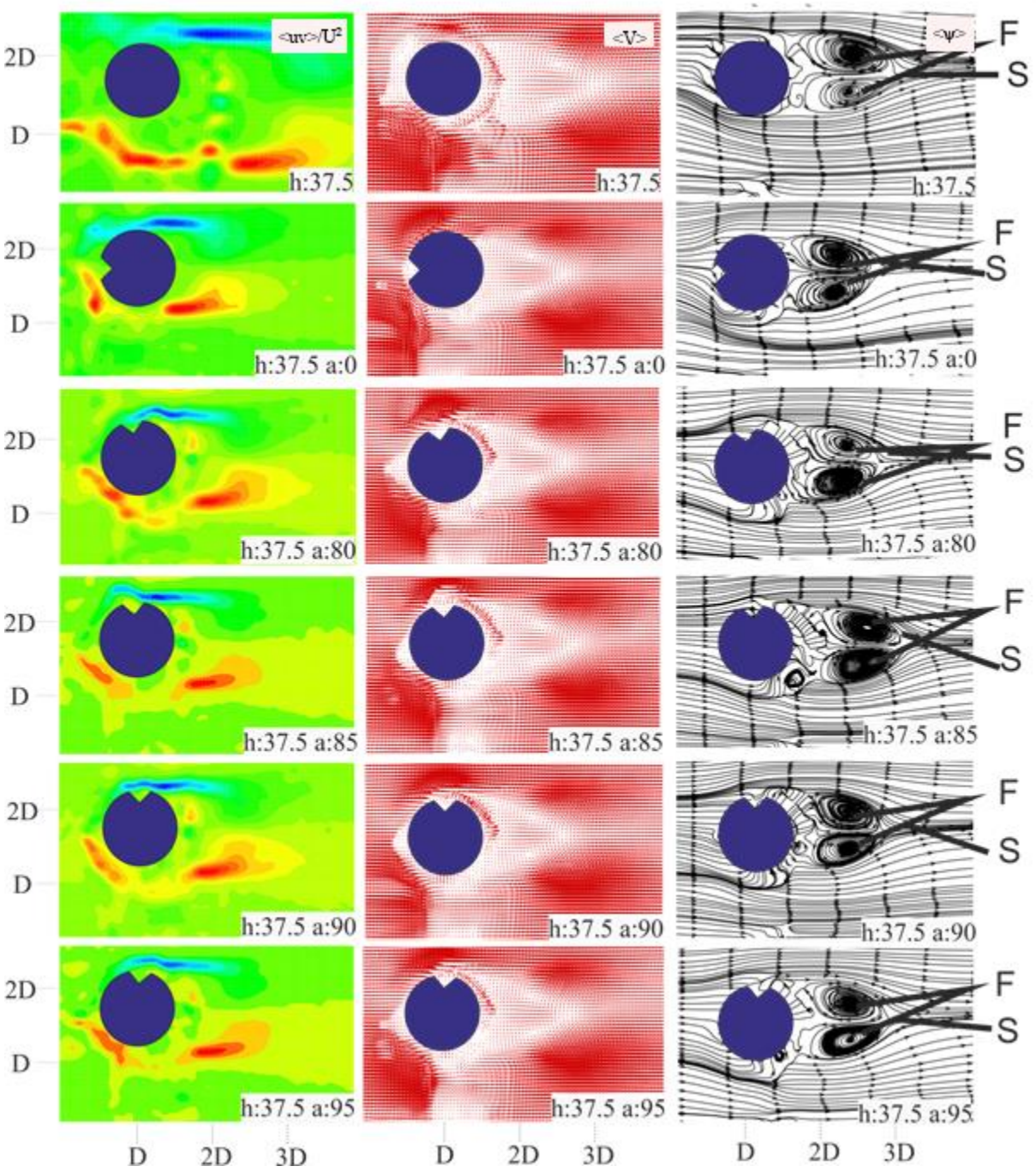

Figure. 4.33. Schematic displaying of flow structure in the downstream of the triangular grooved cylinders for h: 37.5 mm situations.

Both negative and positive counters accrue for all height and angles in Fig.4.34 showing flow structure for bare cylinder and triangular cylinder positioned in h: 45 mm. Velocities vectors are observed at the same density and the same location behind the cylinders at a: 80^o, 85^o, 90^o and 95^o. No vector condensing in the back-cylinder flow region at a: 0^o. Furthermore, in the flow region behind the cylinder, the most velocity vector is seen in the bare cylinder.

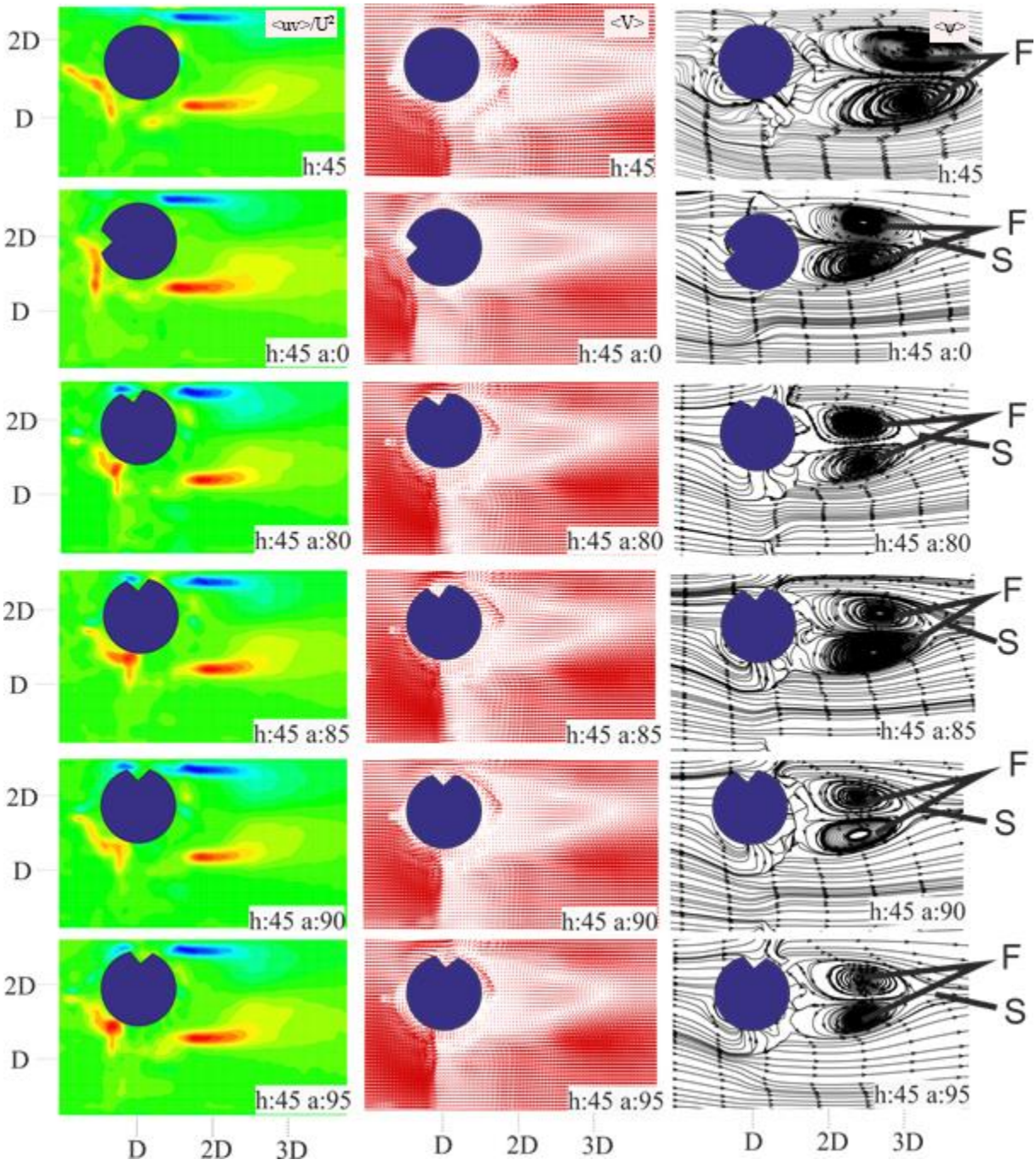

Figure. 4.34**.** Schematic displaying of flow structure in the downstream of the triangular grooved cylinders for h: 45 mm situations.

In Fig.4.35, both negative and positive counters accrue for all height and angles at h: 52.5 mm in the bare cylinder, there are no velocity vectors back of the cylinder. These vectors accrue after the a: 0^{o}. Besides, velocity vectors are observed at the back of the cylinder at a: 95^{o} intensely. The last column shows streamline vectors where two foci points are observed all angles. Also, saddle point can be accruing back of the visual.

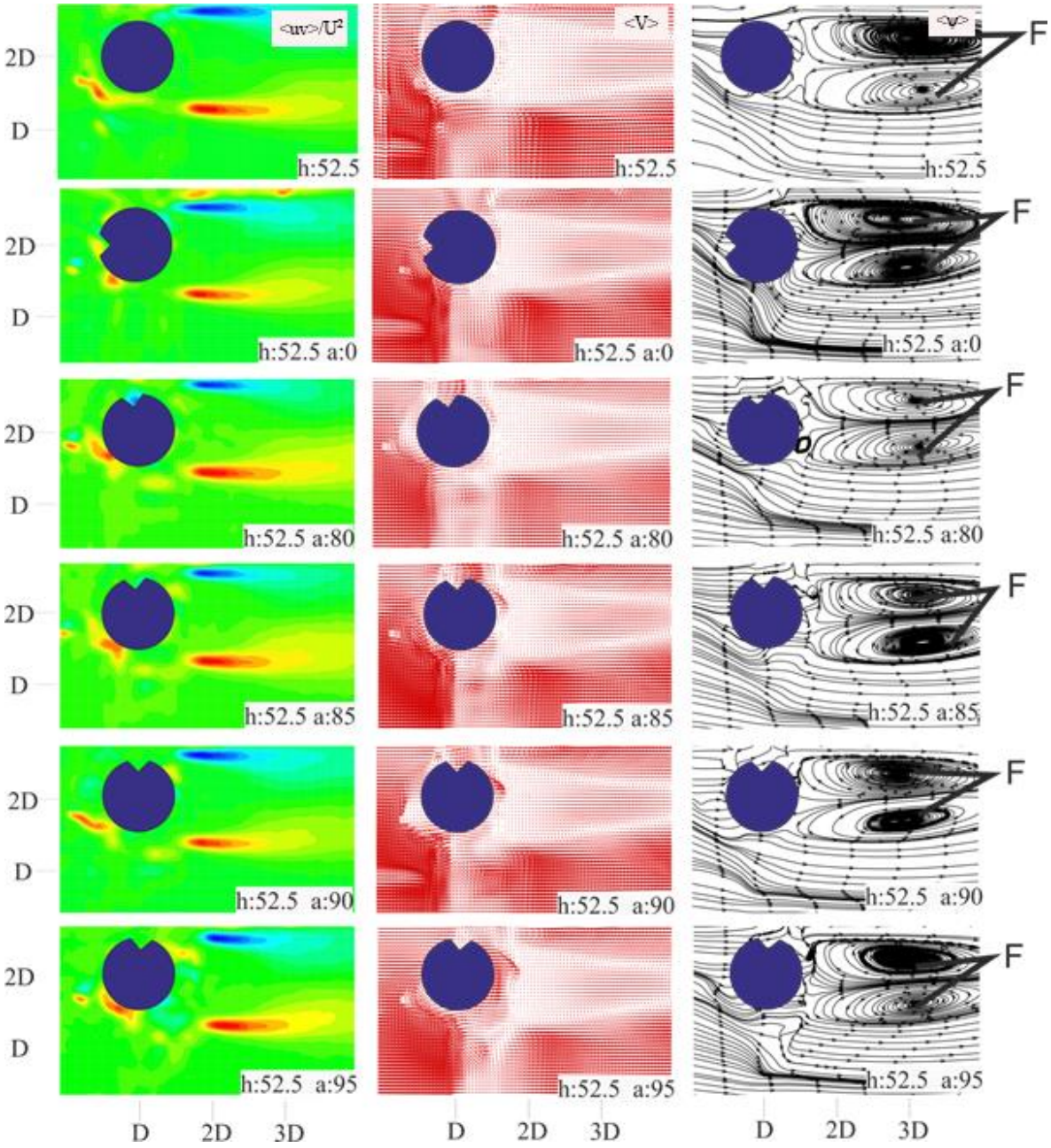

Figure. 4.35. Schematic displaying of flow structure in the downstream of the triangular grooved cylinders for h: 52.5 mm situations.

Fig. 4.36 illustrates grooved and bare cylinders with the angle from 0º to 95ºat h: 60 mm. It is observed that in this figure, at the bare cylinder in the first column positive and negative counters are seen clearly. On the other hand, there is only negative counter in grooved cylinders. Also, unlike other heights, velocity vectors are observed to concentrate on the surface of the water except for the: 0º. In the last column, it can be seen a big difference from other columns. Only one foci point is seen for h: 60 at a: 0º, 85º, 95º and bare cylinder. On the other hand, the foci points are not fully formed at a: 80º and 90º. Thus, it is observed from the

experiment that the groove in the cylinder shrinks in the transverse direction of the wake region. Moreover, the largest wake region accrues in the bare cylinder in the transverse direction.

Fig. 4.37 shows Reynolds stress (uv/U^2), time-averaged velocity vectors (<V>) and the corresponding streamline topology (<ψ>) of bare cylinder and square grooved cylinder at h: 0 mm. In the first column, only positive counter is observed due to the surface effect. Also as cylinder rotate clockwise direction, the larger pressure zone is formed. In addition, there are fragile in the positive counter and the most prominent of these is observed in the bare cylinder. Velocity vectors observe around cylinder in second column. Additionally, it is seen that in the second column, the velocity vectors are not differ greatly. When the time average streamlines are examined at the last column, one foci point are formed at a: 85^o and a: 95^o. Apart from the absence of foci point at other angles and on the bare cylinder, saddle formation is not observed in any of them due to surface effect.

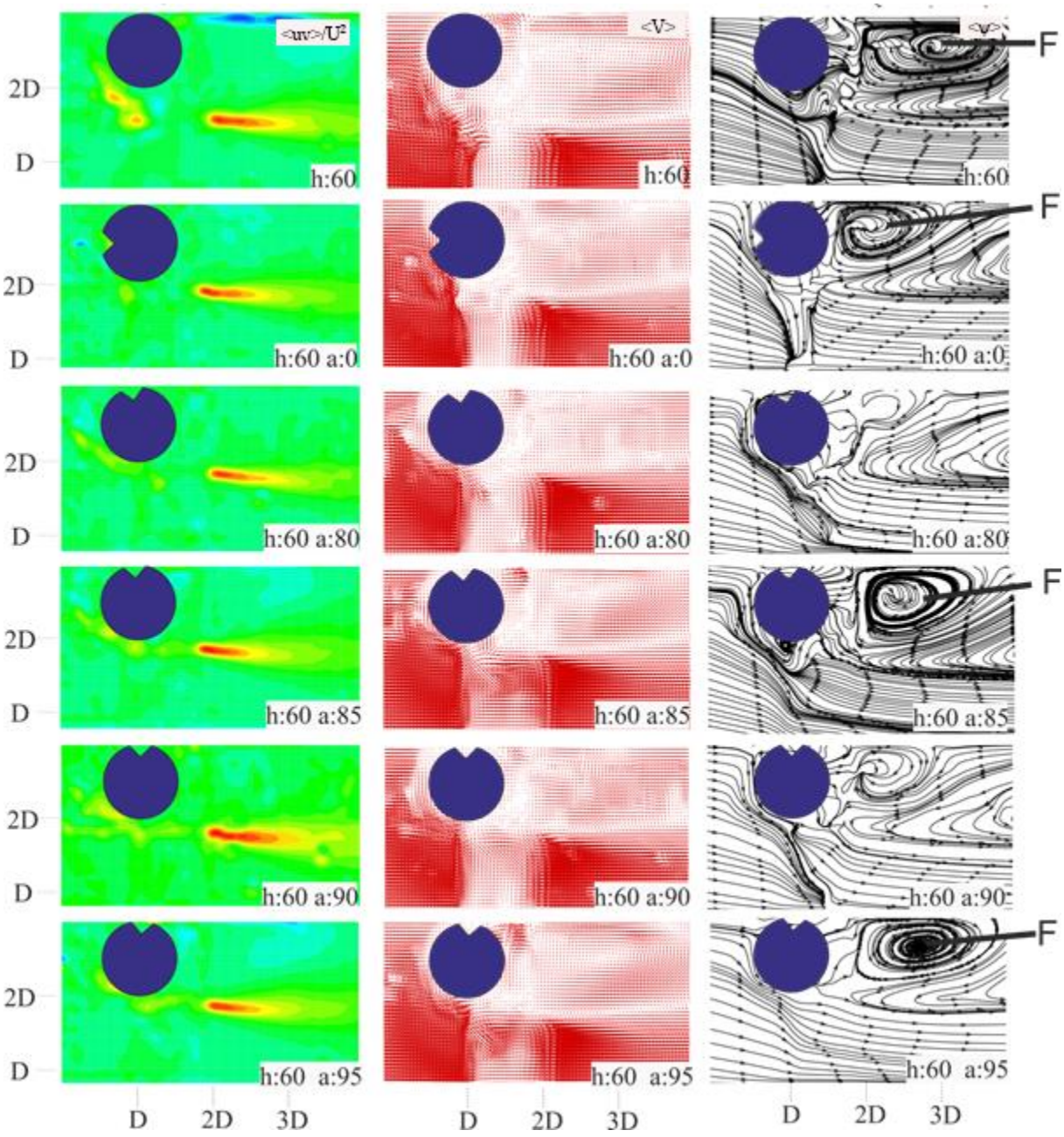

Figure. 4.36**.** Schematic displaying of flow structure in the downstream of the triangular grooved cylinders for h: 60 mm situations.

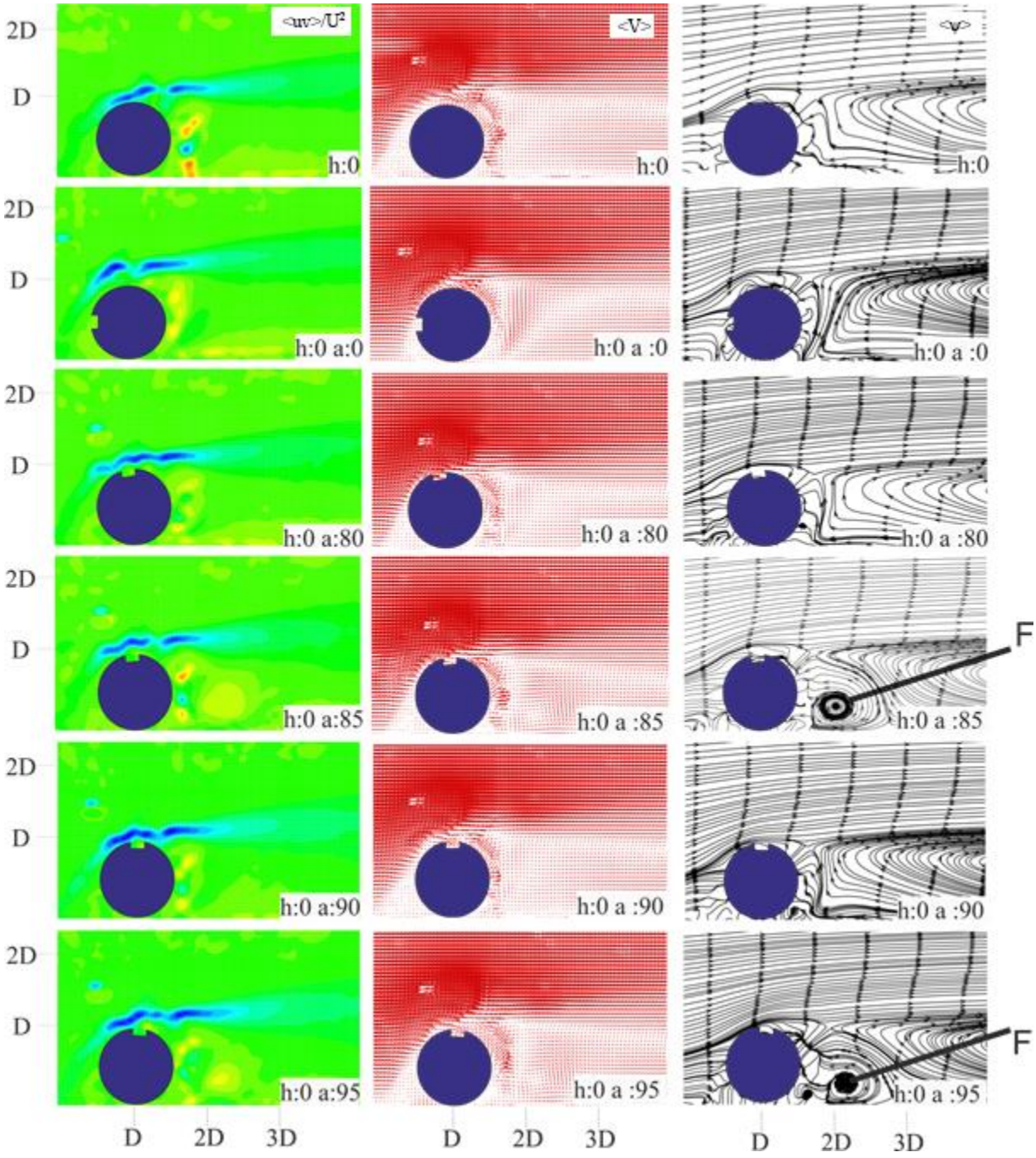

Figure. 4.37. Schematic displaying of flow structure in the downstream of the square grooved cylinder for h: 0 mm situations.

Fig. 4.38 shows Reynolds stress (uv/U^2), time-averaged velocity vectors (<V>) and the corresponding streamline topology (<ψ>) of bare cylinder and square grooved cylinder at h: 15 mm. In the first column, there is growth towards the top of the cylinder in the counter region behind the cylinder. In addition, the negative counter zone under the flat cylinder has shrunk. Velocity vectors are more joint in the grooved cylinder than in bare cylinder. In addition, in the bare cylinder, the dense velocity vectors are seen in the lower part of the

grooved cylinder in the second column. At third column, both foci point and saddle point are seen for all cylinders. Also wake regions is formed symmetrically. In addition, when compared to other cylinders of the same height at h: 15 mm, the saddle point is formed further in the cylinder at a: 0^o.

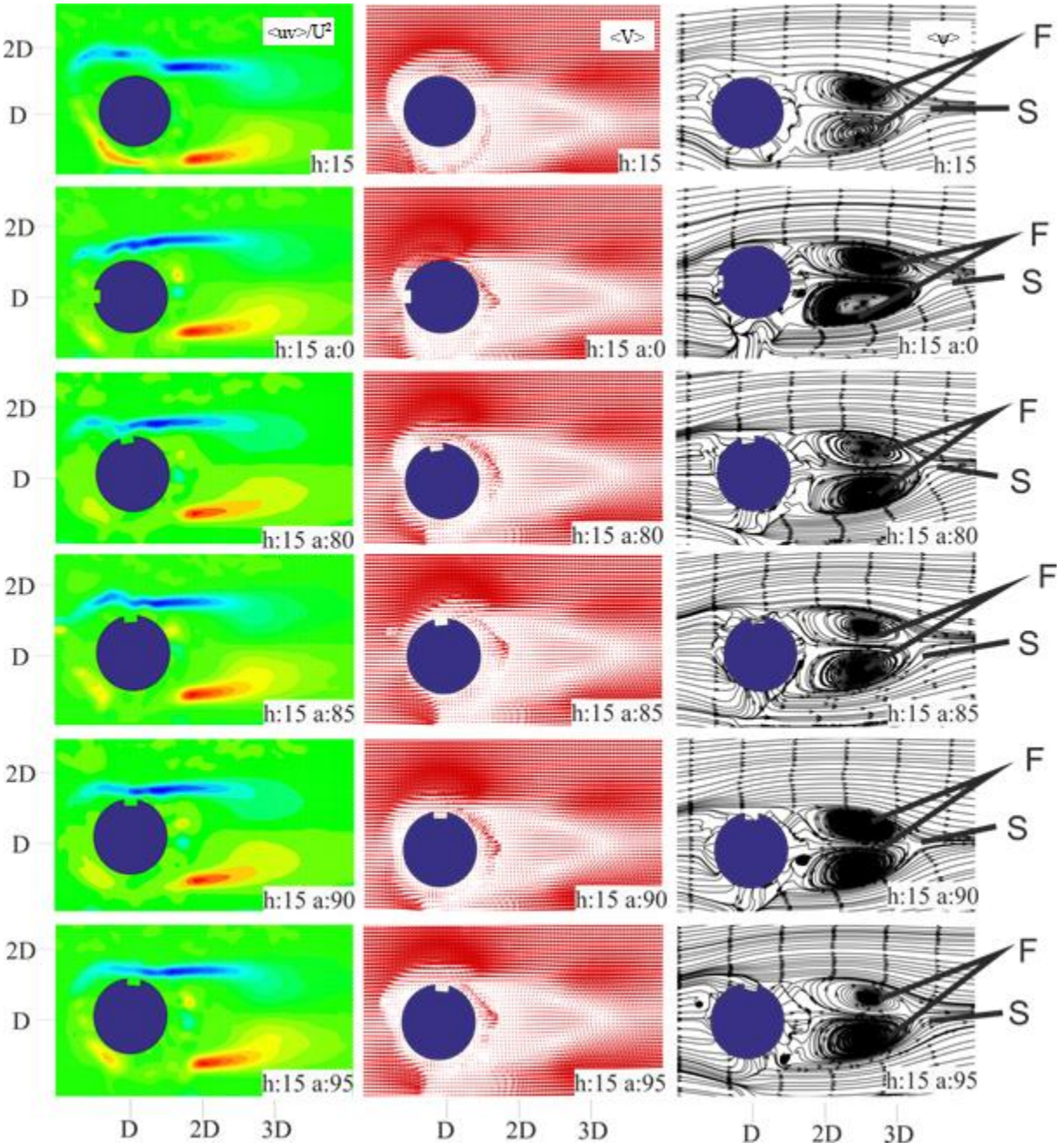

Figure. 4.38. Schematic displaying of flow structure in the downstream of the square grooved cylinder for h: 15 mm situations.

Fig. 4.39 shows Reynolds stress (uv/U^2), time-averaged velocity vectors (<V>) and the corresponding streamline topology (<ψ>) of bare cylinder and square grooved cylinder at h: 22.5 mm. Positive and negative counter form for all cylinder. Moreover, the largest positive counter form both bare cylinder and grooved cylinder at a:95^o in the transverse directions. Also, negative counter at a: 80^o form at a distance h / 2 from the cylinder. This means that, it is the closest negative counter among the other cylinders. Velocity vectors are found at the same density and at the same position behind the cylinders at a: 80^o, 85^o, 90^o and 95^o. In comparison, the bare cylinder shows the most velocity vector in the flow area behind the cylinder. Foci points and saddle points are formed at all angles and bare cylinder and it is observed that wake regions are symmetrical at third coulomb.

Fig. 4.40 shows Reynolds stress (uv/U^2), time-averaged velocity vectors (<V>) and the corresponding streamline topology (<ψ>) of bare cylinder and square grooved cylinder at h: 30 mm. As seen in the first column, the negative counter has occurred both below and behind the cylinder. In addition, the largest positive counter occurred at the angle a: 95^o. In the second column, when the average velocity vectors are compared in terms of a: 0^o, the wake flow region becomes smaller as the a: 95^o is reached. In the third column, the largest wake flow is formed at a: 0^o, while the smallest wake flow is formed at a: 90^o.

Fig. 4.41 shows Reynolds stress (uv/U^2), time-averaged velocity vectors (<V>) and the corresponding streamline topology (<ψ>) of bare cylinder and square grooved cylinder at h: 37.5 mm. Compared to the results of the previous heights, it is seen that the largest negative counter in the first column occurred at a height of h: 37.5. In addition, the largest negative counter at this height is formed in the bare cylinder, and the pressure zone shrinks as the angle a: 95 is reached. In addition to not much variation in time-averaged velocity vectors and streamlines, the largest streamline area is formed behind the bare cylinder.

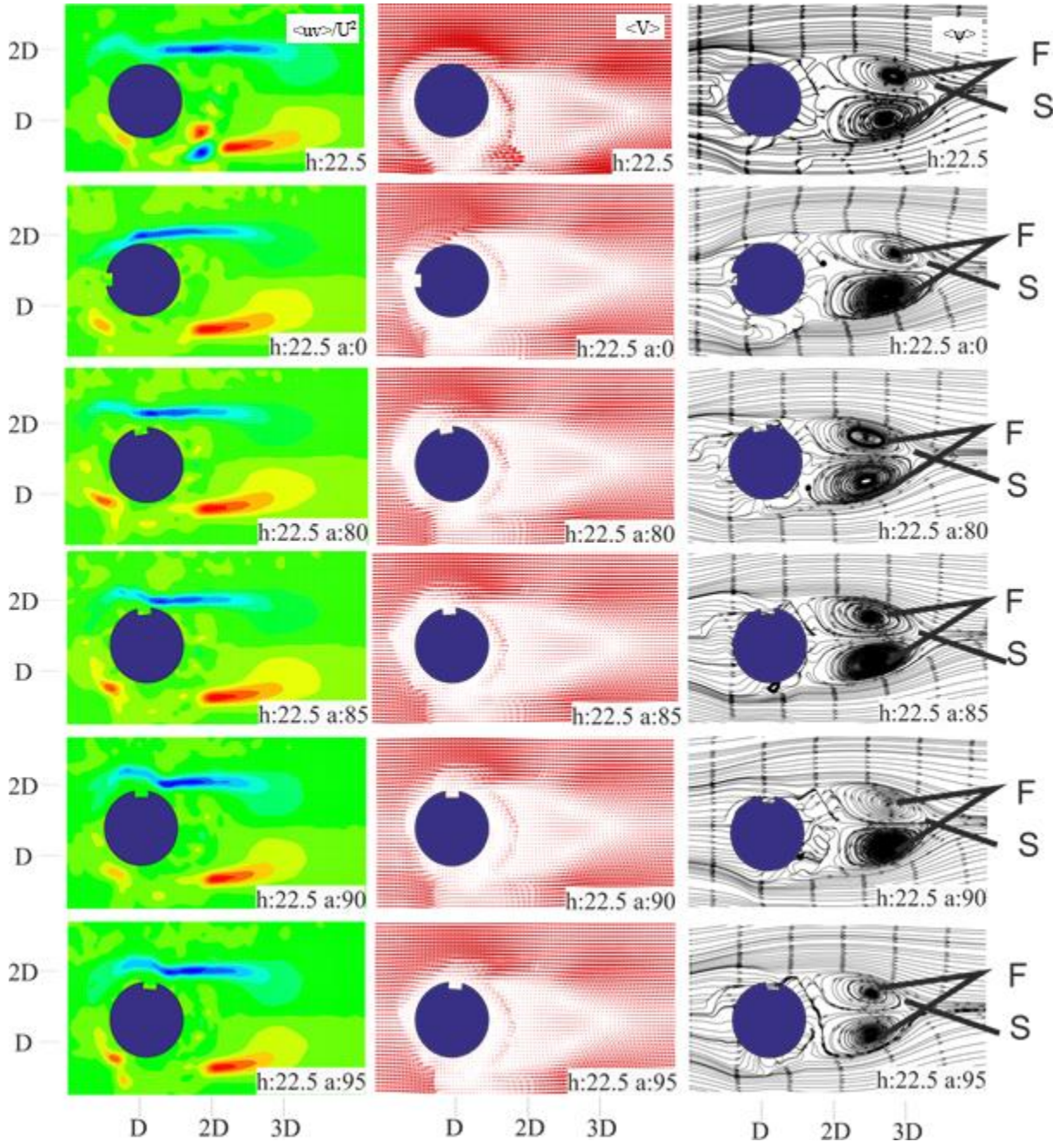

Figure. 4.39**.** Schematic displaying of flow structure in the downstream of the square grooved cylinder for h: 22.5 mm situations.

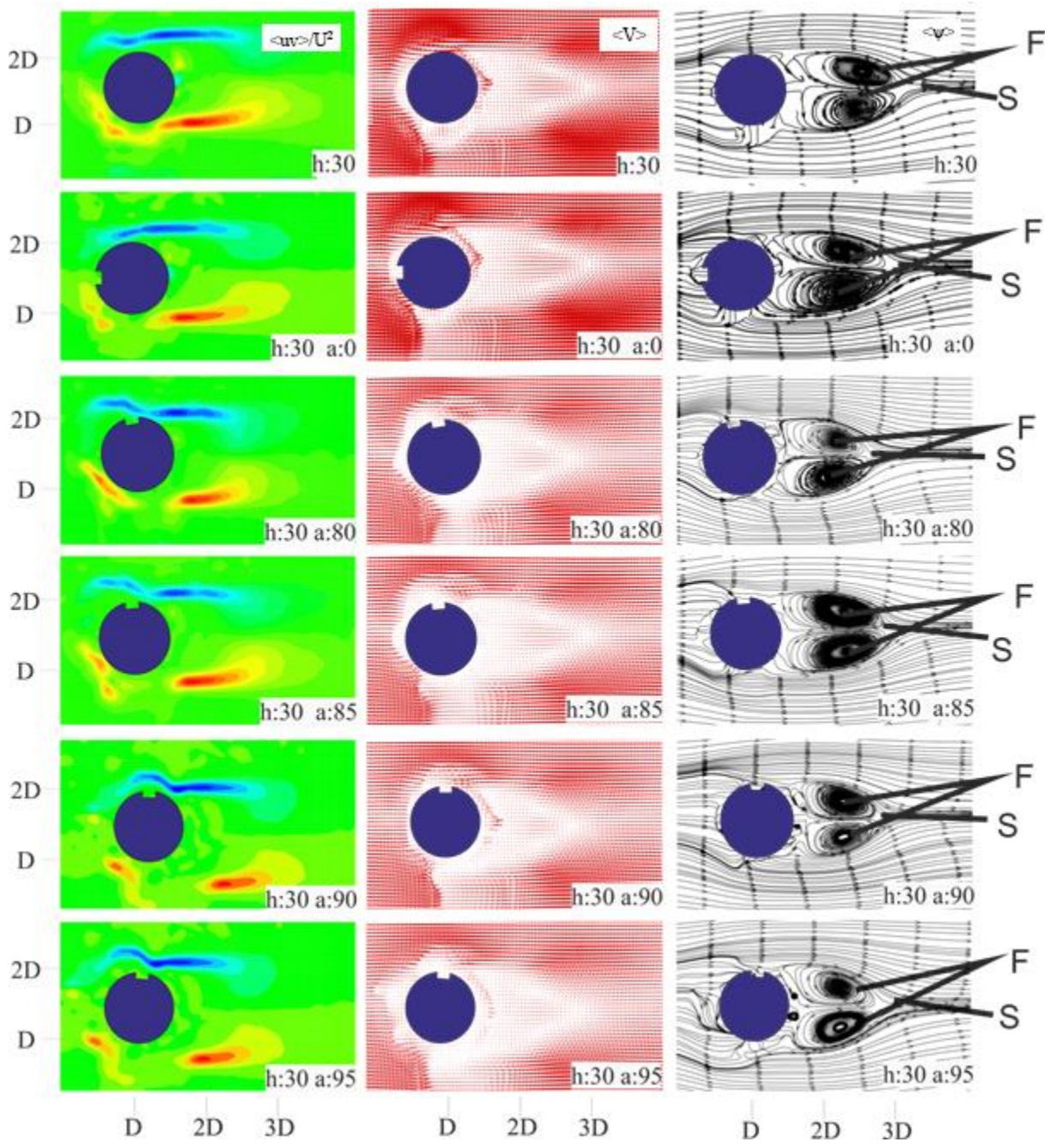

Figure. 4.40**.** Schematic displaying of flow structure in the downstream of the square grooved cylinder for h:30 mm situations.

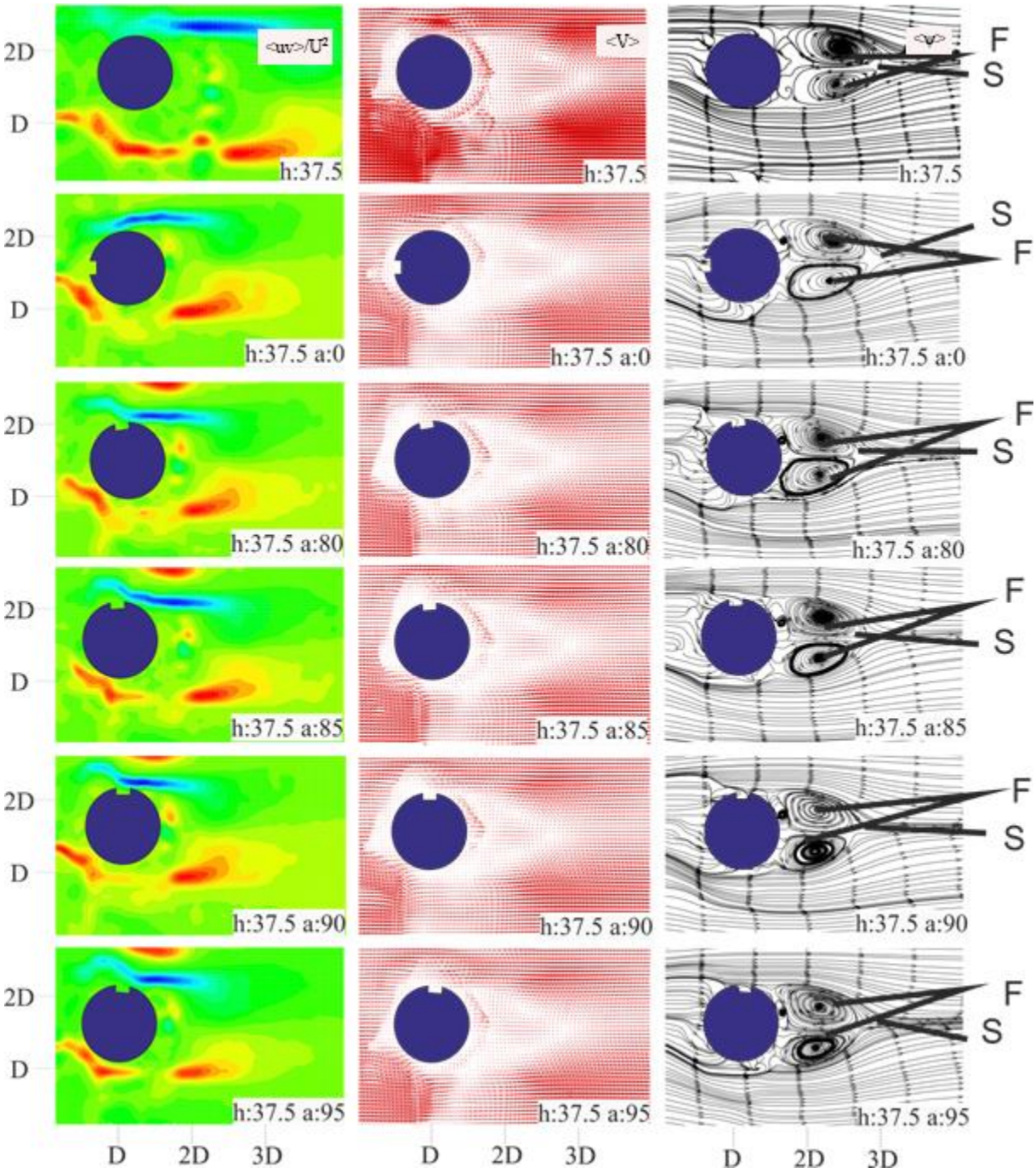

Figure. 4.41. Schematic displaying of flow structure in the downstream of the square grooved cylinder for h: 37.5 mm situations.

Fig. 4.42 shows Reynolds stress (uv/U^2), time-averaged velocity vectors (<V>) and the corresponding streamline topology (<ψ>) of bare cylinder and square grooved cylinder at h: 45 mm. In the first column, it is seen that the negative and positive counter get larger as the angle increases, unlike the cylinders at other heights. In addition, while the smallest time-averaged velocity vector field is at angles a: 85º and a: 90º; the largest area is formed at of a: 95º. In the third column, the largest wake region is seen in bare cylinder and a: 95º.

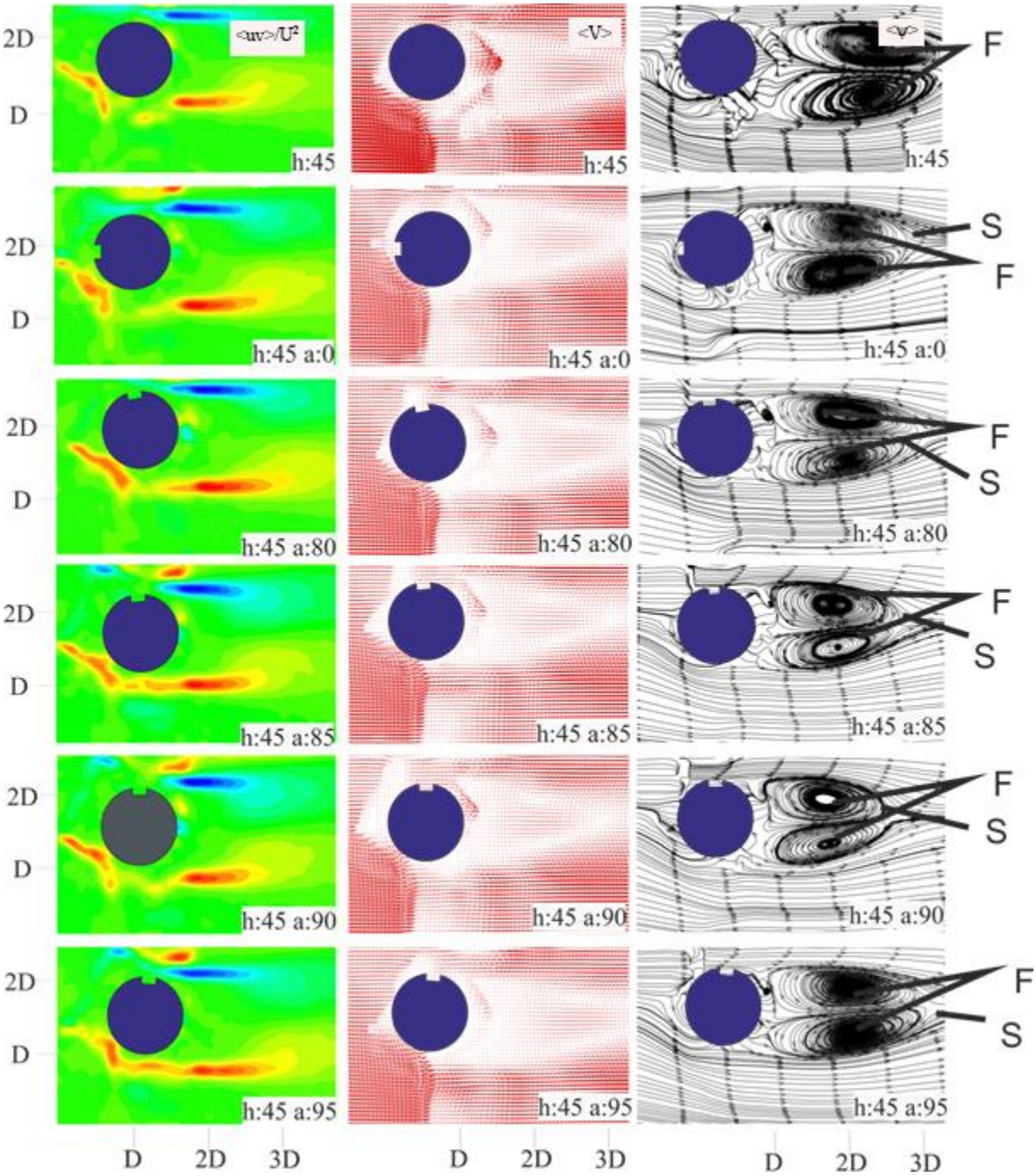

Figure. 4.42. Schematic displaying of flow structure in the downstream of the square grooved cylinder for h: 45 mm situations.

Fig. 4.43 shows Reynolds stress (uv/U^2), time-averaged velocity vectors (<V>) and the corresponding streamline topology (<ψ>) of bare cylinder and square grooved cylinder at h: 52.5 mm. When observed Reynolds Stress at first column, both negative and positive counter are observed for all cylinder. Furthermore, the largest positive counter is observed a :80^o and 90^o. However, the largest negative counter form at a:90^o. In the grooved cylinder, the velocity vector is formed at the back of the cylinder near the cylinder surface, while the density is not

seen at the same location in the bare cylinder. In the third column, while foci points are formed in all cylinders, no saddle points are formed. Further, the start of the vortex occurre at a distance of approximately h / 3 from the cylinder.

Fig. 4.44 shows Reynolds stress (uv/U^2), time-averaged velocity vectors (<V>) and the corresponding streamline topology (<ψ>) of bare cylinder and square grooved cylinder at h: 60 mm. In the first column, only negative counter is formed at angles a: 80^o and a: 90^o, while both negative and positive pressure zones are formed at other angles and in the bare cylinder. In the time-averaged velocity vectors, the largest dead flow region occurs in the bare cylinder when compared to the bare cylinder and the grooved cylinder. In addition, as the a: 0^o is approached to the a: 95^o, the dead flow zone becomes smaller. Finally, in the third column, the single foci point is formed at a: 0^o, 85^o, 95^o, and foci point formation is not observed in a: 80^o and 90^o.

Fig.4.45 shows Reynolds stress (uv/U^2), time-averaged velocity vectors (<V>) and the corresponding streamline topology (<ψ>) of bare cylinder and rectangular grooved cylinder at h: 0 mm. In the first column, when we look at the cylinders, similar to the other h: 0 cylinders, only a positive counter is formed in the bare and grooved cylinders due to the surface effect. In addition, as the angle increases, it has been observed that the counter shrinks with the effect of the cavity. When the time-averaged velocity vectors are compared, there is not much change in the wake region behind the cylinder, but the smallest wake region is at the a: 85^o. Also, velocity vectors are densely observed around the bare cylinder and at a: 0^o. As the angle increased, the density decreased. The corresponding streamline topology in the third column, only one focal point is formed at a: 90^o and a: 95^o.

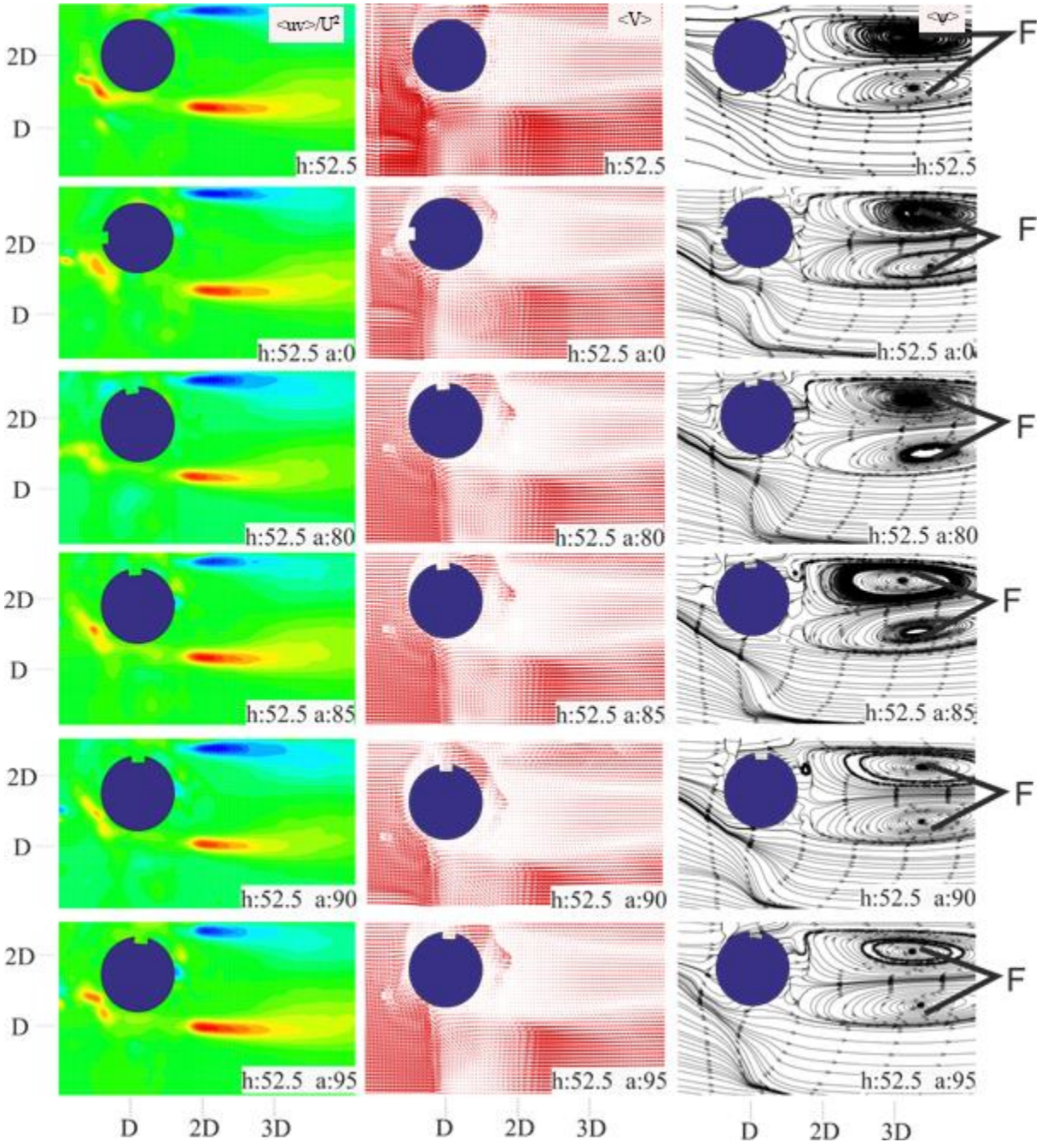

Figure. 4.43. Schematic displaying of flow structure in the downstream of the square grooved cylinder for h: 52.5 mm situations.

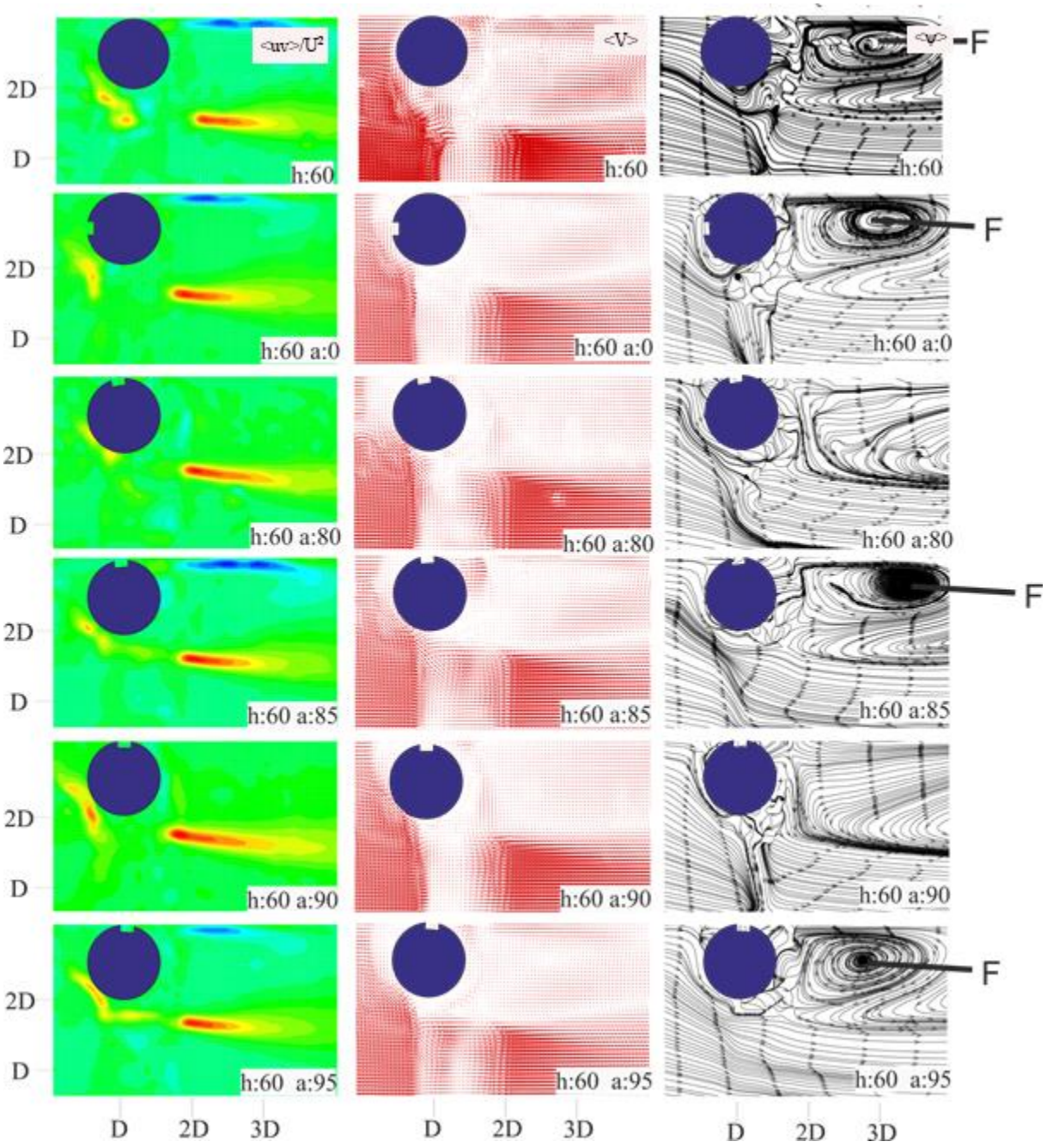

Figure. 4.44. Schematic displaying of flow structure in the downstream of the square grooved cylinder for h: 60 mm situations.

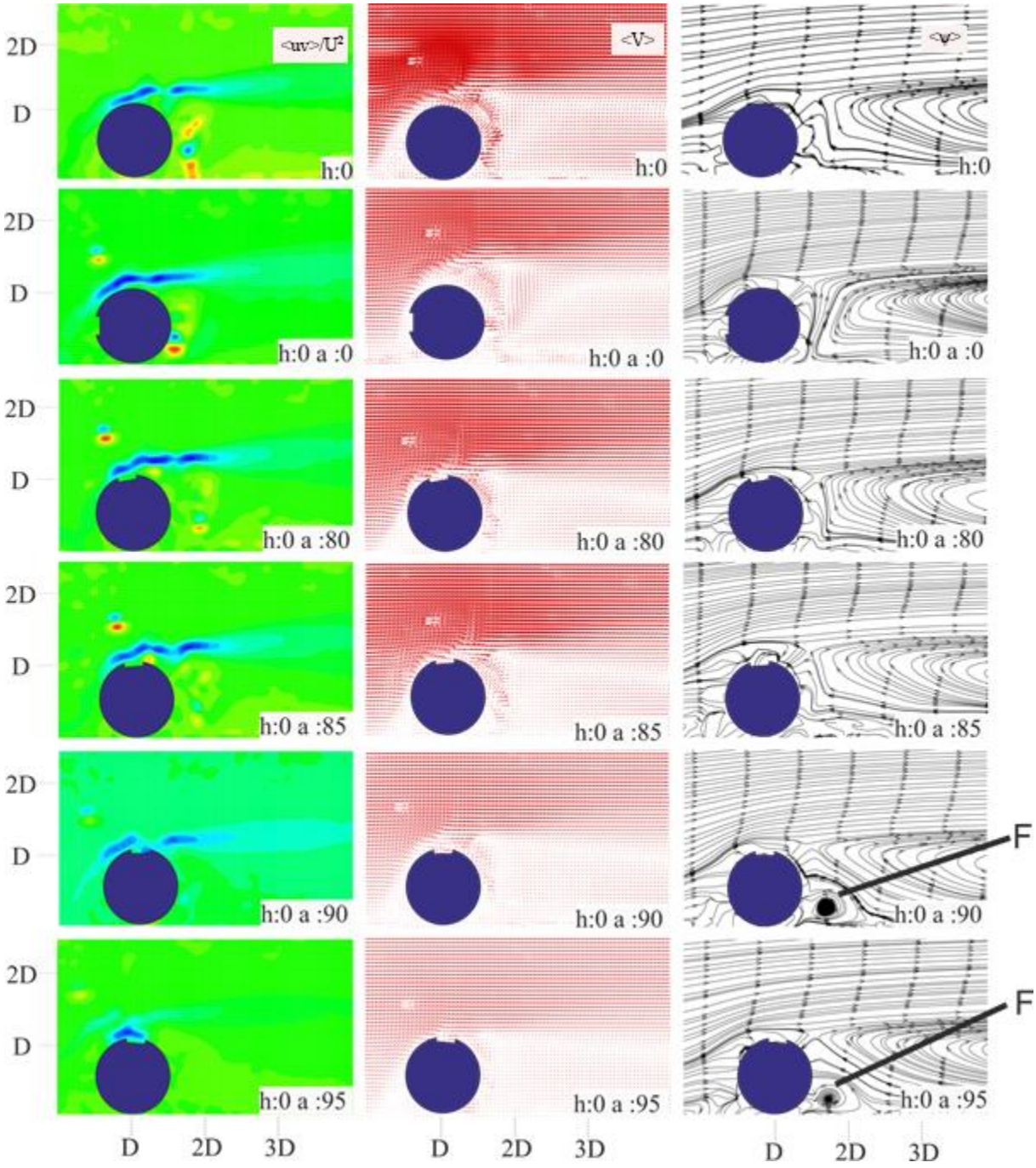

Figure. 4.45**.** Schematic displaying of flow structure in the downstream of the rectangular grooved cylinder for h: 0 mm situations.

Fig. 4.46 shows Reynolds stress (uv/U^2), time-averaged velocity vectors (<V>) and the corresponding streamline topology (<ψ>) of bare cylinder and rectangular grooved cylinder at h: 15 mm. In the first column, although there is not much change in the positive counter, as angle increases, there is a decrease in the negative counter. In the second column, while velocity vectors are formed in the bare cylinder just below the cylinder, it is observed in the upper part of the grooved cylinder. Although the wake region areas are similar in the whole

cylinder, it is observed that the velocity vectors are more intense in the bare cylinder. The third column shows the two foci and saddle point both bare and grooved cylinders. In addition, the largest swirl area is formed in the flat cylinder, and this area is reduced in the bare cylinders.

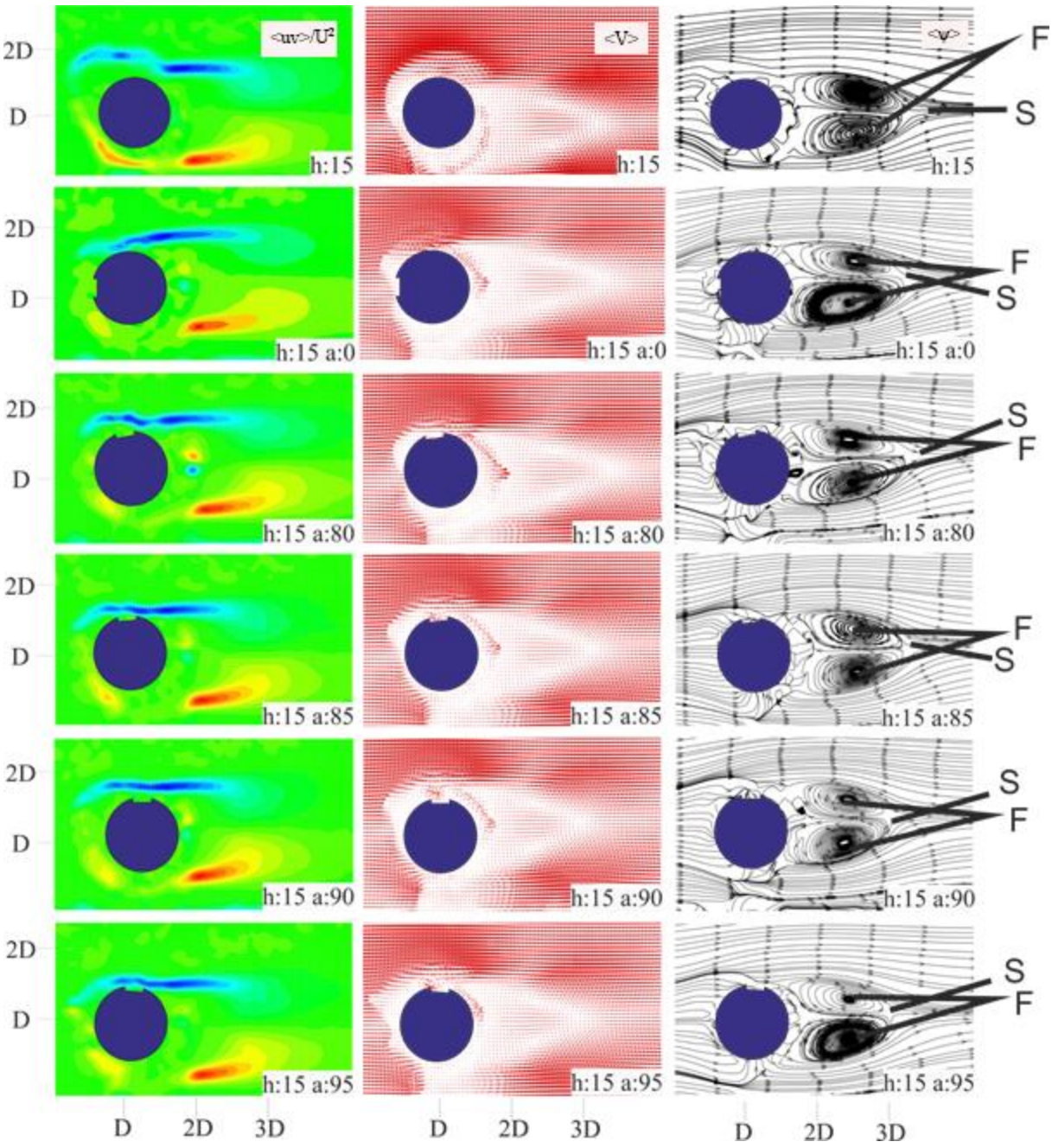

Figure. 4.46. Schematic displaying of flow structure in the downstream of the rectangular grooved cylinder for h: 15 mm situations.

Fig. 4.47 shows Reynolds stress (uv/U^2), time-averaged velocity vectors (<V>) and the corresponding streamline topology (<ψ>) of bare cylinder and rectangular grooved cylinder at h: 22.5 mm. When the time-averaged velocity vectors at h: 22.5 are examined, unlike the other results, a positive counter has occurred in the lower part of the cylinder in the bare cylinder as in the upper part. It is seen that at second column, the most concentrated velocity vectors are seen in the bare cylinder. In addition, the densist of velocity vectors is observed at a: 0^o. In addition, as the groove angle increases, the wake region shrinks.

Fig. 4.48 shows Reynolds stress (uv/U^2), time-averaged velocity vectors (<V>) and the corresponding streamline topology (<ψ>) of bare cylinder and rectangular grooved cylinder at h: 30 mm. As seen in the first column, the smallest negative counter is formed at a: 85^o, and there is a reduction in the pressure zone in the grooved cylinder compared to the bare cylinder. In the second column, when the time average velocity vectors are examined, the smallest wake region is seen at a: 90^o. It is also observed that the streamlines are symmetrical as seen in the third column. Two foci point and saddle point are observed in all the grooved and bare cylinder. Also, the wake region area starts to decrease after a: 80^o.

Fig. 4.49 shows Reynolds stress (uv/U^2), time-averaged velocity vectors (<V>) and the corresponding streamline topology (<ψ>) of bare cylinder and rectangular grooved cylinder at h: 37.5 mm. For the bare cylinder, it has been observed that, the negative counter is very large compared to other heights and shrinks in the grooved cylinder. Similarly, shrinkage occurs in time-averaged velocity vectors and the corresponding streamline topology. At this height, two foci points and saddle point are formed. On the other hand, compared to the cylinders of the whole, the smallest vortex area is at the same height a: 90^o and $95^{o,}$ when two foci point form.

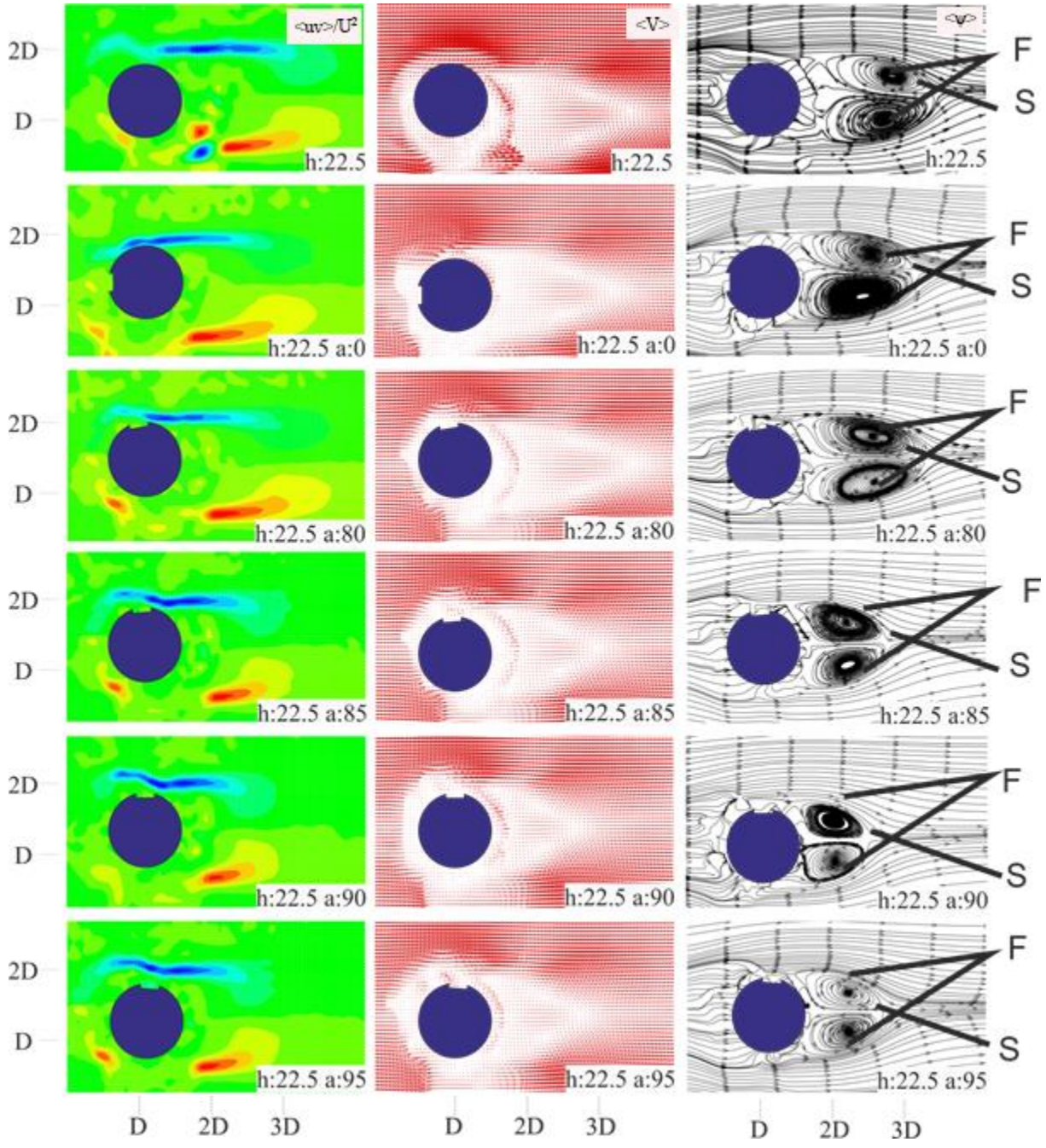

Figure. 4.47. Schematic displaying of flow structure in the downstream of the rectangular grooved cylinder for h: 22.5 mm situations.

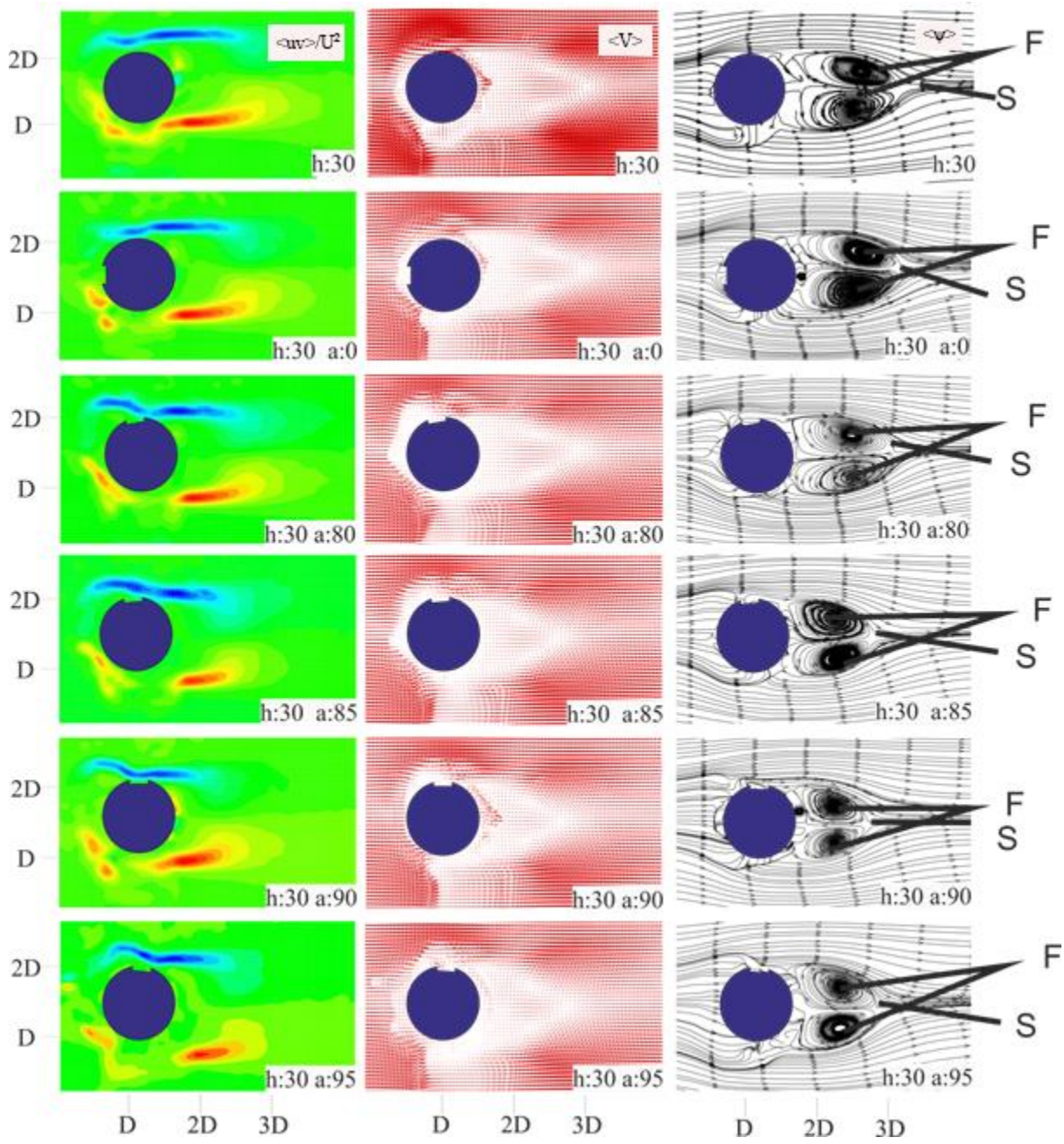

Figure. 4.48**.** Schematic displaying of flow structure in the downstream of the rectangular grooved cylinder for h: 30 mm situations.

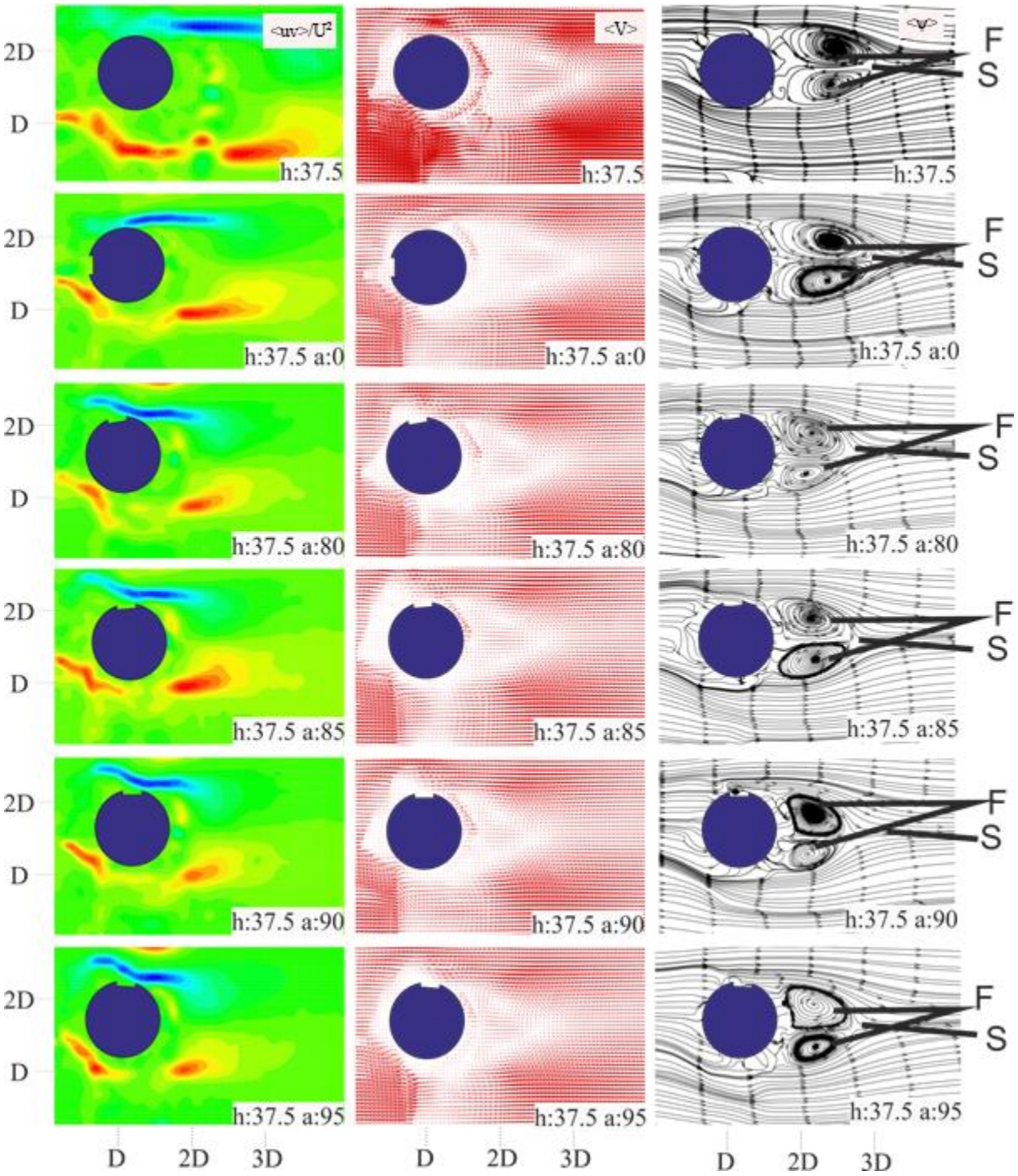

Figure. 4.49. Schematic displaying of flow structure in the downstream of the rectangular grooved cylinder for h: 37.5 mm situations.

Fig. 4.50 shows Reynolds stress (uv/U^2), time-averaged velocity vectors (<V>) and the corresponding streamline topology (<ψ>) of bare cylinder and rectangular grooved cylinder at h: 45 mm. In the first column, the largest negative pressure zone is formed at a: 85^o and a: 90^o. In addition, there is no regular shrinkage in the negative and positive counter. A negative counter has occurred in the upper part of the cylinder in the grooved cylinder as in the bottom

part. When examined time-averaged velocity vectors, the most velocity vector is seen in the bare cylinder and the wake region decreases as the angle increases. In addition to this, no big change is observed in the wake region area of a: 85^o, 90^o and 95^o. When the corresponding streamline topology are examined, the saddle point formation is not seen in bare and a: 0^o, but it is seen in other grooved cylinders. This is because the vortex area shrinks.

Fig. 4.51 shows Reynolds stress (uv/U^2), time-averaged velocity vectors (<V>) and the corresponding streamline topology (<ψ>) of bare cylinder and rectangular grooved cylinder at h: 52.5 mm. At the first column, positive and negative counters form at h distance from the cylinder is seen for all cylinder. Also, in all cylinders the negative counter is formed from the front of the cylinder and rupture occurs and is seen again at the rear. In the second column, there is not much change in the velocity vector wake region areas and the most intense velocity vector is observed in the bare cylinder. When the last column is examined, the foci point is observed in all cylinders, but the saddle point is not seen in the drafting area because the vortex area is enlarged in the direction of the transverse direction.

Fig. 4.52 shows Reynolds stress (uv/U^2), time-averaged velocity vectors (<V>) and the corresponding streamline topology (<ψ>) of bare cylinder and rectangular grooved cylinder at h: 60 mm. Despite the surface effect of h: 60 height, positive pressure counter is formed in the bare cylinder at other angles except a: 0^o and a: 95^o, and the smallest positive counter is at the a: 80. In addition, the largest negative counter is formed at a: 95^o. In addition, when the time-averaged velocity vectors are examined, very large changes are not observed. In the third column, the largest focal point is formed in the bare cylinder but the focal point is not formed at a: 95^o.

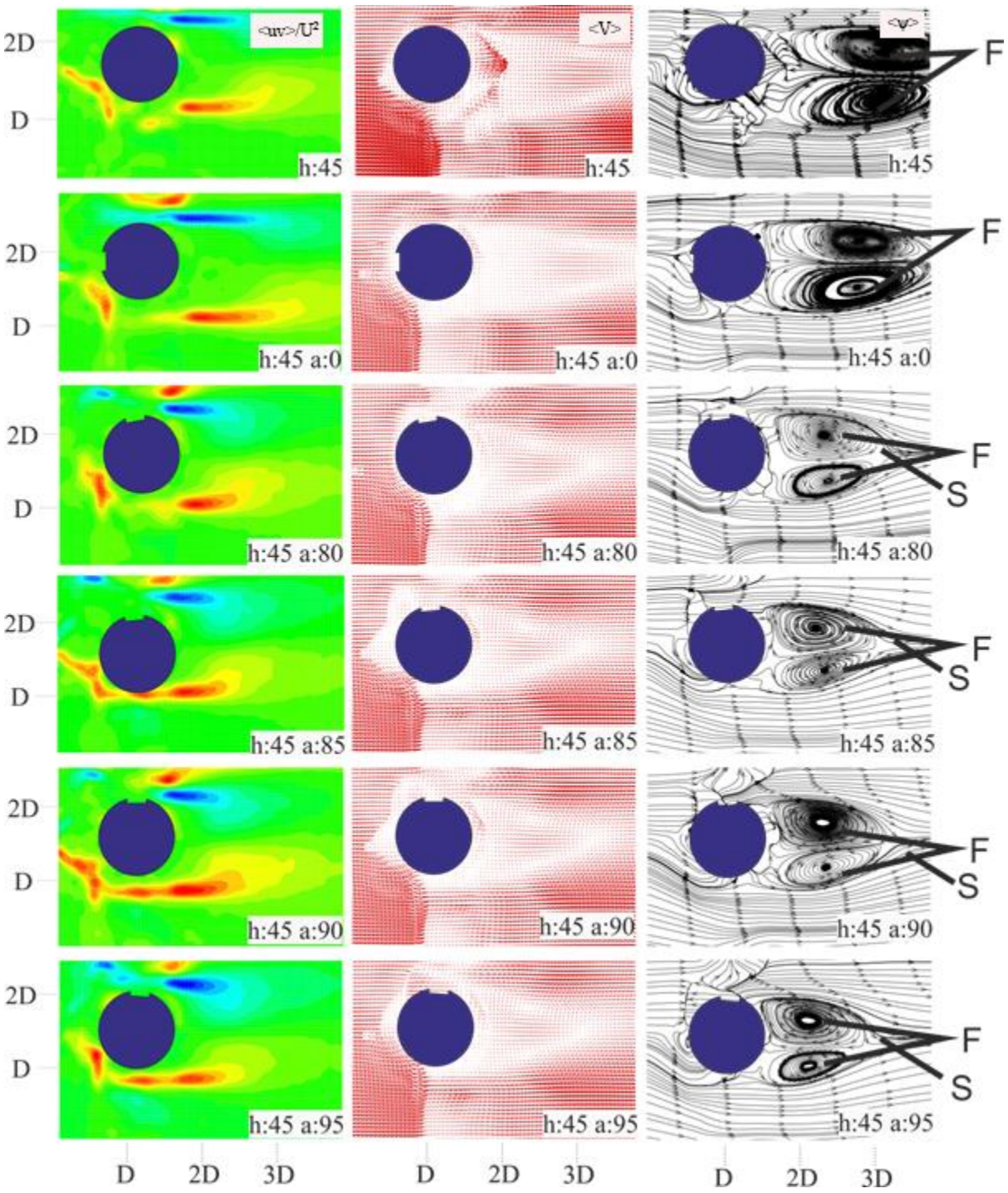

Figure. 4.50**.** Schematic displaying of flow structure in the downstream of the rectangular grooved cylinder for h: 45 mm situations.

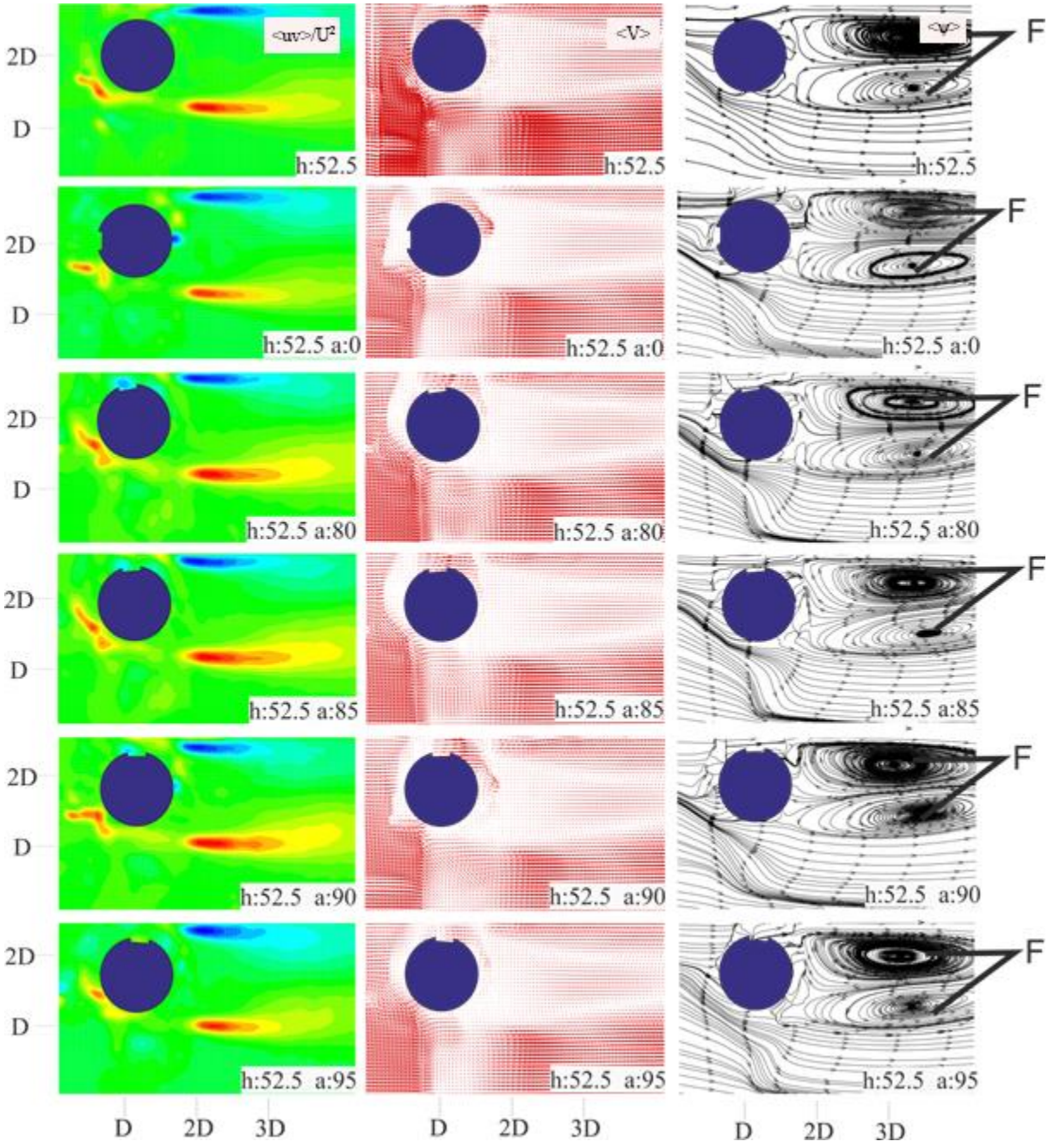

Figure. 4.51. Schematic displaying of flow structure in the downstream of the rectangular grooved cylinder for h: 52.5 mm situations.

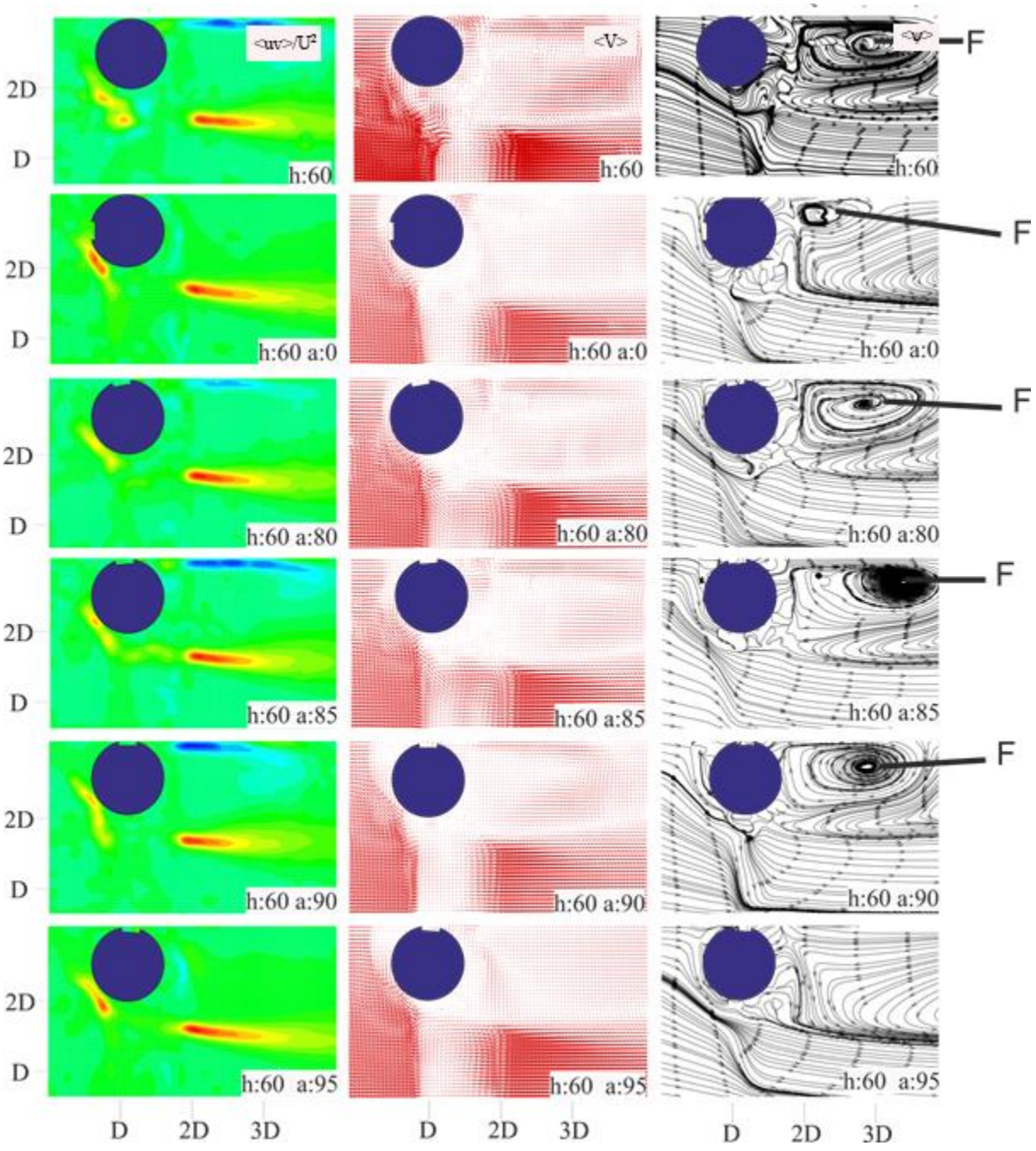

Figure. 4.52**.** Schematic displaying of flow structure in the downstream of the rectangular grooved cylinder for h: 60 mm situations.

4.3. CD Results

In this section, drag coefficients, calculated with the help of velocity values obtained from particle image velocimetry technique, are represented in detail. CD values are calculated numerically about 2D away from the cylinder in order to obtain optimum results which are consistent with the study of Son and Cetiner (2015). As can be seen in literature, it is observed that the drag coefficient value in the smooth body is lower than the rough surface at high Reynolds number like the study of Choi et al. (2008). In addition, in this study, it is observed that drag values are lower in the bare cylinder than grooved cylinder. Also, as Reynolds number increases, CD values decrease from h: 0 mm to 30 mm at bare cylinder with the accordance literature (Wen et al., 2004). On the other hand, CD values increase between h:30 mm and h :37.5 mm and then it decreases. The lowest CD occurred with the value of 0,74 at h: 52.5mm as can be seen from Table 4. On the other hand, the highest CD occurred with a value of 1,059 at h: 37.5 mm. It is also noted that the results obtained are closely related. Drag coefficient values of cylinders for grooved cylinders for all heights are represented in Table 4.2-4.8. According to these findings, as seen in table 4.2, the highest drag coefficient value in h: 0 mm has been obtained at a: 90 for triangular grooved, at a: 85 for square grooved and at a: 85 for rectangular grooved. Looking at Table 4.3, in h: 15 mm, the highest drag coefficient has been obtained at a: 90 for triangular grooved, at a: 85 for square grooved and at a: 95 for rectangular grooved. According to Table 4.4, in h: 22.5 mm, the highest drag coefficient value has been obtained at a: 95 for triangle grooved, at a: 0 for square grooved and at a: 80 for rectangular grooved. As seen in Table 4.5, the highest drag coefficient in h: 30 mm has been found at a: 95 groove angle in three groove options. Looking at Table 4.6, the highest drag coefficient at h: 37.5 mm has been found at a: 0 for triangular and rectangular grooved, and at a: 80 for square grooved. For the height of h: 45 mm, as seen in Table 4.7, the highest drag coefficient has been obtained at an angle of a: 90 for triangle grooved, at a: 95 for square grooved and at a: 85 for rectangular grooved. Finally, looking at Table 4.8, the highest drag coefficient value in h: 52.5 mm has been found at a: 0 for triangular grooved, at a: 80 for square grooved and at a: 85 for rectangular grooved.

Table 4.1**.** Drag coefficient values for bare cylinder at different heights

CD	**Bare**
h:0	0,963237
h:15	0,836642
h:22.5	0,743685
h:30	0,859211
h:37.5	1,059731
h:45	0,999986
h:52.5	0,742597

Table 4.2**.** Drag coefficient values of grooved cylinders with height h: 0 mm according to the groove angles

CD	**h:0**		
	Triangular	**Square**	**Rectangular**
a:0	0,984824	0,785060	0,947992
a:80	1,294557	0,905350	1,078010
a:85	1,209769	1,004266	1,133542
a:90	1,424430	0,925344	0,999782
a:95	1,232564	0,943197	1,013806

Table 4.3**.** Drag coefficient values of grooved cylinders with height h: 15 mm according to the groove angles

CD	**h:15**		
	Triangular	**Square**	**Rectangular**
a:0	0,910757	1,348236	1,365009
a:80	0,96029	1,320947	1,341068
a:85	0,982293	1,407048	1,351757
a:90	1,007494	1,365651	1,251876
a:95	0,970365	1,388424	1,391301

Table 4.4**.** Drag coefficient values of grooved cylinders with height h: 22.5 mm according to the groove angles

CD	**h:22.5**		
	Triangular	**Square**	**Rectangular**
a:0	0,84404	1,182549	1,183458
a:80	0,899416	1,129945	1,249685
a:85	0,924493	1,171046	1,207078
a:90	0,892728	1,088654	1,208266
a:95	0,981509	1,168686	1,224631

Table 4.5**.** Drag coefficient values of grooved cylinders with height h: 30 mm according to the groove angles

CD	**h:30**		
	Triangular	**Square**	**Rectangular**
a:0	0,951978	1,114307	1,113530
a:80	0,945689	1,037609	1,115548
a:85	0,944947	1,103765	1,004387
a:90	0,917963	1,052083	1,032250
a:95	1,121036	1,351186	1,443778

Table 4.6**.** Drag coefficient values of grooved cylinders with height h: 37.5 mm according to the groove angles

CD	**h:37.5**		
	Triangular	**Square**	**Rectangular**
a:0	0,952261	1,293552	1,418335
a:80	0,828275	1,295733	1,367526
a:85	0,903379	1,269590	1,337561
a:90	0,856416	1,288209	1,330127
a:95	0,930032	1,255965	1,386038

Table 4.7**.** Drag coefficient values of grooved cylinders with height h: 45 mm according to the groove angles

CD	**h:45**		
	Triangular	**Square**	**Rectangular**
a:0	1,172564	1,100254	1,119485
a:80	1,112494	1,147797	1,107633
a:85	1,112252	1,123854	1,122555
a:90	1,180275	1,134916	1,118941
a:95	1,146602	1,162731	1,073562

Table 4.8**.** Drag coefficient values of grooved cylinders with height h: 52.5 mm according to the groove angles

CD	**h:52.5**		
	Triangular	**Square**	**Rectangular**
a:0	1,348507	1,321908	1,394997
a:80	1,295370	1,413646	1,331614
a:85	1,208007	1,338977	1,401407
a:90	1,323616	1,341085	1,378666
a:95	1,296157	1,374670	1,399698

4.4. Strouhal Number (St) Results

The values of St for bare and triangular grooved cylinder for all heights and angles can be seen in Tables 4.9-4.12 and Figures 53-64. Strouhal number is calculated obtained with frequancy value from PIV result. For bare cylinder in Fig. 53 and Table 4.9, the highest St value occurs in h: 15 mm as 0,09. According Table 4.10, because of the surface effect in h: 60 mm, the highest St value is seen at a: 95^{o} as 0,58 for triangular grooved cylinder. Compatible with triangular cylinder the highest St value is seen at a: 95^{o} in h:60 mm as 0,64 due to surface effect for rectangular grooved cylinder. Furthuremore, the highest St value is seen at a: 0^{o} in h:22.5 as 0,30 mm for square grooved cylinder. When all cylinders are compared, the minimum value of the St is observed as 0.004 in h:0 mm at a :80^{o} for square grooved cylinder.

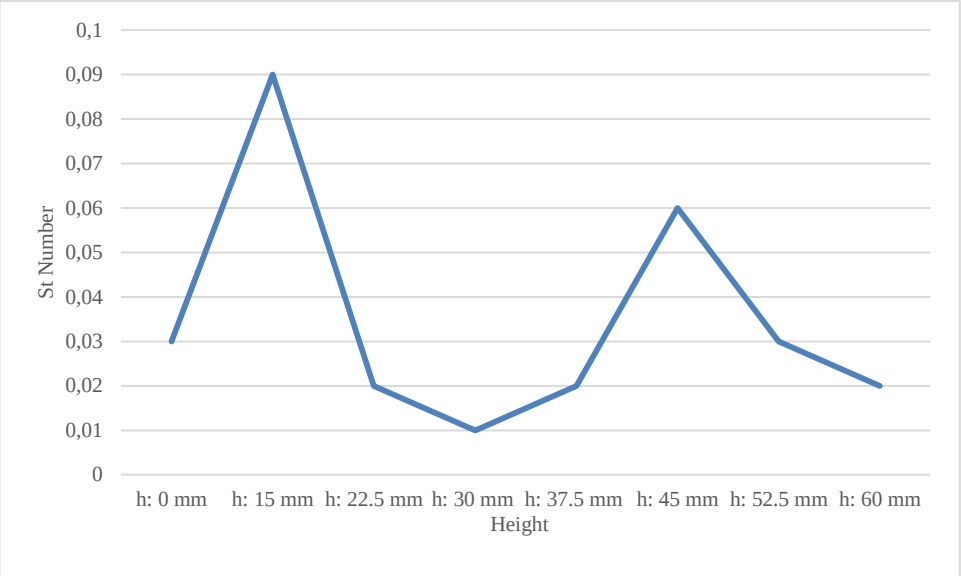

Figure. 4.53**.** Distribution of St number values per heights for bare cylinder

Table 4.9**.** St values for bare cylinder

St	Bare Cylinder
h: 0 mm	0,03
h: 15 mm	0,09
h: 22.5 mm	0,02
h: 30 mm	0,01
h: 37.5 mm	0,02
h: 45 mm	0,06
h: 52.5 mm	0,03
h: 60 mm	0,02

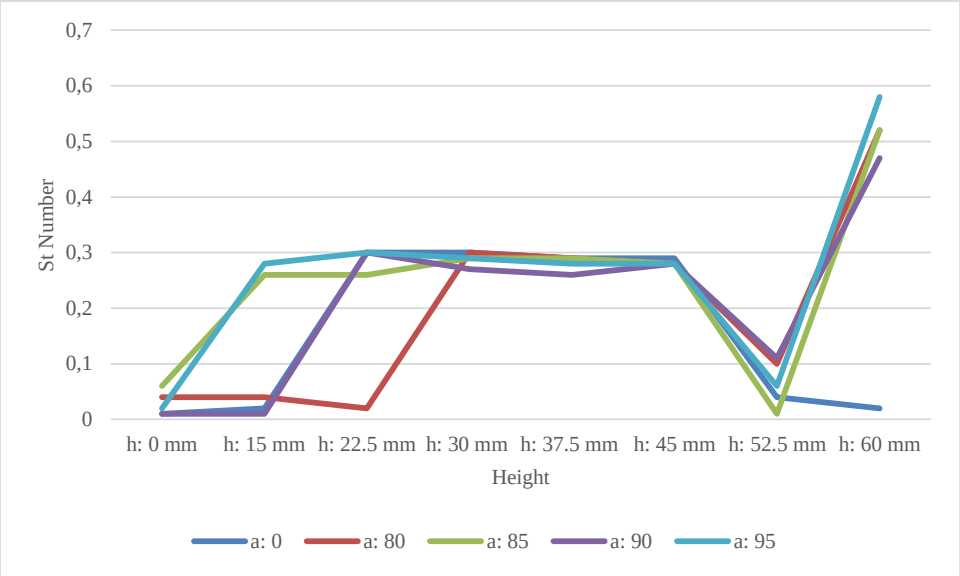

Figure. 4.54. Distribution of St number values per heights from a:0º to a: 95º for triangular cylinder.

Table 4.10. St values per height for triangular grooved cylinder

St	a: 0º	a: 80º	a: 85º	a: 90º	a: 95º
h: 0 mm	0,01	0,04	0,06	0,01	0,02
h: 15 mm	0,02	0,04	0,26	0,01	0,28
h: 22.5 mm	0,30	0,02	0,26	0,30	0,30
h: 30 mm	0,30	0,30	0,29	0,27	0,29
h: 37.5 mm	0,29	0,29	0,29	0,26	0,28
h: 45 mm	0,29	0,28	0,28	0,28	0,28
h: 52.5 mm	0,04	0,10	0,01	0,11	0,06
h: 60 mm	0,02	0,52	0,52	0,47	0,58

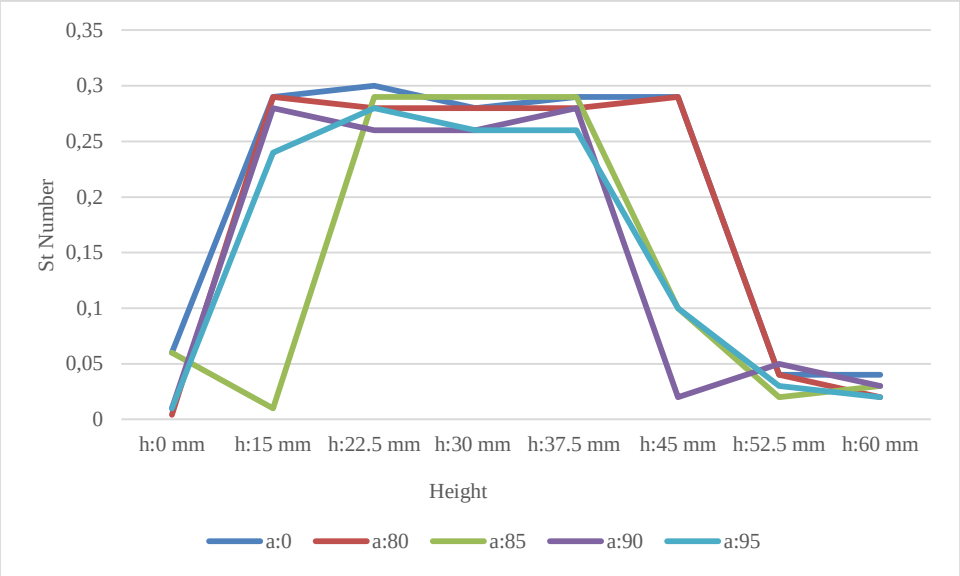

Figure. 4.55. Distribution of St number values per heights from a:0º to a: 95º for square grooved cylinder.

Table 4.11. St values per height for square grooved cylinder

St (w/d:1)	a:0º	a:80º	a:85º	a:90º	a:95º
h:0 mm	0,06	0,004	0,06	0,01	0,01
h:15 mm	0,29	0,29	0,01	0,28	0,24
h:22.5 mm	0,30	0,28	0,29	0,26	0,28
h:30 mm	0,28	0,28	0,29	0,26	0,26
h:37.5 mm	0,29	0,28	0,29	0,28	0,26
h:45 mm	0,29	0,29	0,10	0,02	0,10
h:52.5 mm	0,04	0,04	0,02	0,05	0,03
h:60 mm	0,04	0,02	0,03	0,03	0,02

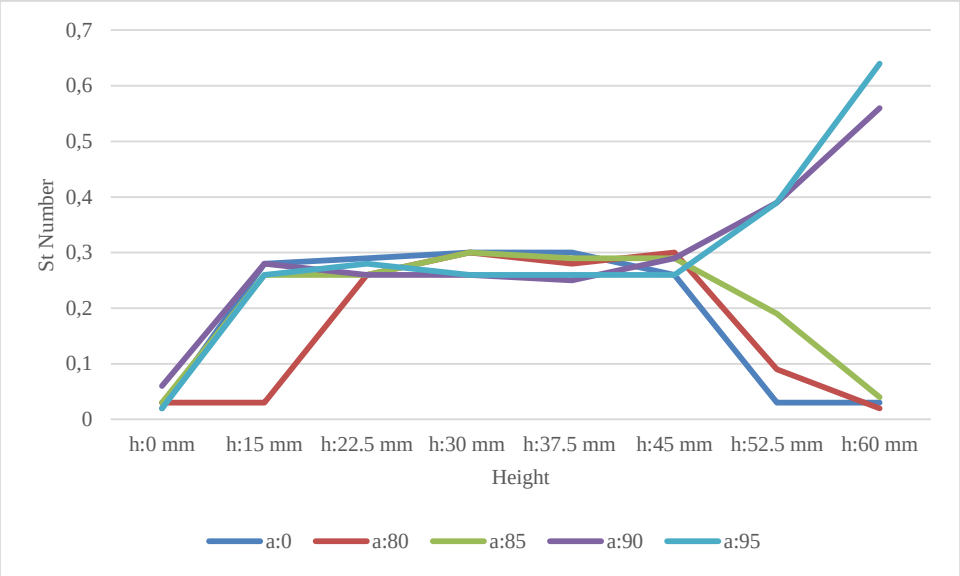

Figure. 4.56. Distribution of St number values per heights from a:0º to a: 95º for rectangular grooved cylinder.

Table 4.12. St values per height for rectangular grooved cylinder

St (w/d:2)	a:0º	a:80º	a:85º	a:90º	a:95º
h:0 mm	0,02	0,03	0,03	0,06	0,02
h:15 mm	0,28	0,03	0,26	0,28	0,26
h:22.5 mm	0,29	0,26	0,26	0,26	0,28
h:30 mm	0,30	0,30	0,30	0,26	0,26
h:37.5 mm	0,30	0,28	0,29	0,25	0,26
h:45 mm	0,26	0,30	0,29	0,29	0,26
h:52.5 mm	0,03	0,09	0,19	0,39	0,39
h:60 mm	0,03	0,02	0,04	0,56	0,64

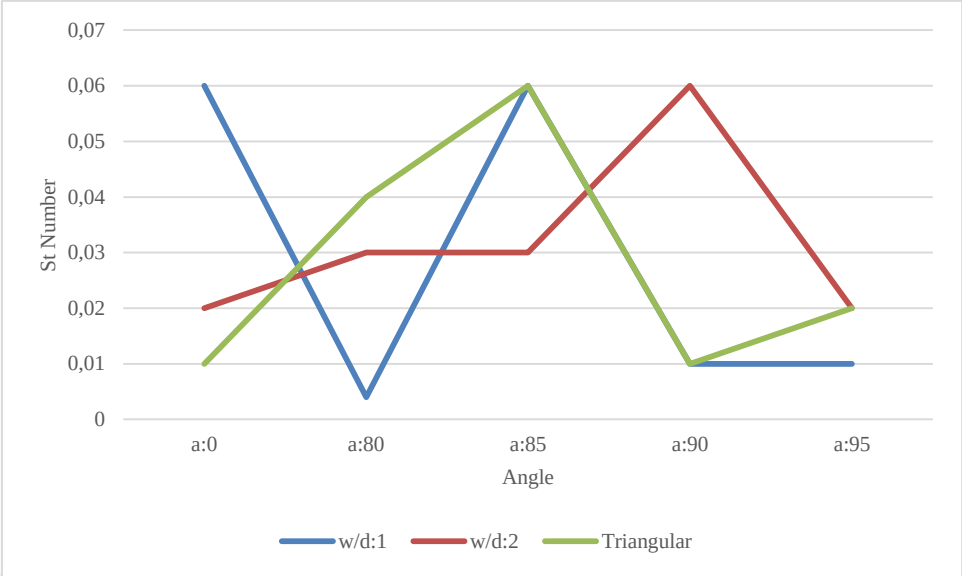

Figure. 4.57. Comparison of St number values per grooved angles for h:0 mm

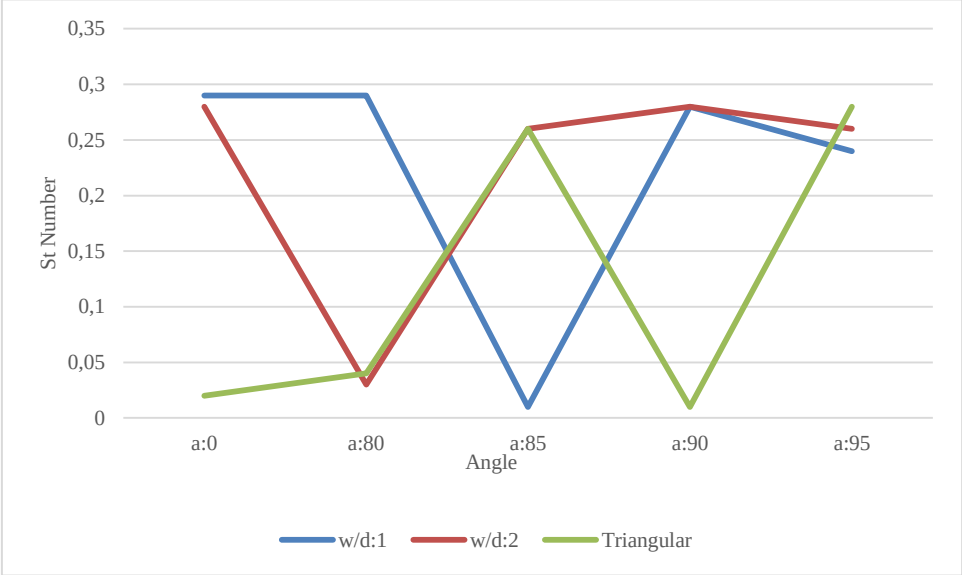

Figure. 4.58. Comparison of St number values per grooved angles for h:15 mm

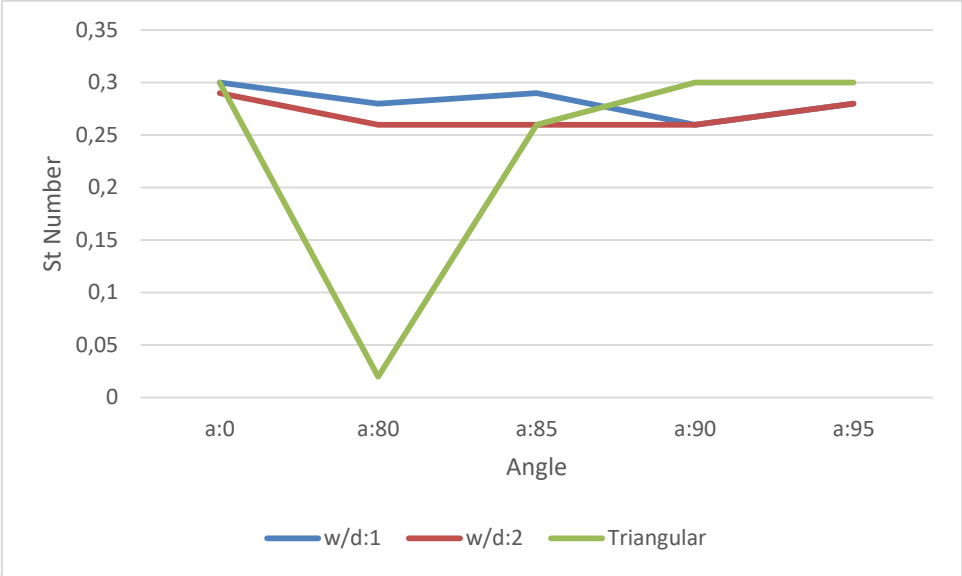

Figure. 4.59**.** Comparison of St number values per grooved angles for h:22.5 mm

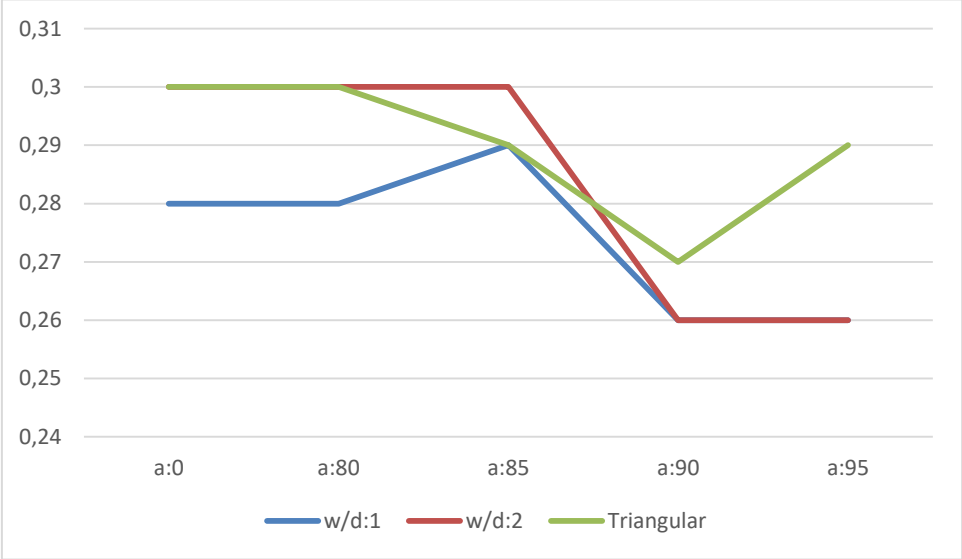

Figure. 4.60**.** Comparison of St number values per grooved angles for h:30 mm

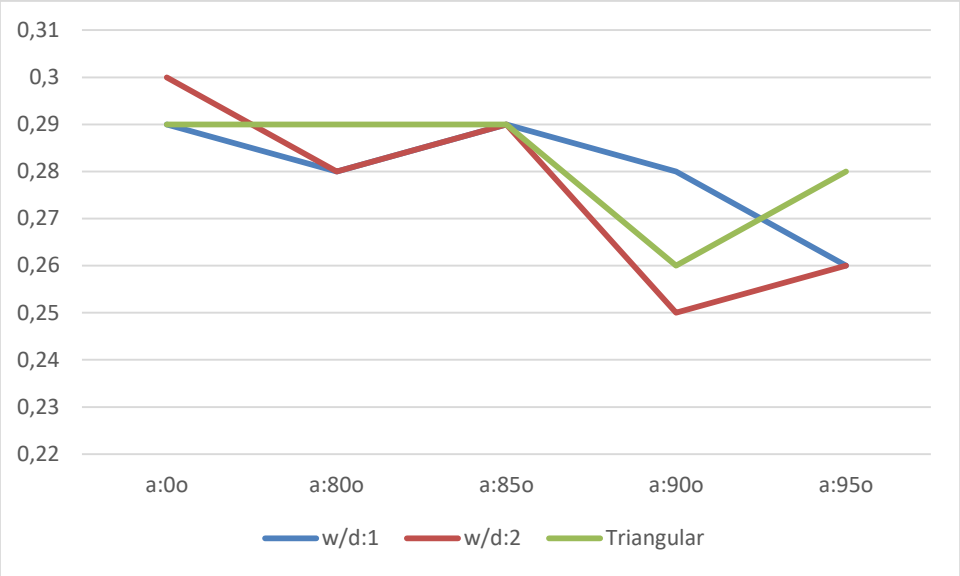

Figure. 4.61. Comparison of St number values per grooved angles for h:37.5 mm

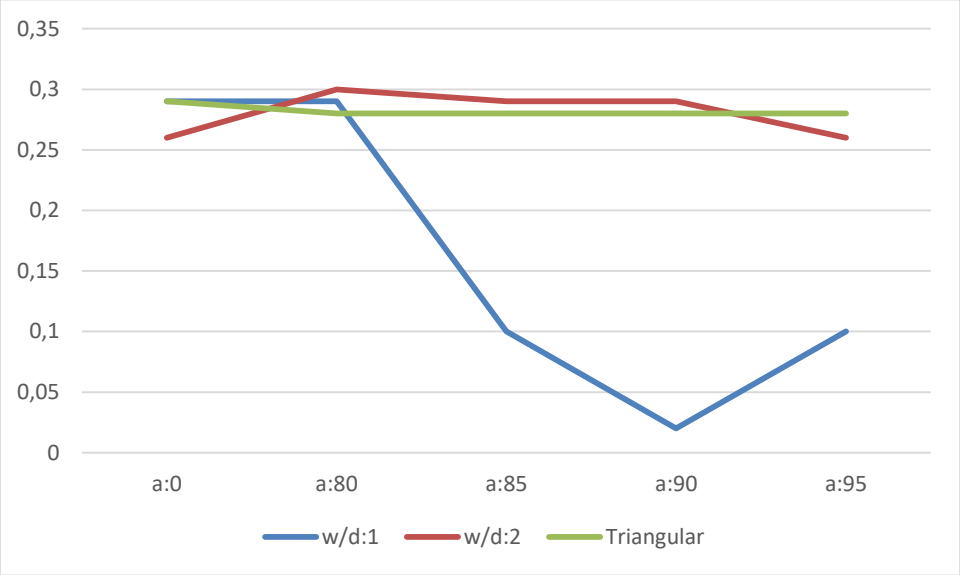

Figure. 4.62. Comparison of St number values per grooved angles for h:45 mm

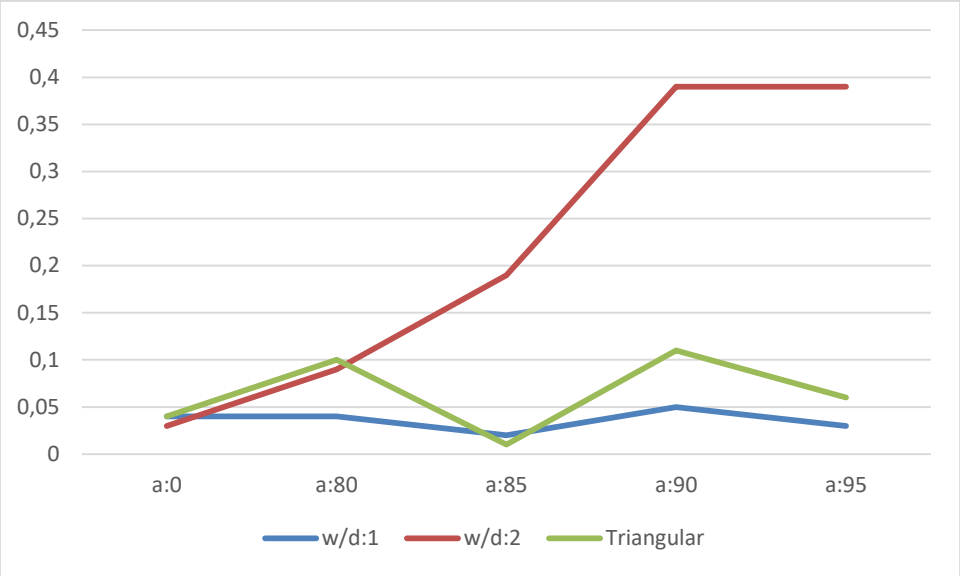

Figure. 4.63**.** Comparison of St number values per grooved angles for h:52.5 mm

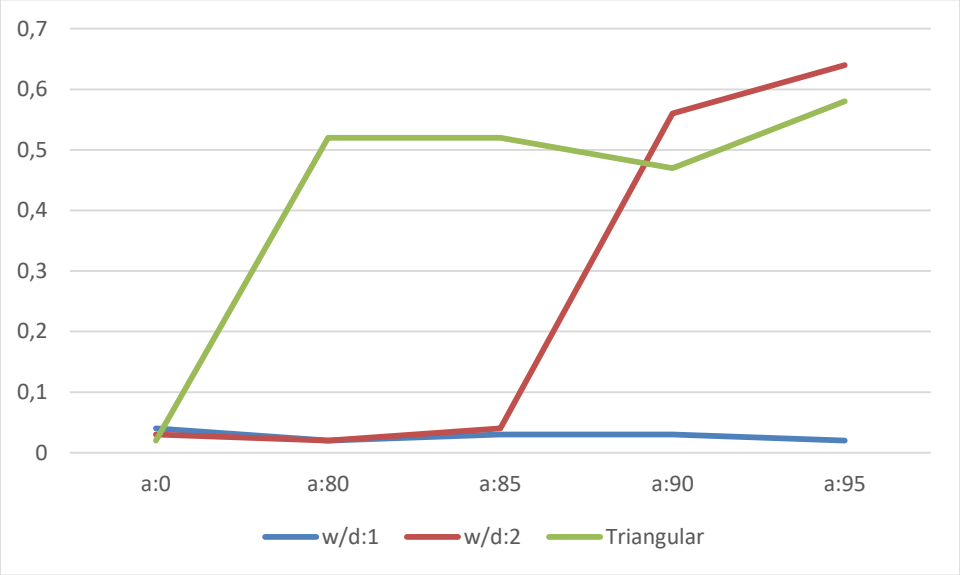

Figure. 4.64**.** Comparison of St number values per grooved angles for h:60 mm

5. CONCLUSIONS

In order to compare the fluid characteristic around bare cylinder, a triangular grooved cylinder, a square grooved cylinder and a rectangular grooved cylinders, a lot of experiments have been performed using PIV in this thesis. The experiments have been conducted under shallow water conditions, h_w=90 mm. On the other hand, the cylinders have been positioned at h: 0 mm, 15mm, 22.5 mm, 30mm, 37.5mm 45mm, 52.5 and 60 mm from bottom to surface to examine the surface effect. Another parameter is the grooved angles which change with the a: 0^o, 80^o, 85^o, 90^o and 95^o in shallow water. During the experiments, Reynolds number and Fr number have been selected as 5000 and 0.27, respectively.

According to the outcomes of the experiment, when Reynolds stress is compared between the bare cylinder and triangular grooved cylinders, the highest negative counter is formed at h: 37.5mm. In bare cylinder at h: 0 mm, the only positive counter is observed due to surface effect. Furthermore, at h: 60 mm from a: 0^o to a: 95^o, the only negative counter is accrued. Also, it seemed to streamline topology, saddle and foci point have not been seen at h: 0mm for bare cylinder and at h: 0mm a: 0^o, h: 60mm a: 80^o and a: 90^o for triangular grooved cylinder. Wake region compared to height, the biggest wake region area is observed at h: 52.5 mm for triangular, square rectabgular grooved cylinders and bare cylinders. It is clearly shown that the surface effect affects the flow structure of the dye experiment. The vortex ruptured also varies with the groove angles. The lowest CD value is at h: 22.5 mm for the bare cylinder, whereas the maximum CD at triangular groved cylinder at h: 0 mm a: 90^o is 1.42.

The results uncover that large negative counter at height h: 37.5 is observed for bare cylinder, at h: 45 mm for square grooved cylinder and rectangular grooved cylinders. Also, no negative counter is observed at h: 0 mm due to the bottom effect. Due to surface effects, a foci point at most nor foci point has been formed in cylinders close to the surface and close to the base. Two foci points and saddle point have been seen as they move away from the surface. When the wake regions consisting of two foci points are examined, the smallest vortex region is in h: 37.5 mm for rectangular grooved cylinder at a: 90^o and 95^o. Also, the highest force coefficient value at h: 52.5 mm and a:80^o is obtained for square grooved cylinder. The highest force coefficient value at h: 37.5 mm and a:95^o is obtained for rectangular grooved cylinder.

The highest St value is seen for a: 95^{o} triangular grooved cylinder and rectangular grooved cylinder. When all cylinders are compared, the minimum value of the St is observed as 0.004 at h:0 a :80^{o} for square grooved cylinder.

6. RECOMMENDATIONS

It is very little distance between the bottom of the fluid and the upper of the fluid in the shallow water. This makes the fluid more complicated than deep waters. However, there are not enough studies in shallow water in the literature. Therefore, it is aimed to control formed non-permanent flow on the back of a cylinder positioned different height, geometries and angles at the shallow water in this study, passively. As a result, this study will fill the shallow water research gap in the literature. In future studies, CFD analysis can be made with this parameter for interms of validations. In additons, this experiment can be repeated with different parameters.

REFERENCES

Akilli H. and Rockwell D. (2002). Vortex formation from a cylinder in shallow water. Physics of Fluids 14, 2957.

Akilli H., Karakus C., Akar A., Sahin B., Tumen N.F. (2008). Control of Vortex Shedding of Circular Cylinder in Shallow Water Flow Using an Attached Splitter Plate Journal of Fluids Engineering.130,041401-3.

Akilli H., Şahin B., Tümen N.F. (2005). Suppression of vortex shedding of circular cylinder in shallow water by a splitter plate. Flow Measurement and Instrumentation 16, 211-219.

Akoz M. S, 2012. Investigation of vortical flow characteristics around a partially buried circular cylinder. Ocean Eng. 52,35-51.

Alonzo-Garcia A., Gutierrez-Torres C.C., Jimenez B.J.A., Mollinedo-Ponce L.H.R., Martinez-Delgadillo S.A., Barbosa-Saldana J.G. "RANS simulations of the U and V grooves effect in the subcritical flow over four rotated circular cylinders", Journal of Hydrodynamics, 4, 569-578.

Bayraktar S, Yayla S, Oztekin A, Ma H, 2014. Wall proximity effects on flow over cylinders with different cross sections. Can. J. Phys. 10, 1141-1148.

Canpolat C, Sahin B., 2017. Influence of single rectangular groove on the flow past a circular cylinder. *Int. J Heat Fluid Fl*. 64, 79–88.

Canpolat C., 2015. Characteristics of flow past a circular cylinder with a rectangular groove. *Flow Meas. Instrum*. 45, 233–246.

Chen D., Jirka G.H. 1995. "Experimental study of plane turbulent wakes in a shallow water layer", Fluid Dynamics Research,1, 11-41.

Choi H., Jeon W-P. and Jinsung Kim J., (2008). Control of flow over a bluff body. Annu. Rev. Fluid Mech. 40, 113–39.

Chutkey K,Suriyanarayanan P, Venkatakrishnan L, 2018. Near wake field of circular cylinder with a forward splitter plate. Journal of Wind Engineering and Industrial Aerodynamics. 173, 28-38.

Dai S, Younis B. A, Zhang H, Guo C, 2018.Journal of Wind Engineering and Industrial Aerodynamics Prediction of vortex shedding suppression from circular cylinders at high Reynolds number using base splitter plates 182,115-127.

Durhasan (2020). T. Flow topology downstream of the hollow square cylinder with slots. Ocean Engineering 209, 107516.

Durhasan T, Pinar, Ozkan G.M, Aksoy M.M, Akilli H and Sahin B., 2018. PIV Measurement downstream of perforated cylinder in deep water. *Eur. J Mech B-Fluid*. 72, 225-234.

Durhasan T., Aksoy M.M., Pinar E., Ozkan G.M., Akilli H., Sahin B. (2016). Vortex street suppression of a circular cylinder using perforated semi-circular fairing in shallow water. Experimental Thermal and Fluid Science 79, 101-110.

El-Makdah, A.M., Oweis, G.F. 2013. "The flow past a cactus-inspired grooved cylinder", Exp Fluids, 54,1464.

Fırat E, Akansu Y.E, Akilli H., 2015. Flow past a Square Prism with an Upstream Control Rod at Incidence to Uniform Stream. *Ocean. Eng.* 108, 504–518.

Firat E., Gokturk M. Ozkan G.M., Akilli H. (2017). PIV measurements in the near wakes of hollow cylinders with holes. Exp Fluids 39,1 -19.

Firat E., M. Ozkan G.M., Akilli H. (2019). Flow past a hollow cylinder with two spanwise rows of holes. Experiments in Fluids 60, 163.

Gao Y., Yang K., Ren X., Zhang B., Tan S. K., 2018. Flow behavior behind a clockwise-and-counterclockwise rotational oscillating cylinder. *Ocean. Eng.* 159, 410–421.

Göktürk M.Ö., Fırat E., Akıllı H (2017). Passive flow control in the near wake of a circular cylinder using attached permeable and inclined short plates. Ocean Engineering 139, 35-49.

Gozmen B, Akilli H, Sahin B., 2013. Passive control of circular cylinder wake in shallow flow. *Measurement*. 46, 1125–1136.

He G. S, Wang J. J, Pan C, Feng L. H, Gao Q, Rinoshika A, 2017. Vortex dynamics for flow over a circular cylinder in proximity to a wall. J. Fluid Mech. 812, 698-720.

Kahraman A, Ozgoren M. and Sahin B., 2012. Flow structure from a horizontal cylinder coincident with free surface in shallow water flow. *Therm. Sci.* 16, 93-107.

Karasu I., 2020. Flow control over a diamond-shaped cylinder using slits. *Experimental Therm. Fluid Sci*. 112, 109992.

Lei, C., Cheng, L., Kavanagh, K. 1999. "Re-examination of the effect of a plane boundary on force and vortex shedding of a circular cylinder", Journal of Wind Engineering and Industrial Aerodynamics, 8, 263-86.

Leung, Y.C., Wong, C.H., Ko, N.W.M. 1997. “Characteristics of flows over an asymmetrically grooved circular cylinder in transitional regimes”, Journal of Wind Engineering and Industrial Aerodynamics, 71,169-178.

Lim, H.C., Lee, S.J. 2003. “PIV measurements of near wake behind a U-grooved cylinder”, Journal of Fluids and Structures, 18:119-130.

Liu Y.Z, Shi L.L, Yu J., 2011. TR-PIV measurement of the wake behind a grooved cylinder at low reynolds number. *J. Fluids Struct.* 27, 394-407.

Liu, Y.Z., Shi L.L., Yu, J. 2011. “TR-PIV measurement of the wake behind a grooved cylinder at low Reynolds number”, Journal of Fluids and Structures, 27,394-407.

Najafi L, Firat F, Akilli H., 2016. Time-averaged near-wake of a yawed cylinder. *Ocean. Eng*. 113, 335–349.

Narayanan K.V, Vengadesan S, Murali K., 2018. Wall proximity effects on the flow past cylinder with flexible filament. Ocean Eng. 157, 54-61.

Oner A. A, Kirkgoz M. S, Akoz M. S, 2008. Interaction of a current with a circular cylinder near a rigid bed. Ocean Eng. 35, 1492-1504.

Oruç V, Akilli H, Sahin B., 2016. PIV measurements on the passive control of flow past a circular cylinder. *Exp. Therm. Fluid Sci*. 70, 283–291.

Oruc V., 2012. Passive control of flow structures around a circular cylinder by using screen. *J. Fluids Struct*. 33, 229–242.

Ozdil N. F, Akilli H., 2015. Investigation of flow structure around a horizontal cylinder at different elevations in shallow water. *Ocean. Eng*. 96, 56-67.

Ozdil N. F, Akilli H., 2019. Flow comparison around horizontal single and tandem cylinders at different immersion elevations. *Ocean. Eng*. 188, 106352.

Ozgoren M., Pınar E., Sahin B., Akilli H., (2011). Comparison of flow structures in the downstream region of a cylinder and sphere, Int. J Heat Fluid Fl. 32, 1138-1146.

Ozkan M.G. Fırt E., Akıllı H. (2017) Control of vortex sheddıng usıng a screen attached on the separatıon poınt of a cırcular cylınder and ıts effect on drag. Journal of Fluids Engineering.

Ozkan M.G., Oruç V., Akıllı H. (2012). Flow around a cylinder surrounded by a permeable cylinder in shallow water. Exp Fluids 53,1751–1763.

Pinar E, Ozkan G.M, Durhasan T, Aksoy M.M, Akilli H, Sahin B., 2015. Flow structure around perforated cylinders in shallow water. *J. Fluids Struct*. 55, 52-63.

Quintavalla, S.J., Angilella, A.J., Smits, A.J. 2013. “Drag reduction on grooved cylinders in the critical Reynolds number regime”, Experimental Thermal and Fluid Science, 48, 15-18.

Rinoshika H, Rinoshika A., 2019. Passive control of a front inclined hole on flow structures around a surface-mounted short cylinder. *Ocean. Eng*. 189, 106383.

Sanlı B.G., Akıllı H. (2018). Effects of Permeable Cylinder on the Flow Structure in Deep Water. Fluıd dynamıcs 53,134- 145.

Sheridan J., Lin J.C., Rockwell D. 1997. “Flow past a cylinder close to a free surface”, Journal of Fluid Mechanics, 330, 1-30.

Shi L, Wang Y, Zhang G, Jin Y, Zhang D, 2020. Applied Mathematical Modelling. Assessment of an improved turbulence model in simulating the unsteady flows around a D-shaped cylinder and an open cavity.83, 552-575.

Shi L. L, Liu Y. Z, Wan J. J, 2010. Influence of wall proximity on characteristics of wake behind a square cylinder: PIV measurements and POD analysis. Exp. Therm. and Fluid Sci. 34, 28-36.

Son O. and Cetiner O., (2015). Drag prediction in the near wake of a circular cylinder based on dpiv data. J. Appl. Fluid Mech. 9, 1963-1968.

Song X., Qi Y., Zhang M., Zhang G., Zhan W. (2019). Application and optimization of drag reduction characteristics on the flow around a partial grooved cylinder by using the response surface method. Engineering Applications of Computational Fluid Mechanics.13, 158–176.

Sooraj P, Khan M. H, Sharma A, Agrawal A., 2019. Wake analysis and regimes for flow around three side-by-side cylinders. *Exp. Therm. Fluid Sci*. 104, 76-88.

Wang X.C, Zhang J. X, Hao Z, Zhaou B, Tan S.K, 2015. Influence of wall proximity on flow around two tandem circular cylinders. Ocean Eng. 94, 36-50.

Wang, S.F., Liu, Y.Z., Zhang, Q.S. 2014. “Measurement of flow around a cactus-analogue grooved cylinder at ReD =5,4.104: Wall-pressure fluctuations and flow pattern”, Journal of Fluids and Structures, 50,120-136.

Wen C.Y, Yeh C. L, Wang M. J, Lin C.Y., (2004). On the drag of two-dimensional flow about a circular cylinder. Phys. Fluids, 10, 3828 - 3831.

Yagmur S, Dogan S, Aksoy M.H, Goktepeli I, Ozgoren M., 2017. Comparison of flow characteristics around an equilateral triangular cylinder via PIV and Large Eddy Simulation methods. *Flow Meas. Instrum*. 55, 23–36.

Yamagishi, Y., Oki, M. 2004. “Effect of groove ghape on flow characteristics around a circular cylinder with grooves”, Journal of Visualization, 3,209-216.

Yang F, An H, Cheng L, 2018. Drag crisis of a circular cylinder near a plane boundary. Ocean Eng. 15, 133-142.

Yang F, Zhou Z, Lou X, Lu L, 2020.Ocean Engineering. Flow around a near-bed horizontal circular cylinder mounted on a vertical wall.216,107586.

Yang H, Yang W, Yang T, Lia Q, 2020.Ocean Engineering. Experimental investigation of flow around a square cylinder with very small aspect ratios.214 107732.

Yayla S, Teksin S., 2018. Flow measurement around a cylindrical body by attaching flexible plate: a PIV approach. *Flow Meas. Instrum*. 62, 56-65.

Zdravkovich, M.M. 1980. “Intermittent flow separation from flat plate induced by a nearby circular cylinder”, In: Proceeding of the 2nd international symposium on flow visualization, 21, 265-70.

Zhang, H.L., Ko, N.W.M. 1995. “Numerical analysis of incompressible flow over smooth and grooved circular cylinders”, Computers & Fluids, 3, 263-281.

Zhou B, Wang X, Guo W, Gho W. M, Tan S.K., 2015. Experimental study on flow past a circular cylinder with rough surface. *Ocean. Eng.* 109, 7–13.

Zhou, B., Wang, X., Guo W., Zheng J., Tan S.K. 2015. “Experimental measurements of the drag force and the near-wake flow patterns of a longitudinally grooved cylinder”, Journal of Wind Engineering and Industrial Aerodynamics”, 145,30-41.